Dissertation

Brillouin Light Scattering Study of Linear and Nonlinear Spin Waves in
Continuous and Patterned Magnetic Thin Films

Submitted by

Hau-Jian Jason Liu

Department of Physics

In partial fulfillment of the requirements

For the Degree of Doctor of Philosophy

Colorado State University

Fort Collins, Colorado

Summer 2014

Doctoral Committee:

Advisor: Kristen S. Buchanan

Martin P. Gelfand
Pavel Kabos
James R. Neilson

Abstract

BRILLOUIN LIGHT SCATTERING STUDY OF LINEAR AND NONLINEAR SPIN WAVES IN
CONTINUOUS AND PATTERNED MAGNETIC THIN FILMS

This thesis focuses on the use of the Brillouin light scattering (BLS) technique to measure spin waves or magnons in thin films. BLS is an experimental technique that measures the inelastically scattered light from photon-magnon interactions. Broadly, three different experiments are presented in this thesis: the measurements of spin wave properties in iron cobalt (FeCo), yttrium iron garnet (YIG), and microstructures involving Permalloy ($Ni_{80}Fe_{20}$) and cobalt nickel (CoNi). First, conventional backward scattering BLS was used to measure the spin waves in a set of $Fe_{65}Co_{35}$ films that were provided by Seagate Technologies. By fitting the spin wave frequencies that were measured as a function of the external magnetic field and film thickness, the quantum mechanical parameter responsible for short range order, known as the exchange parameter, was determined. Second, nonlinear spin waves were measured in YIG using conventional forward scattering BLS with time resolution. Two nonlinear three wave processes were observed, namely, the three magnon splitting and confluence. The nonlinear power threshold, the saturation magnetization, and the film thickness were determined independently using network analyzer measurements. The spin wave group velocities were determined from the space- and time-resolved BLS data and compared to calculations from the dispersion relations. Back calculations showed the location where the three magnon splitting process took place. Lastly, spin waves in Permalloy and CoNi microstrips were measured using a recently developed micro-BLS. The micro-BLS, with a spatial resolution of 250 nm, allows for measuring the effects on the lateral confinement of spin waves in microstrips. The confinement of spin waves led to modifications to the dispersion relations, which were

compared against the spin wave frequencies obtained from the micro-BLS. The Permalloy experiments shows non-reciprocity in surface spin wave modes with opposite wavevectors and provides a quantitative measure of the difference in excitation efficiency between the surface spin wave and the backward volume spin wave modes. Measurements were also conducted in the Permalloy microstrips at zero external magnetic field, showing evidence that propagating spin waves can be observed by exploiting the effects of shape anisotropy. Finally, preliminary measurements were done on CoNi microstrips with perpendicular anisotropy. A magnetic signal was detected, however further investigation will be needed to determine the exact origin of the observed signal and to definitively answer the question as to whether or not BLS can be used to measure spin waves in perpendicularly magnetized films. Overall, the experiments and results presented in this thesis show that BLS is a useful tool for measuring spin wave properties in magnetic thin films.

TABLE OF CONTENTS

H External magnetic field. . . . . .Oe

H_i Internal magnetic field. . . . . .Oe

H_{demag} Demagnetization field. . . . . Oe

N Demagnetization factor. . . . . *unitless*

M Volume magnetization. . . . . emu/cm^3

M_s Saturation magnetization. . . . . emu/cm^3

$4\pi M_s$ Saturation magnetiztion. . . . . G

m Magnetic moment. . . . . .emu

g Landé g-factor. . . . . *unitless*

$\gamma/2\pi$ Gyromagnetic ratio. . . . . Hz/Oe

α Exchange parameter. . . . . cm^2

λ Wavelength. . . . . .nm

f_p Pumping frequency. . . . . GHz

f_c Confluence frequency. . . . . GHz

k_{cutoff} Cutoff wavevector. . . . . μm^{-1}

κ_n Perpendicular standing spin wave wavevector. . . . .μm^{-1}

k_n Total spin wave wavevector. . . . .μm^{-1}

$k_\parallel$ Wavevector parallel to the film surface. . . . .μm^{-1}

k_p Quantized lateral spin wave wavevector. . . . .μm^{-1}

q_I Incident photon wavevector. . . . .μm^{-1}

q_s Scattered photon wavevector. . . . .μm^{-1}

v_g Group velocity. . . . .μm/s

LIST OF ACRONYMS

BLS .... Brillouin light scattering

BV .... Backward volume

DE .... Damon-Eshbach

FMR .... Ferromagnetic resonance

FP1 .... First Fabry-Perot interferometer

FP2 .... Second Fabry-Perot interferometer

FSR .... Free spectral range

MOKE .... Magneto-optic Kerr effect

MSBVW .... Magnetostatic backward volume wave

MSFVW .... Magnetostatic forward volume wave

MSSW .... Magnetostatic surface wave

PNA .... General purpose network analyzer

PSSW .... Perpendicular standing spin wave

ROI .... Region of interest

TFP .... Tandem Fabry-Perot interferometer

CHAPTER 1

INTRODUCTION

1.1. MOTIVATION

Ferromagnetic materials are used in our everyday lives. The most common uses for them are in permanent magnets, which can be found in compasses, refrigerator magnets, speakers, and motors of generators. Currently, ferromagnetic materials are also widely used in recording devices. These devices store information based on the magnetization state of a system. The need to optimize magnetic recording storage density has driven research in the field of magnetic switching, magnetic anisotropy, and magnetic damping. Recently, polarized spin currents have been used in spintronic devices: devices that uses the spin degree of freedom of electrons as opposed to their electric charge. Advances in these fields require an understanding of the material parameters used in magnetic recording and spintronic devices.

Spin waves are magnetic excitations are quantized as magnons. These excitations follow dispersion relations that describe their energy (frequency) and momentum (wavevector). The dispersion relations are governed by material parameters like exchange, anisotropy, and saturation magnetization. Spin waves show unique properties depending on their direction of propagation with respect to an external magnetic field. By measuring the spin wave frequency and wavevector one can extract useful material parameters.

Brillouin light scattering (BLS) is a technique that measures the frequency shift of inelastically scattered light. In the last few decades, BLS has grown in popularity because of the information that can be obtained using this technique with magnetic materials. The technique is non-invasive and allows for control of useful parameters like the external magnetic field, the spin wave wavevector, and in microwave-excited systems the spin wave frequency

can be controlled. The frequency shift of the inelastically scattered light directly corresponds to the spin wave frequency, thus it provides a direct means to probe dispersion relations. With the recent development of the micro-BLS, localized spin wave measurements with sub-micrometer resolution can now be achieved.

1.2. OBJECTIVES

The focus of this thesis is to use the BLS technique to measure spin waves in a variety of magnetic thin films and patterned microstructures. The spin wave measurements were used in several ways: to determine magnetic parameters, to gain insight into nonlinear spin wave dynamics, and to explore spin wave confinement in microstructures. In all cases, the spin wave dispersion relations have been used to guide the experiments and understand the results. Several different configurations of the BLS were used: conventional backward scattering, conventional forward scattering, space-resolved, time-resolved, and micro-BLS, which will be described in detail in the chapters to come.

1.3. THESIS STRUCTURE AND ORGANIZATION

This thesis consists of three separate sets of experiments that are linked by a common theme: spin wave processes in magnetic thin films measured with BLS. The individual experiments are presented in Chap. 4, 5, and 6. Specific properties and physics of spin waves that are relevant to the individual experiments are presented in the corresponding chapters.

Chapter 2 gives a general overview of spin wave dynamics in thin films. The different types of energies that play a role in magnetic systems are discussed. These energies are the Zeeman energy, dipole-dipole energy, exchange energy, and anisotropy energy. The results from the torque equation are presented for uniform precession, ferromagnetic resonance,

and then as the more general theory for propagating spin waves in the form of dispersion relations. The dispersion relations are the general theory that is used throughout this thesis to fit and to understand experimental results. This chapter focuses on dispersion relations for magnetic thin films: modifications to the dispersion relations that are required for patterned microstrips as discussed in Chap. 6.

The light scattering mechanisms and the experimental BLS apparatus are discussed in Chap. 3. Raman and Brillouin scattering are first considered followed by the mechanisms of how light couples to magnetic excitations. The main components of the BLS are reviewed; particularly, the tandem Fabry-Perot interferometer. This chapter also includes a brief description of the recently developed micro-BLS, which is used to measure spin waves with a spatial resolution of 250 nm. It will be shown in Chap. 6 that the micro-BLS is particularly useful for measuring spin waves that are laterally confined in microstrips.

Chapter 4 discusses external magnetic field- and film thickness-dependent BLS measurements conducted on a set of $Fe_{65}Co_{35}$ films. A general procedure for fitting the frequencies from surface spin waves and perpendicular standing spin waves is shown to obtain the quantum mechanical exchange parameter α that is responsible for short range magnetic order. This procedure was applied to the spin wave frequencies obtained by BLS and the exchange parameter was determined.

Chapter 5 discusses nonlinear spin wave processes in yttrium iron garnet. The processes that were investigated were the three magnon splitting and confluence. A detailed set of microwave measurements were performed using a network analyzer to determine the nonlinear microwave power threshold and material parameters like the saturation magnetization and the film thickness. One-dimensional spatial and time-resolved BLS scans allowed for the

measurement of spin wave group velocities for both the magnons generated by splitting and by confluence.

Chapter 6 discusses the spin wave measurements in Permalloy and CoNi microstrips. The Permalloy measurements address the question of nonreciprocal behavior of surface spin waves with opposite wavevectors. It is experimentally shown that surface waves with opposite wavevectors have a 3:1 ratio in intensity. Also shown in this chapter is evidence that backward volume spin waves can exist in the absence of an external magnetic field. A discussion on how this is achieved with the use of shape anisotropy is also presented. Preliminary BLS measurements are presented on CoNi microstrips, a material with strong perpendicular anisotropy, with out-of-plane and in-plane external magnetic fields.

Chapter 7 summarizes the work and results presented in this thesis. A section is include which specifically suggests improvements to the micro-BLS technique to maximize the spin wave information obtained from BLS. Possible future directions for the preliminary work on CoNi presented in Chap. 6 are also discussed.

Appendix A reviews the design of an optical mask and photolithography process that has proven successful for conducting spin wave measurements using the micro-BLS technique. First, the design of an optical mask with the waveguide structures that are compatible with the micro-BLS is discussed. Lastly, a procedure for photolithography and liftoff is included.

CHAPTER 2

Magnetization Dynamics

2.1. Introduction

Magnetic materials that possess a permanent magnetization show interesting properties when placed in an externally applied magnetic field. Figure 2.1 shows a flow chart that illustrate the different classifications of magnetic properties: diamagnetism, paramagnetism, ferromagnetism, ferrimagnetism, and antiferromagnetism. This thesis will focus on the properties of ferromagnetic materials. The magnetization in ferromagnetic materials arises from electrons filling orbitals following Hund's rules [1]. Electrons of spin "up" are filled first, then electrons with spin "down" are paired with them. The origin of magnetism results from the net dipole moment formed by the unpaired electrons. 3d metals, the type of metals studied in this thesis, possess a large magnetization because they have a large number of unpaired electrons. Ferromagnetic materials have spins that are all aligned parallel and the dipole moments are all equal in magnitude. Antiferromagnetic materials on the other hand, have spins that are anti-parallel to their nearest neighbor, which results in a net zero magnetization. Exchange interactions between electrons will govern whether the energy is lower for aligned or anti-aligned spins and whether the material will be ferromagnetic or antiferromagnetic. Note that ferrimagnetic materials, like yttrium iron garnet (YIG), are treated like ferromagnetic materials because they possess spins that are aligned parallel but the dipole moments differ in magnitude with their nearest neighbors, which still gives rise to a net magnetization.

The individual moments $\mathbf{m}$ of ferromagnetic materials collectively form a volume magnetization $\mathbf{M} = \mathbf{m}/V$, where V is the volume that the moments are contained in. When
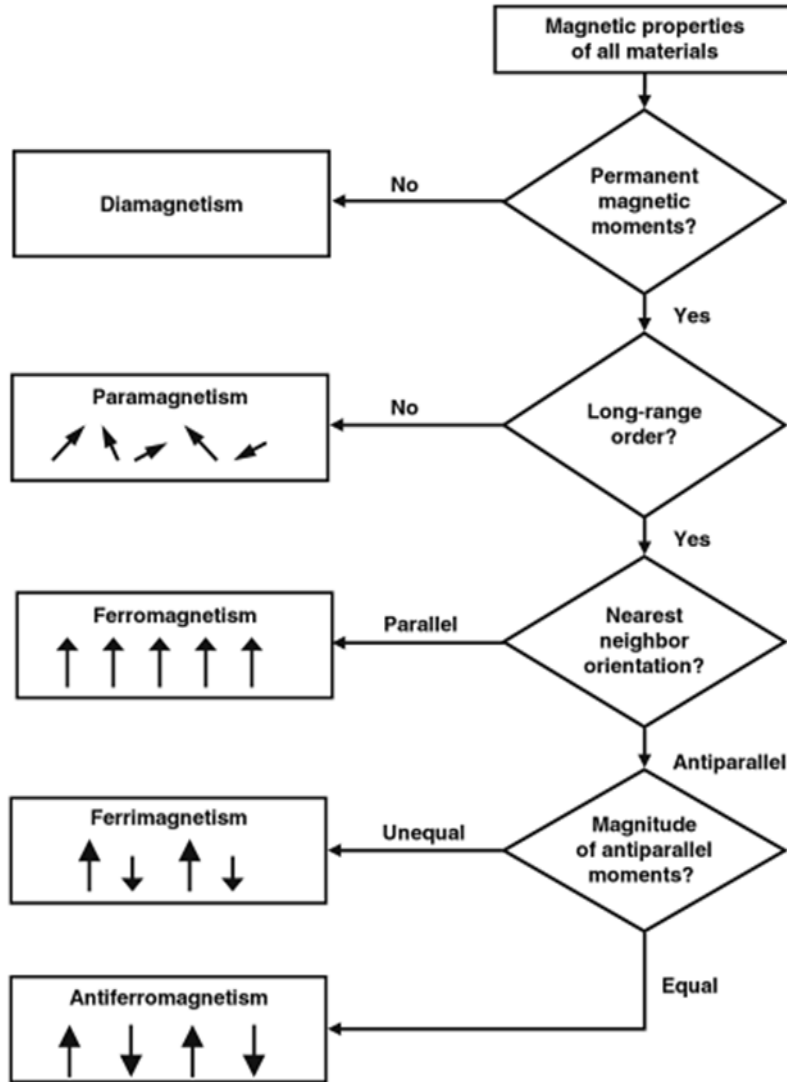
FIGURE 2.1. Flow chart of different classifications of magnetic properties. This figure was reproduced from Ref. [2] with permission from Springer.

placed in an externally applied magnetic field $\mathbf{H}$, this magnetization will precess about $\mathbf{H}$. For an isolated electron the processional frequency is called the Larmor precession frequency and is in the microwave frequency regime. In a ferromagnetic system where the electron are coupled, the uniform precessional motion of $\mathbf{M}$ is called ferromagnetic resonance (FMR). FMR has proven useful for determining magnetic properties such as the saturation magnetization [3–5], anisotropy [6–9], and magnetic damping [10–13]. The saturation magnetization is the maximum magnetization per unit volume for a material, typically observed when the

magnetization is fully aligned in a large external magnetic field. The energy that describes the fact that the energy of a sample often depends on the direction of the spins with respect to the crystal lattice or, in patterned structures, with respect to the geometrical axes, is call anisotropy energy. Magnetic damping is an intrinsic parameter that describes the rate of energy loss for a precessing magnetization and is related to the time it will take for the magnetization to return to equilibrium after a perturbation.

FMR describes the uniform precession of $\mathbf{M}$, where the individual moments are all precessing at the same frequency and in phase. Spin waves occur when each individual dipole is precessing slightly out of phase with its nearest neighbor. This produces a propagating wave that has energy and momentum associated with it. The energy and momentum are related to one another by the spin wave dispersion relations. Because nearest neighbor interactions are dominated by what is called the exchange parameter α, an understanding of the spin wave dispersion relations can be used to determine this parameter.

This chapter starts off by reviewing the energies that play a role in the dynamics of a ferromagnetic system. The equation of motion is presented as the basis of FMR and the results for an infinite sheet approximation is presented. Finally, the spin wave dispersion relations for out-of-plane and in-plane magnetized films are present with both pinned and unpinned boundary conditions.

2.2. Magnetostatic Energies

The dynamic magnetization of a system can be described by considering the different energies that contribute to its motion. The energies that are typically the most important for magnetization dynamics are the Zeeman energy, dipole-dipole energy, exchange energy, and anisotropy energy. This section discusses the former three. Anisotropy energy is related

to the fact that there are preferred directions of the magnetization and can sometimes be treated as an additional magnetic field, for example in magnetic microstrips as described in Chap. 6.

The Zeeman energy describes the energy associated with a magnetic moment $\mathbf{m}$ in an externally applied magnetic field $\mathbf{H}$. This energy is defined as [14]:

$$\mathcal{E}_{Zeeman} = -\mathbf{m} \cdot \mathbf{H}. \tag{2.1}$$

This and all other equations are given in CGS units. Note that the equations are slightly different in SI units. Details on the conversion between units can be found in Ref. [15]. It can be seen that the energy is at a minimum when $\mathbf{m}$ and $\mathbf{H}$ are in the same direction. This means that for a ferromagnetic system in an externally applied magnetic field, the magnetization tends to align along $\mathbf{H}$. The total Zeeman energy of a collection of dipoles is the sum of all individual energies.

Magnetic moments also produce dipolar magnetic fields that are felt by other moments, which results in long range interactions. This energy is called the dipole-dipole energy and is written as [16]

$$\mathcal{E}_{dipole-dipole} = (\mu_B g)^2 \sum_{\substack{i,j=1 \\ i \neq j}}^{N} \left[\frac{\mathbf{S}_i \cdot \mathbf{S}_j}{r_{ij}^3} - \frac{3(\mathbf{S}_i \cdot \mathbf{r}_{ij})(\mathbf{S}_j \cdot \mathbf{r}_{ij})}{r_{ij}^5} \right] \tag{2.2}$$

where μ_B is the Bohr magneton and g is the Landé g-factor which is taken as 2.0 for a free electron and is often close to or slightly higher for ferromagnetic materials. The quantum mechanical spin of the moment is taken as $\mathbf{S}$ where the subscripts represent the ith and j^{th} spin. The sum is over N spins and r_{ij} is the distance between $\mathbf{S}_i$ and $\mathbf{S}_j$. The magnetic

moment is related to the spin by $\mathbf{m} = \gamma\mathbf{S}$, where γ is the gyromagnetic ratio. For a free electron $\gamma = 1.76 \times 10^7$ rad/s·Oe and $\gamma/2\pi = 2.8$ MHz/Oe.

The exchange energy leads to short range order in ferromagnetic systems. Exchange is a quantum mechanical effect and describes the interactions between nearest-neighbor spins. For a one-dimensional chain of N spins, the exchange energy is written as

$$\mathcal{E}_{exchange} = -2J\sum_{i=1}^{N}\mathbf{S}_i \cdot \mathbf{S}_{i+1}, \tag{2.3}$$

where J is the exchange integral and $\mathbf{S}_{i+1}$ is the nearest-neighbor to $\mathbf{S}_i$. Note that for a ferromagnet, J is positive and it is negative for antiferromagnets.

2.3. Uniform Precession and Ferromagnetic Resonance

Uniform precession occurs when a collection of spins with magnetization $\mathbf{M}$ precesses about $\mathbf{H}$ all in phase. The precession is driven by the torque exerted on $\mathbf{M}$ by $\mathbf{H}$. The equation of motion for the magnetization is given as

$$\frac{d}{dt}\mathbf{M} = -\gamma[\mathbf{M} \times \mathbf{H}] + damping\ term(s). \tag{2.4}$$

Setting $\mathbf{H}$ along the z-axis results in solutions where both M_x and M_y vary in time with a time dependence of $exp(-i\omega t)$, where t is the time, $\omega = 2\pi f$ is the angular frequency, and f is the frequency. Solving Eq. 2.4 assuming $d|\mathbf{M}|/dt = 0$ yields the FMR frequency ω. In a thin film, the infinite sheet approximation, where the static magnetization is only in one direction, is sufficient to describe ω. The solutions to Eq. 2.4 were calculated by Kittel in Ref. [17] and the result is

$$\omega^2 = \left[\omega_H + (N_y - N_x)\omega_M\right]\left[\omega_H + (N_z - N_x)\omega_M\right]. \tag{2.5}$$

This is commonly referred to as Kittel's equation. The external magnetic field H and saturation magnetization $4\pi M_s$ terms are contained in $\omega_H = \gamma H$ and $\omega_M = \gamma 4\pi M_s$, respectively. N_x, N_y, and N_z are demagnetization factors. The demagnetization factors are constants that describe a field H_{demag} that opposite to H. The demagnetization factors are discussed in more detail in Chap. 6.

The FMR frequency for an out-of-plane magnetized film is

$$\omega = \omega_H - \omega_M. \tag{2.6}$$

Note that for the magnetization to point out-of-plane, ω_H must be greater than ω_M. The FMR frequency for an in-plane magnetized film is

$$\omega = [\omega_H(\omega_H + \omega_M)]^{1/2}. \tag{2.7}$$

The difference between these two arises from the demagnetization factors discussed in Chap 6.

2.4. SPIN WAVES

Dispersion relations are key to understanding which spin waves, also referred to as magnons, will be excited in a given geometry and how they will behave. Dispersion relations relate the spin wave energy or frequency to the momentum or wavevector. This section will focus on spin waves in thin films because these are the samples that are discussed in Chap. 4, 5, and 6. Figure 2.2 illustrates a spin wave using a one-dimensional chain of spins. The spins precess at the same frequency but they precess such that the precession of each successive nearest neighbor is slightly different in phase. The spin wave shown in Fig. 2.2 has a wavelength $\lambda = 2\pi/k$, where k is the magnitude of its wavevector.
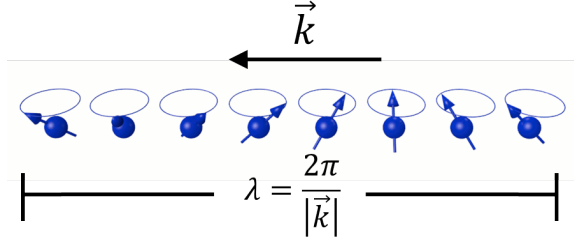
FIGURE 2.2. Illustration of a one-dimensional chain of spins that form a spin wave, where k is the spin wave wavevector and λ is the spin wave wavelength.

2.4.1. SPIN WAVE MODES. There are two directions for the static magnetization that are considered: a film that is magnetized out-of-plane and in-plane. All other directions are linear combinations of the two. Table 2.1 summarizes the main geometries for spin wave propagation in thin films. Spin waves that propagate parallel to the film surface of an out-of-plane magnetized film are called magnetostatic forward volume waves (MSFVW) and spin waves that propagate parallel to the surface of an in-plane magnetized film are called either magnetostatic surface waves (MSSW) or magnetostatic backward volume waves (MSBVW). The magnitude of the wavevector of spin waves that propagate parallel to the film surface is denoted as $k_\parallel$. MSSW occur when the spin waves propagate perpendicular to the magnetization and MSBVW are when they propagate parallel to the magnetization. In addition to spin waves that propagate parallel to the film surface it is also possible to excite perpendicular standing spin waves (PSSW) across the film thickness. Note that MSSW spin waves are commonly referred to in the literature as Damon-Eshbach (DE) spin waves, after the authors of Ref. [18]. This thesis will use the two terms interchangeably. Not discussed in this thesis is another type of spin wave mode called edge modes. For further readings on edge modes see Ref. [19–22] and references therein.

In out-of-plane or normally magnetized films, the MSFVW spin waves also propagate perpendicular to the magnetization. MSFVW spin waves do not have a preferred direction of propagation along the film surface [2]. The magnetization profile of a MSFVW spin wave

11

TABLE 2.1. Classification of different spin wave modes
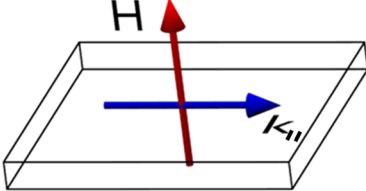
Normally Magnetized		$\mathbf{k}_\parallel \perp \mathbf{M}$	MSFVW
Tangentially Magnetized		$\mathbf{k}_\parallel \perp \mathbf{M}$ $\mathbf{k}_\parallel \parallel \mathbf{M}$	MSSW MSBVW
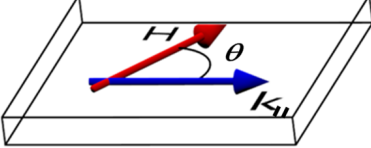
involves a standing wave profile across the thickness or volume of the film that propagates with in-plane wavevector $k_\parallel$. The group and phase velocities are both in the same direction and positive. The velocity characteristics of each spin wave group will become clear in Sec. 2.4.2, where the spin wave dispersion relations are discussed.

For in-plane or tangentially magnetized films, spin waves behave quite differently depending on whether $k_\parallel$ is perpendicular or parallel to the magnetization. Spin waves in the former geometry are called MSSW spin waves and spin waves in the latter geometry are called MSBVW spin waves. In the MSSW geometry, the magnitude of the magnetization precession decays exponentially across the film thickness. For a rather "thick" thin film, where the spin wave wavelength is comparable to the film thickness, like the ones discussed in Chap. 4, only MSSW spin waves on the top surface are seen in an optical experiment because MSSW spin waves involve exponential decay of the amplitude below the surface and so the amplitude of the precession from the bottom surface spin wave is small near the top surface. The magnetization profile of MSBVW spin waves are similar to that of MSFVW spin waves: they are standing spin waves across the thickness that propagate with an in-plane wavevector $k_\parallel$. The group and phase velocities for MSSW spin waves are both in the

same direction and both are positive, whereas the group and phase velocities are in opposite directions for MSBVW spin waves.

PSSW modes are standing waves across the film thickness with a net zero wavevector in that direction. Their magnetization profile is sinusoidal and depends on their quantized mode number n along with whether the surface spins are unpinned or pinned. If the spins on the surface are free to precess, then those surface spins are said to be unpinned. For a film of thickness t, the quantized PSSW wavevector can be written as

$$\kappa_n = \frac{n\pi}{t}. \tag{2.8}$$

Pinned or unpinned boundary conditions depend on the surface properties of a particular film and must be determined experimentally [23]. This is done as either a fit of the spin wave frequencies to their dispersion relations or through measurements of their transmission loss profile from microwave measurements with a network analyzer. Both of these methods are used in this thesis.

Figure 2.3 shows an illustration of the magnetization profiles for the MSSW or DE mode and the first two PSSW spin wave modes for unpinned surface spins. The MSFVW and MSBVW modes have similar thickness profiles as the PSSW modes but also propagate with wavevector $k_\parallel$.

2.4.2. DISPERSION RELATIONS. Detailed calculations of the spin wave dispersion relations are presented in Ref. [24] and [25]. A summary of these references are presented in Ref. [26]. The dispersion relations are derived from the torque equation (Eq. 2.4) using a "driving force" to excite the magnetization. The torque equation is then solved for following Maxwell's equations by applying the appropriate boundary conditions. For the MSFVW

DE   PSSW1   PSSW2
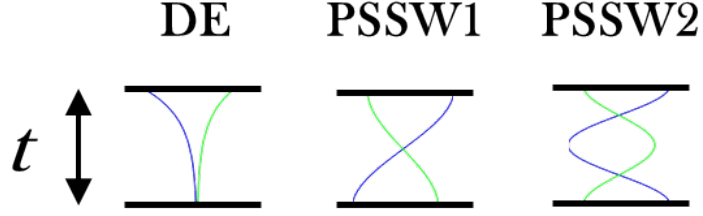
FIGURE 2.3. Magnetization profiles for a film of thickness t. The DE mode has an exponential decay as a function of depth while the PSSW modes are standing spin waves.

geometry, the spin wave dispersion relation is

$$\omega_{out-of-plane}^2 = (\omega_0 + \alpha\omega_M k_n^2)(\omega_0 + \alpha\omega_M k_n^2 + \omega_M P_n). \tag{2.9}$$

For external magnetic fields applied in the plane of the film, the dispersion relation is

$$\omega_{in-plane}^2 = (\omega_H + \omega_M + \alpha\omega_M k_n^2 - \omega_M P_n)(\omega_H + \alpha\omega_M k_n^2 + \omega_M P_n \sin^2\theta). \tag{2.10}$$

Here

$$\omega_0 = \omega_H - \omega_M, \tag{2.11}$$

and

$$k_n^2 = k_\parallel^2 + \kappa_n^2. \tag{2.12}$$

α is the exchange parameter and θ in Eq. 2.10 is the angle that is formed by $k_\parallel$ relative to the magnetization and ranges from 0 to $\pi/2$. $\theta = \pi/2$ is for MSSW spin waves and $\theta = 0$ is for MSBVW spin waves. Angles between 0 and $\pi/2$ form what is called the spin wave manifold [2]. k_n is the total spin wave wavevector, which contains wavevector components that are parallel to the film surface $k_\parallel$ and perpendicular to the film surface κ_n. The latter is quantized across the film thickness, as described by Eq 2.8.

14

The P_n terms in Eq. 2.9 and 2.10 represents the dipolar boundary conditions for unpinned and pinned surface spins and are given as

$$P_n = \frac{k_\parallel^2}{k_n^2} - \frac{2}{k_\parallel t} \frac{k_\parallel^4}{k_n^4} \frac{1}{1 + \delta_{0n}} \left[1 - (-1)^n e^{-k_\parallel t} \right] \tag{2.13}$$

for unpinned surface spins and

$$P_n = \frac{k_\parallel^2}{k_n^2} + \frac{2}{k_\parallel t} \frac{k_\parallel^2 \kappa_n^2}{k_n^4} \left[1 - (-1)^n e^{-k_\parallel t} \right] \tag{2.14}$$

for pinned surface spins. For unpinned surface spin, $n = 0, 1, 2, 3, \cdots$ and for pinned surface spin $n = 1, 2, 3, \cdots$.

Calculated MSFVW, MSSW, and MSBVW dispersion relations for unpinned and pinned surface spins based on Eq. 2.9-2.14 are shown in Fig. 2.4, 2.5, and 2.6, respectively. The unpinned dispersion relations are shown for the $n = 0$ mode as well as the first 5 nonzero modes. The pinned dispersion relations are shown for the first 5 modes.
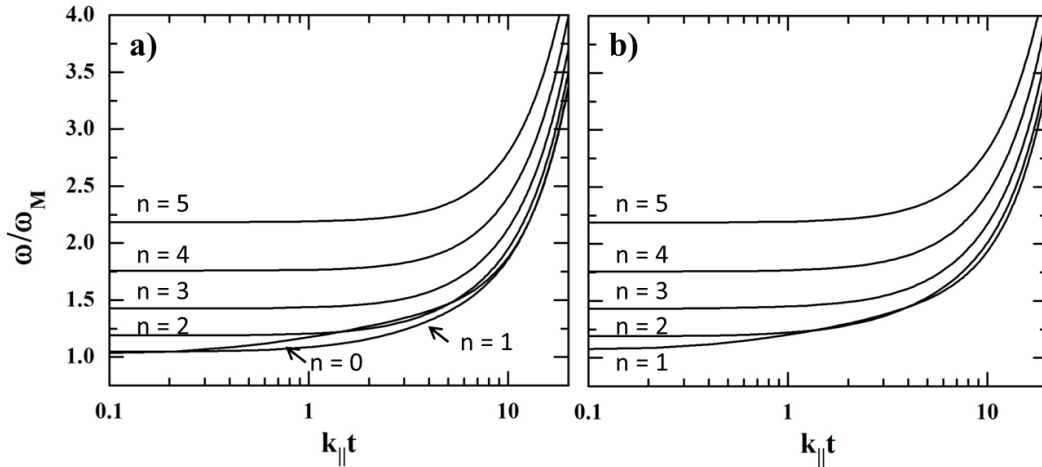
FIGURE 2.4. Calculated MSFVW dispersion relation for a) unpinned and b) pinned surface spins. The calculations were made using parameters typical for YIG: $t = 0.25$ μm, $\alpha = 3.0 \times 10^{-12}$ cm^2, and $\omega_H/\omega_M = 2$.
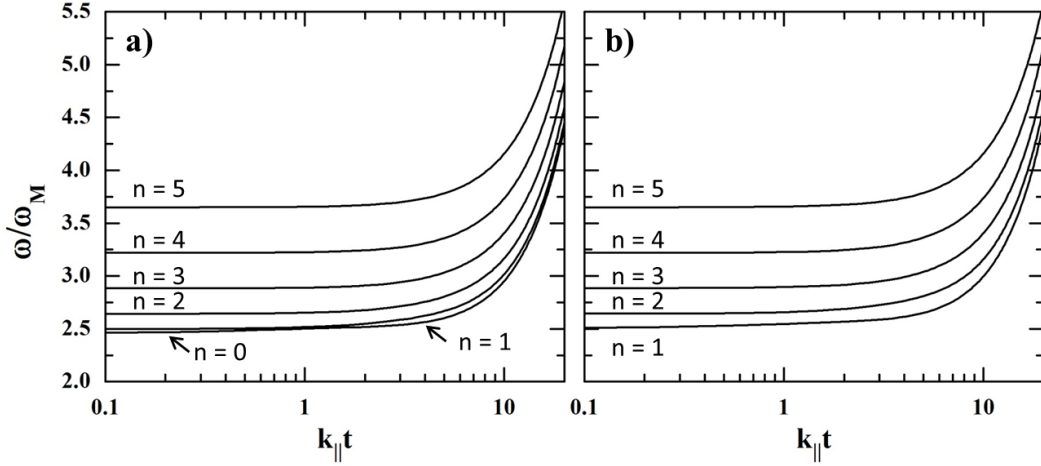
FIGURE 2.5. Calculated MSSW dispersion relation for a) unpinned and b) pinned surface spins. The calculations were made using parameters typical for YIG: $t = 0.25 \ \mu\text{m}$, $\alpha = 3.0 \times 10^{-12} \ \text{cm}^2$, and $\omega_H/\omega_M = 2$.
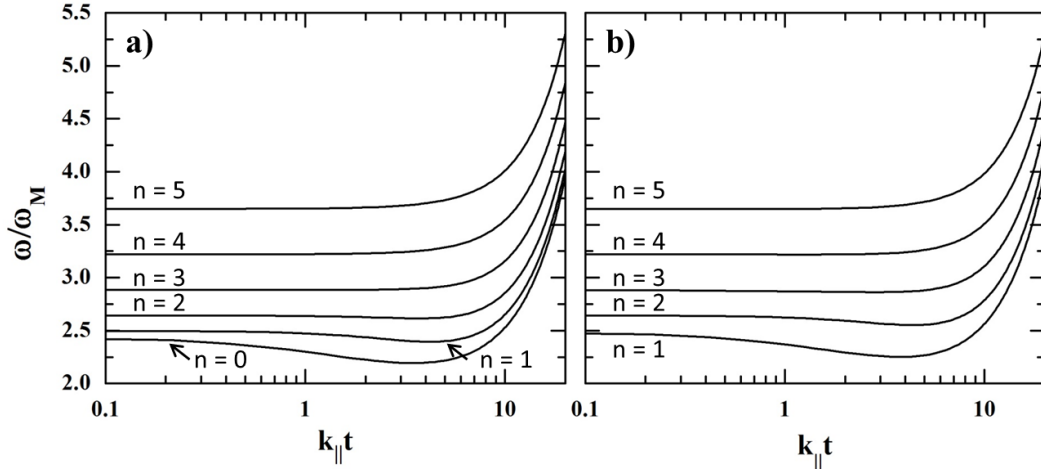
FIGURE 2.6. Calculated MSBVW dispersion relation for a) unpinned and b) pinned surface spins. The calculations were made using parameters typical for YIG: $t = 0.25 \ \mu\text{m}$, $\alpha = 3.0 \times 10^{-12} \ \text{cm}^2$, and $\omega_H/\omega_M = 2$.

The dispersion relations are plotted on a log scale for $k_\parallel t$. At large $k_\parallel t$, the frequencies of all spin wave modes converge. These are short wavelength spin waves ($\lambda \ll t$). The dominant energy term for these spin waves is exchange, thus, they are called exchange spin waves. Long wavelength spin waves are dominated by the dipole-dipole energy term and are called dipolar spin waves. Between these two types of spin waves are what is called dipole-exchange spin

16

waves. Dipole-exchange spin waves are most noticeable in the MSBVW dispersion relation, Fig. 2.6, where the curves "dip" before entering the exchange regime.

The group velocity can be calculated from the dispersion relation as $v_g = d\omega/dk_\parallel$ and the phase velocity as $v_p = \omega/k_\parallel$. The phase velocities are all parallel to $k_\parallel$ and thus positive. The group velocity is positive for the MSFVW and MSSW spin waves. The group velocities for the MSBVW spin waves are negative for dipolar spin waves but positive for exchange spin waves.

Useful forms of Eq. 2.9 and 2.10 are:

$$\omega^2_{MSFVW} = \omega_0 \left[\omega_0 + \omega_M \left(1 - \frac{1 - e^{-k_\parallel t}}{k_\parallel t} \right) \right], \tag{2.15}$$

$$\omega^2_{MSSW} = \omega_H(\omega_H + \omega_M) + \frac{\omega^2_M}{4}(1 - e^{-2k_\parallel t}), \tag{2.16}$$

$$\omega^2_{MSBVW} = \omega_H \left[\omega_H + \omega_M \left(\frac{1 - e^{-k_\parallel t}}{k_\parallel t} \right) \right], \tag{2.17}$$

and

$$\omega^2_{PSSW} = (\omega_H + \alpha\omega_M k_n^2)(\omega_H + \omega_M + \alpha\omega_M k_n^2). \tag{2.18}$$

These forms are useful for calculating the lowest order $(n = 0)$ propagating mode with pinned surface spins. The PSSW modes for specific geometries can also be calculated independently. Full theories of spin wave dispersion relation calculations can be found in Ref. [25] and [27]

2.5. Conclusions

In conclusion, the FMR frequency and the spin wave dispersion relations for thin films were presented. By examining the FMR frequency of a magnetic system as a function of either H or ω, one can gain insight into the material's magnetic properties, such as damping. The spin wave dispersion relations are of interest for a number of reasons. Among those reasons are their dependence on the quantum mechanical exchange parameter α. As will be seen in Chap. 6, the dispersion relations can be modified for microstrips which can be useful as spin wave waveguides.

CHAPTER 3

Experimental Setup of the Conventional and Micro-Brillouin Light Scattering Apparatus

3.1. Introduction

Light scattering, as a general technique, has been used for many decades to measure properties of gases, liquids, and solids. The technique of light scattering is rather simple: scatter light off of a sample and measure the properties of the scattered light. The properties of the scattered light compared to the incident light gives information about the mechanisms that play a role in the scattering process. The scattering processes that are of interest in this thesis are photon-magnon interactions.

Brillouin light scattering (BLS) is an effective technique for measuring material properties because of its degree of flexibility in samples, frequency resolution, and localized spatial resolution. The focus of this thesis is to use BLS to measure spin wave excitations in thin films. BLS has proven to be a useful tool for measuring magnetic properties. BLS has also proven useful in measuring the elastic properties of water [28–31] and solids like spessartite, perovskite, and zirconate. [32–36]. Recently BLS has been used in biomedical applications to measure the elastic properties of the eyes of mice and humans because it is a non-contact tool and thus non-invasive [37–39]. These studies have shown that BLS can be used to measure phonons in water, solids, and organic materials to obtain elastic constants including the bulk modulus value.

In magnetics research, BLS has been widely used because it can be used to measure spin wave properties, particularly, spin wave frequencies or dispersion relations. As discussed in Chap. 2, the spin wave dispersion relations rely on material parameters, and obtaining

information about the dispersion relations can be a useful means to extract those parameters. In Chap. 4, 5, and 6, the reader should refer to the references therein regarding the use of BLS to measure material parameters, nonlinear effects, and effects on spin wave confinement. Other areas of magnetic research include: magnonic gases [40, 41], spin-transfer-torque [42–48], and magnonic crystals [49–53]. BLS has been used in each of these research areas to measure spin waves. In magnonic gases, BLS was used to observe the parametrically excited $2f_p$ magnons. In the spin-transfer-torque measurements, the spin waves generated by the spin polarized current produced by multilayer stacks were observed. In magnonic crystals, BLS was used to measure the spin wave dispersion relations and band gaps corresponding to forbidden spin wave frequencies were observed.

In this chapter, the light scattering processes are reviewed in Sec. 3.2 which includes a short discussion of the effects of the polarization of the incident photons scattered from magnetic materials. Section 3.3 discusses the BLS apparatus including the tandem Fabry-Perot interferometer and the two different light scattering configurations: the conventional BLS and the recently designed micro-BLS.

3.2. Light Scattering

The light scattering process can be divided into two main categories: the elastic and inelastic scattering of photons. The elastic scattering of photons are events for which the photon's energy or frequency is unchanged. Rayleigh scattering is an example of an elastic scattering process. The inelastic scattering of photons, where the photon's frequency has been shifted due to scattering from other quasi-particles, forms the basis of the spin wave detection method used in this thesis. Two similar inelastic scattering methods, Raman and Brillouin, are discussed in the following two subsections.

3.2.1. RAMAN SCATTERING. Raman scattering, named after its founder [54], is the inelastic scattering of photons due to interactions with a system's rotational or vibrational degree of freedom. This interaction leads to either a decrease or increase in the scattered photon's energy. The former is called Stokes scattering and the latter is called anti-Stokes scattering. Both processes require that energy conservation laws be obeyed between all scattered particles; it is called inelastic because the energies of the photons are not conserved and go into either quasi-particle creation or annihilation.

To visualize this process, consider Fig. 3.1, which illustrates Raman scattering using a transition energy level diagram. The first transition in each scattering process starts off with an incident photon of energy $E_I = \hbar\omega_I$. Here $\hbar$ is the reduced Planck constant $h/2\pi$ and ω_I is related to the incident photon frequency by $\omega_I = 2\pi f_I$. In the Stokes scattering process, the system "absorbs" some of the incident photon's energy; E_0 in the figure. The final energy of the scattered photon is $E_s = E_I$ - E_0. The anti-Stokes scattering process is opposite, where the scattered photon "gains" energy from the system resulting in $E_s = E_I$ + E_0. The Rayleigh scattering energies are as expected: unchanged in energy at E_I.
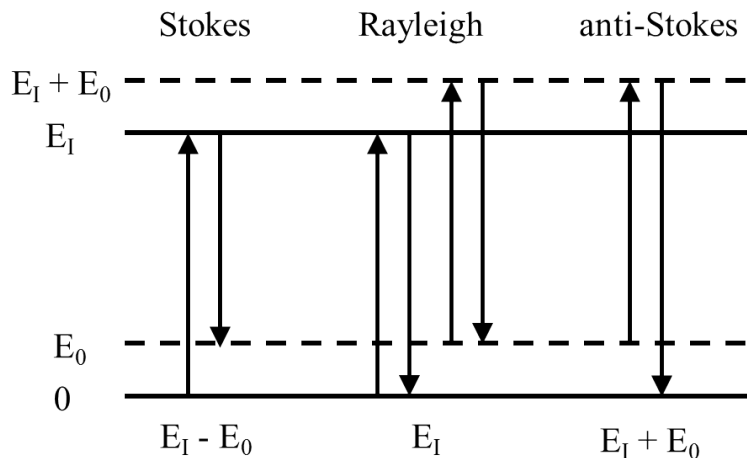
FIGURE 3.1. Transition energy level diagram illustrating Rayleigh and Raman scattering.

3.2.2. BRILLOUIN SCATTERING. Brillouin scattering, first theorized by Brillouin in 1922 [55], is a specific type of Raman scattering. It is the inelastic scattering of photons by means of translational excitations in a system that has momentum. The inelastic scattering processes are still referred to as Stokes and anti-Stokes. Along with energy conservation, momentum is another quantity that is conserved in Brillouin scattering. In the case of spin waves, magnetic excitations, the relationship between energy and momentum is given by the dispersion relations presented in Chap 2.

Figure 3.2 shows the Stokes and anti-Stokes scattering processes involving photons and the spin wave quanta, magnons. In both cases, the incident photon has frequency $\hbar\omega_I$ and wavevector $\hbar\mathbf{q_I}$. For Stokes scattering, a magnon with energy $\hbar\omega_m$ and momentum $\hbar\mathbf{k_m}$ is said to be created and the scattered photon loses energy $\hbar\omega_s = \hbar(\omega_I - \omega_m)$, as with Raman scattering, and undergoes a change in momentum of $\hbar\mathbf{q_s} = \hbar(\mathbf{q_I} - \mathbf{k_m})$. When a magnon is annihilated, the anti-Stokes process, the scattered photon gains energy $\hbar\omega_s = \hbar(\omega_I + \omega_m)$ and momentum $\hbar\mathbf{q_s} = \hbar(\mathbf{q_I} + \mathbf{k_m})$.

3.2.3. MAGNETO-OPTIC KERR EFFECT. The magneto-optic Kerr effect (MOKE) was discovered by Kerr in 1877 [56]. When linearly polarized light is incident on a magnetic material, the reflected or scattered light is elliptically polarized. This is illustrated in Fig. 3.3. In both (a) the polar and (b) the longitudinal MOKE geometries, the reflected light is elliptically polarized. For the case of (c) transverse MOKE, the reflected light is linearly polarized but its amplitude is changed. MOKE involves the same underlying physics as the Faraday effect and both involve a rotation of polarization, the former of reflected light while the latter deals with transmitted light.

The ellipticity of the reflected light can be calculated by applying the appropriate boundary conditions from Ref. [15]. The permittivity tensor, which describes how a material will
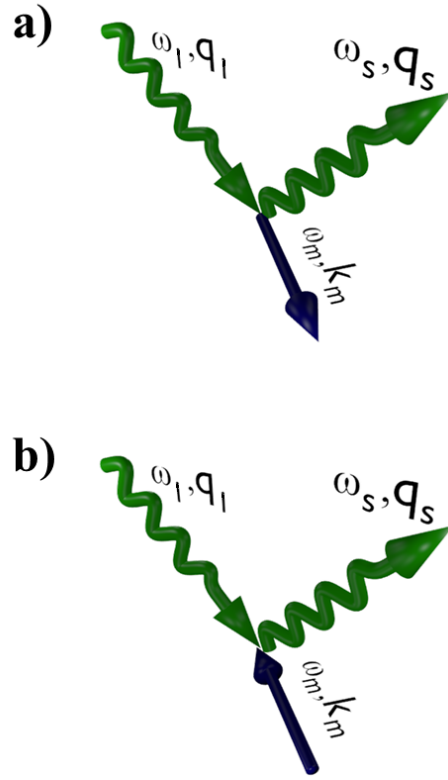
FIGURE 3.2. a) Stokes and b) anti-Stokes scattering processes of photons with magnons.
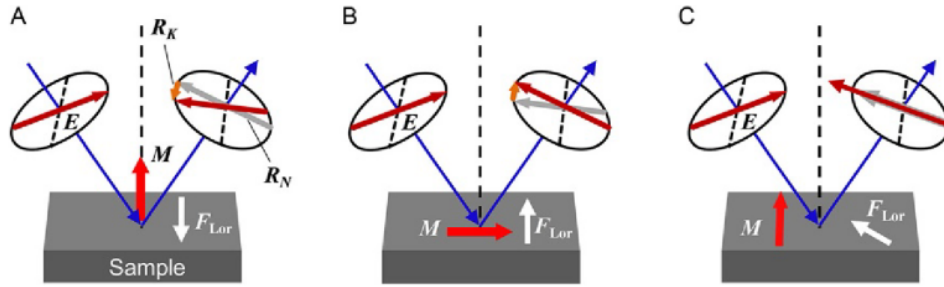
FIGURE 3.3. The MOKE shown for three different configurations of the magnetization: a) is when the magnetization is perpendicular to the plane of the sample (polar MOKE), b) is when the magnetization is parallel to the plane of incidence (longitudinal MOKE), and c) is when the magnetization is perpendicular to the plane of incidence (transverse MOKE) This figure was reproduced from Ref. [57] with permission from Elsevier.

react under the influence of an electric field, will have off diagonal elements that contain effects of the magnetization. One finds that magnetic materials are birefringent: the speed of light is different for left and right circularly polarized light. This causes the reflected

23

light to be elliptically polarized. In the case of spin waves, the propagating magnetic field of the incident light couples with the spin waves, so MOKE can be used to extract spin wave information.

3.3. Brillouin Light Scattering Apparatus

The BLS apparatus is used for measuring the small frequency shifts in the gigahertz regime. The apparatus consists of many optical components including a solid state laser with a wavelength of 532 nm and a tandem Fabry-Perot interferometer. Although all optical components play a role in the apparatus, this thesis will only focus on the most crucial aspects. The experimental BLS apparatus is shown in Fig. 3.4. Figure 3.4(a) shows the beam path that originates from the laser and (b) shows the tandem Fabry-Perot (TFP) interferometer that is used to measure the spin wave frequencies. The TFP will be described in the following subsection and the microscope setup will be expanded on in the final subsection.

The laser is a 200 mW Excelsior laser from Spectra-Physics. The laser is single mode and is linearly polarized perpendicular to the plane of the optical table. The light is directed towards a magnetic sample. The scattered light is collected and directed towards the TFP. Typically a polarizer is inserted in the path of the scattered light, set such that it passes light perpendicular to the incident laser polarization. Since the scattered light from a BLS measurement contains mostly elastically scattered light and light of the same polarization as the laser, the polarizer blocks out light of unaffected polarization. Photons that have scattered from magnons have a component normal to the original polarization that is transmitted through the polarizer.

3.3.1. Fabry-Perot Interferometer. The specific interferometer used for BLS is a Fabry-Perot interferometer. A Fabry-Perot interferometer is used in BLS because the
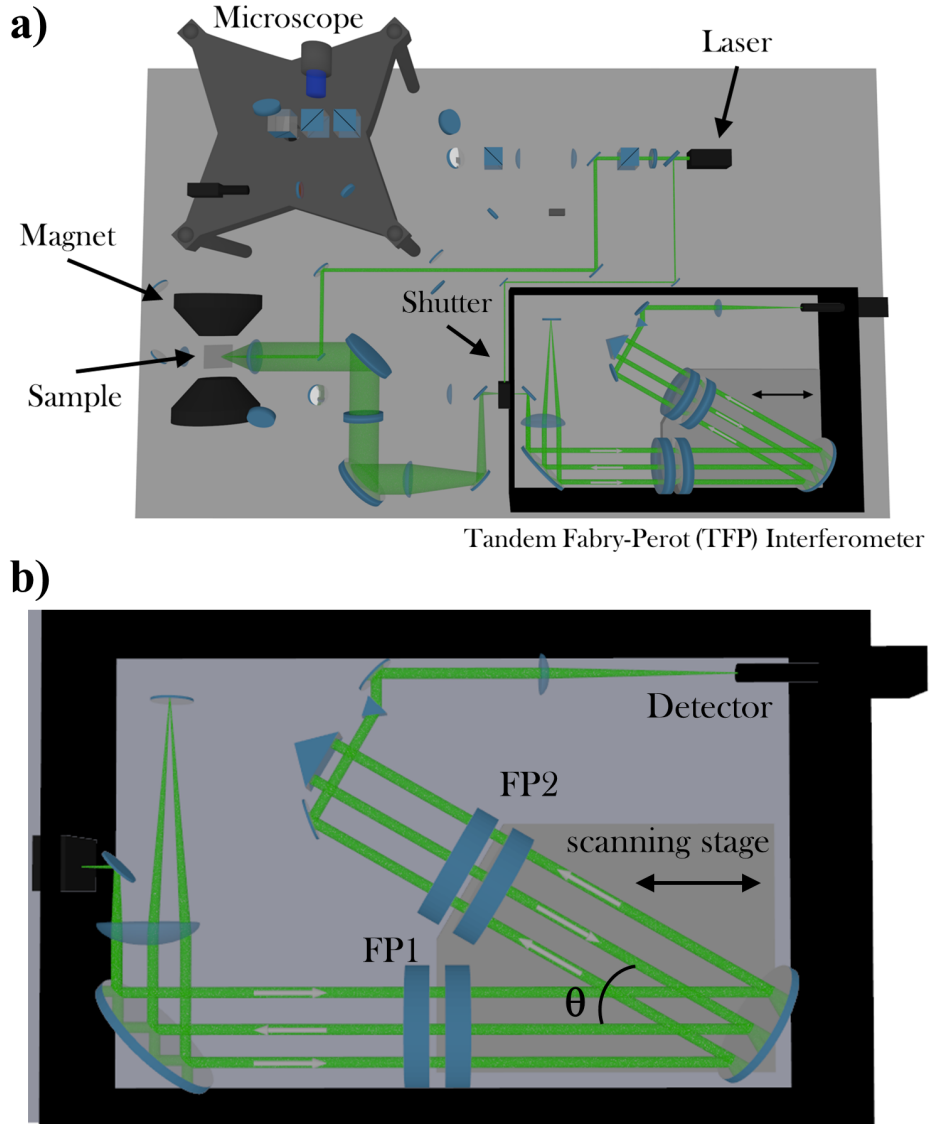
FIGURE 3.4. a) General setup of the optics and instruments used in a BLS experiment and b) tandem Fabry-Perot (TFP) interferometer used for measuring the spin wave frequencies. The optical pathway shown in a) is for the backward scattering geometry. Not shown is the software that is required to run the experiment. The black arrow in b) indicates the scan direction of the piezoelectic stage (shaded region). θ is the angle formed by the normal of the two interferometers.

frequency shifts of the scattered light from spin waves is typically on the order of 1-20 GHz. The free spectral range, discussed below, corresponds to this frequency range with a 532 nm laser. The interferometer is commonly misnamed as a Fabry-Perot etalon. Although similar, they have different definitions. The definitions and an explanation on the basics of

an interferometer can be found in Ref. [58]. An interferometer uses two highly reflective mirrors facing each other and has air between them, while an etalon is typically two highly reflective surface at a fixed distance apart with something other than air between them. The interferometer has the ability to scan through different frequencies because the spacing between the mirrors can be adjusted. In this thesis it is an interferometer and not an etalon.

A single Fabry-Perot interferometer consist of two plane mirrors that are parallel to each other. The mirrors are separated by a distance d_m. The surfaces of the mirrors facing each other are coated with silver and typically have around a 95 percent reflectivity. When light enters the interferometer, it goes through multiple reflections and the light will interfere constructively or destructively depending on the phase difference between the incident light and the reflected light. The phase difference is given as [58]

$$\delta = \left(\frac{2\pi}{\lambda}\right) 2d_m, \tag{3.1}$$

where λ is the wavelength of the incident light, which remains unchanged for the reflected light. For constructive interference, the incident light and the reflected light will be in phase ($\delta = 2\pi n$). This corresponds to a mirror spacing of $d_m = n\lambda/2$. Here $n = 0, 1, 2, 3, \ldots$. By scanning the distance, light of a particular frequency will constructively interfere and be transmitted. The frequencies of light that BLS will observe will be shifted by spin waves.

Figure 3.5 shows transmission spectra for a TFP. For a single Fabry-Perot interferometer, consider only the top spectrum (FP2). The separation between peak transmission intensities is called the free spectral range (FSR). The FSR is related to the mirror spacing as

$$FSR(frequency) = \frac{c}{2d_m}. \tag{3.2}$$

in units of frequency, where c is the speed of light in a vacuum. Equation 3.2 can be written in terms of wavelength λ using $c = \lambda f$:

$$FSR(wavelength) = \frac{\lambda^2}{2d_m},\qquad (3.3)$$

where f is the frequency of the incident light. The full width half maximum of the transmission peak $\delta\lambda$ is known as the resolution. The smaller the width, the better the resolution. The relationship between the FSR and the resolution is known as the finesse $\mathcal{F}$ and is given as

$$\mathcal{F} = \frac{FSR}{\delta\lambda}.\qquad (3.4)$$
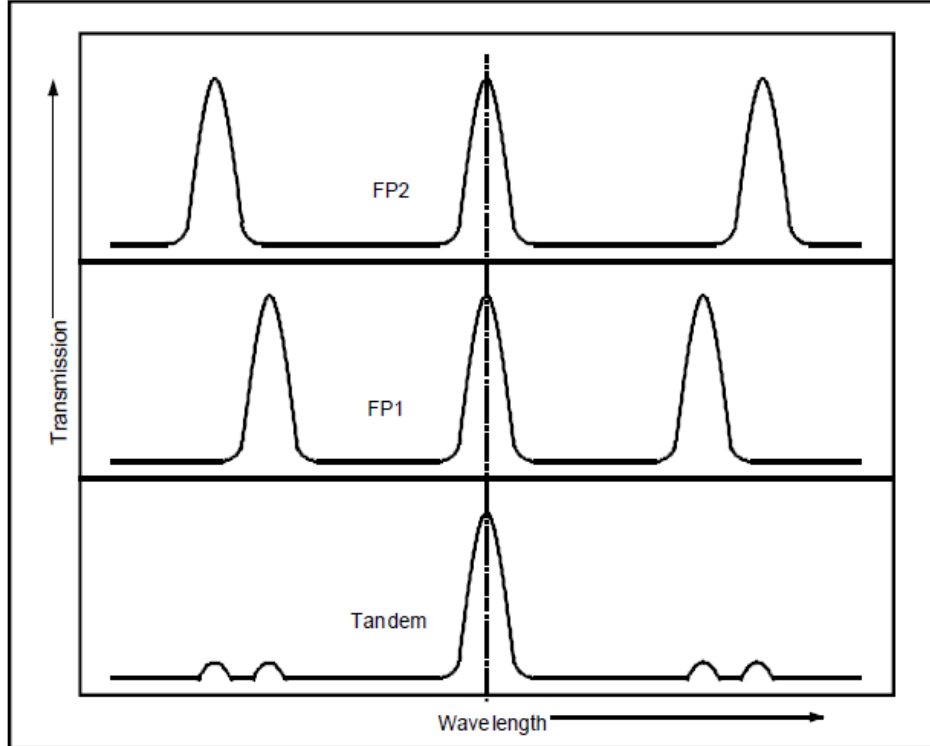
FIGURE 3.5. Transmission spectra for a tandem Fabry-Perot interferometer. This figure was reproduced from Ref. [59].

The tandem Fabry-Perot interferometer was developed by Sandercock [60] and is shown in Fig. 3.4(b). The TFP has gone through many iterations during its development [61]; only the current design is discussed here. The TFP is designed as a multi-pass interferometer, where the beam from either the scattered light or from the reference light passes through each interferometer three times for a total of six passes before being detected. There are two basic ideas to the TFP. First, the multiple passes of the beam through each Fabry-Perot interferometer allows better signal-to-noise compared to a single pass by reducing the stray light. [62]. The second idea is illustrated in Fig. 3.5. This idea addresses the shortcoming of a single Fabry-Perot interferometer: increasing the FSR by decreasing the mirror spacing decreases the resolution. In a tandem configuration, the mirror spacing of FP2 is related to the mirror spacing of FP1 by

$$d_{m,FP2} = d_{m,FP1} \cos \theta. \tag{3.5}$$

The angle θ is formed from the normals on the two interferometers and is shown in Fig. 3.4(b). The nonzero interference modes from FP1 are suppressed when the transmitted light passes through FP2. This happens in the same manner when light from FP2 passes through FP1. This results in an increase in FSR without any reduction in resolution. The tandem spectrum is shown in the lower panel of Fig. 3.5.

The TFP is configured as a scanning interferometer, where slight adjustments to the mirror spacing are achieved through piezoelectic devices connected to a scanning stage. The scan stage is shown in Fig. 3.4(b) where the black arrows show the scan direction. This allows the interferometer to scan through a range frequencies centered at the frequency of the laser. Note the double shutter shown in Fig. 3.4. The double shutter is set up to allow only inelastically scatter light from the sample to enter the interferometer. When the scan stage scans through an interference mode that corresponds to elastically scattered photons, the

shutter blocks the scattered light and allows a diffused reference beam from the laser to enter the interferometer instead. By measuring the finesse of the interferometer using reference beam the parallel-ness of the TFP mirrors can be achieved through a software-controlled stabilization routine discussed in the following subsection. Light scattered off of magnons is directed into the TFP in two configurations: conventional and micro-BLS.

3.3.2. CONVENTIONAL BLS. There are two light scattering geometries used in the conventional BLS: backward and forward scattering. The term conventional comes from the usage of BLS before the development of the micro-BLS, discussed in Sec. 3.3.3, and because it is the typically used BLS configuration.

The backward scattering geometry is typically used when working with materials that are opaque or on opaque substrates; e.g., metals. In this geometry, shown in Fig. 3.6, the incident light is focused on the sample by a lens and the scattered light is collected by the same lens and is then sent to the interferometer to be analyzed. The light that is analyzed by the TFP has scattered through an angle of 180° as compared to the incident light. As will be seen in Chap. 4, this geometry allows one to select the wavevectors to be measured through selection of the angle of incidence.

For transparent samples, like YIG, the forward scattering geometry is frequently used. Figure 3.7 shows an illustration of the forward scattering configuration. In this geometry, a lens is used to focus the incident light onto the sample and another lens is used to collect the light that is transmitted through the sample.

The backward and forward scattering geometries both have advantages and disadvantages. First, if the sample is completely opaque to the wavelength of the laser, then the backward scattering must be used. For samples that have some degree of transparency, either scattering geometry can be used. In this case, the advantage of using forward scattering
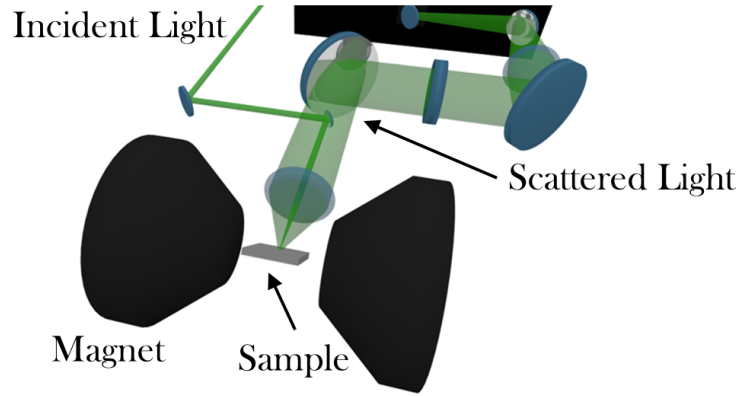
FIGURE 3.6. Light scattering setup of the conventional backward scattering geometry. In this geometry, light is focused onto the sample with a lens and the back-scattered reflected light is collected from the same lens and sent to the interferometer to be analyzed.
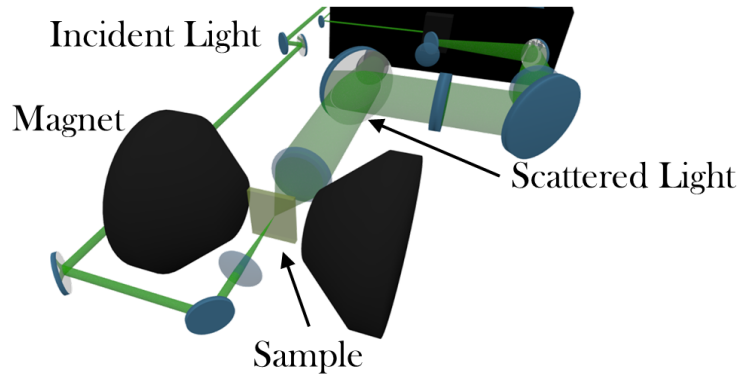
FIGURE 3.7. Light scattering setup of the conventional forward scattering geometry. In this geometry, a pair of lens are used: one to focus the incident light and another to collect the scattered transmitted light.

is that the signal-to-noise improves because much more of the scattered light is collected. The drawback is that one loses the ability to access large spin wave wavevectors by selecting a large angle of incidence.

In both of these scattering geometries, the BLS can be set up to examine specific wavevectors of the scattered light and to measure the time difference between propagating spin waves originating from the same source. The former is called wavevector selective BLS and the latter is called time-resolved BLS. Wavevector selective BLS will not be discussed in this

thesis but the reader is referred to Ref. [16, 63, 64] for more information on this specific technique. The time-resolved BLS is typically used when launching spin waves in a thin film from a microwave antenna. This is a time-of-flight technique that has a temporal resolution of 250 ps. This technique was used to obtain the results in Chap. 5 and an explanation of the time-resolved setup is contained therein.

Figure 3.8 is a screenshot of the TFPDAS4 main screen. The display includes a plot of the BLS spectrum, where the y-axis is the number of photon counts and the x-axis is the BLS frequency, simply referred to as frequency in this thesis. The displayed frequency is a frequency shift relative to the frequency of the incident photons. Therefore, zero GHz refers to photons that have a frequency corresponding to a wavelength of 532 nm. The negative frequencies make up the Stokes spectrum (magnon creation) and the positive frequencies correspond to the anti-Stokes spectrum (magnon annihilation). The peaks are shifts in frequencies and for experiments presented in this thesis are due to photon-magnon interactions, and therefore they correspond to magnon frequencies.

The red dashed vertical lines represent the boundaries of the regions of interest (ROI). The Stokes and anti-Stokes spectra both have their own ROI. The ROI sets the frequency range over which the double shutter allows in inelastically scattered light. When the TFP scans through the elastically scattered light the sample beam is blocked and the reference beam is allowed to enter the TFP. This is shown as the large peak at zero GHz. The smallest frequencies that can be measured are around 500 MHz, limited by the timing of the double shutter and the width of the reference peak.

The term complex scan is used when conducting scans where one or more variables are changed. The software allows for a maximum of three variables to be changed. An independent program that controls the variable, typically written in Labview, is connected
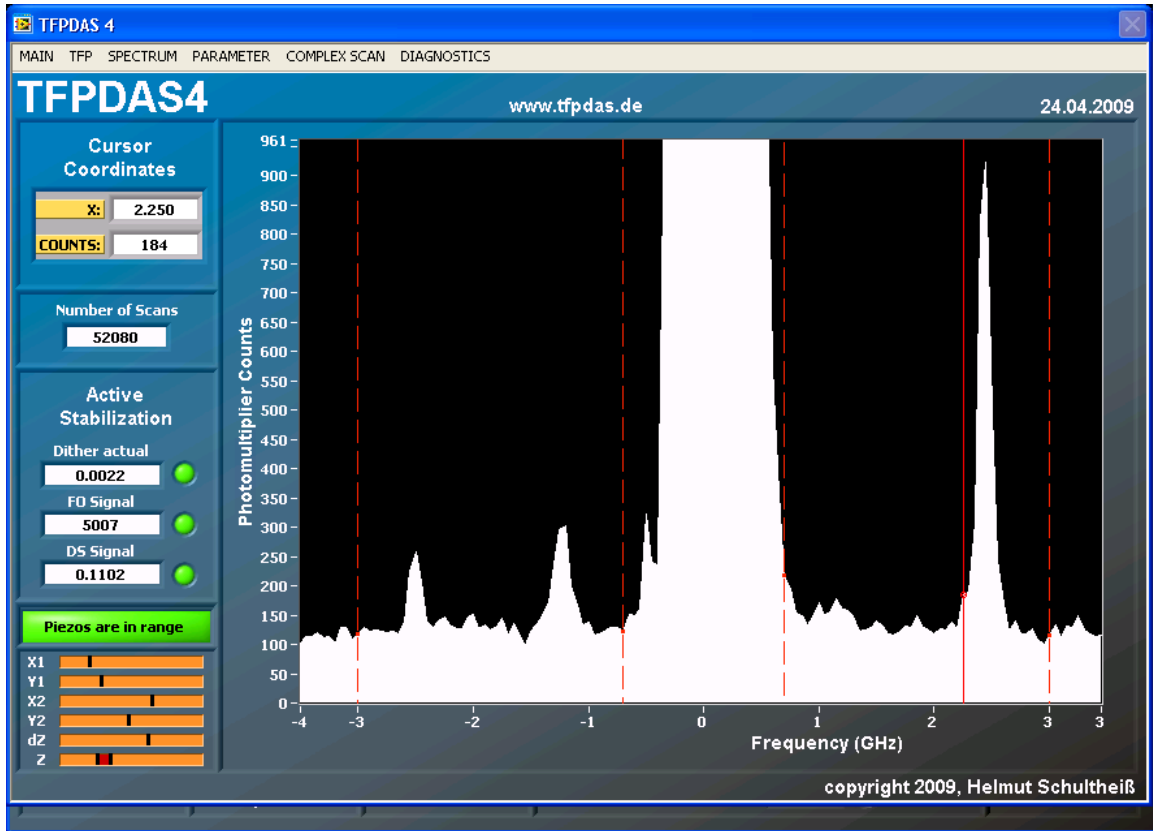
FIGURE 3.8. Screenshot of the TFPDAS4 software.

to the TFPDAS4 program through TCP protocols. In this thesis, the complex scan function in the software is used to collect BLS spectra as a function of pumping frequency, magnetic field, time, or position depending on the experiment. The user defines the step size that the variable will change by and the number of loops to run through that variable. A more detailed explanation of the operation of the software can be found in Ref. [65–67].

3.3.3. MICRO-BLS. The micro-BLS is a recent extensions to the BLS technique that has been developed within the past decade [68, 69]. The conventional BLS works well for examining spin waves in continuous films but is limited when micrometer-sized structures are introduced. The spot size of the focused laser in conventional BLS is typically tens of micrometers. This is sufficient for observing spin waves in an array of microstructures

[70, 71] but for single magnetic elements, micro-BLS would have to be used. With micro-BLS the laser spot size is approximately 250 nm. This allows for localized measurements of micrometer size structures with great signal-to-noise as compared to conventional BLS. The micro-BLS was used in Chap. 6 to measure spin waves in microstrip waveguides. The components needed to transform the BLS to a micro-BLS are shown in Fig. 3.9. These components include: a microscope objective, a CMOS camera, and a set of high precision three-dimensional translation stages.
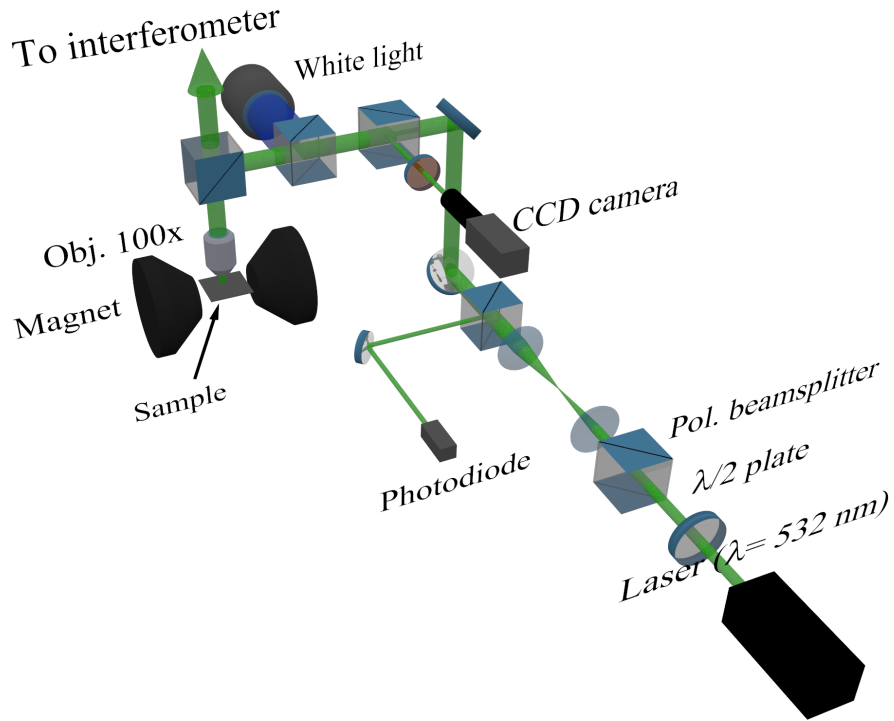
FIGURE 3.9. Setup of the optics used in micro-BLS. The essential items of the setup that vary from conventional BLS are the microscope objective, the CMOS camera, and high precision translation stages (not shown) that are used to control the sample position.

The microscope object is from Zeiss and has a magnification of 100x, a numerical aperture (NA) of 0.75, and a long working distance of 3 mm. The micro-BLS uses the backward scattering geometry without the ability to change the angle of incidence. The maximum

angle of incidence is given by the numerical aperture $NA = n \sin \theta$, where n is the index of refraction of the medium (1.00 for air) and θ is the angle of incidence. For a numerical aperture of 0.75, the corresponding maximum angle of incidence is 48.6°. Thus, the scattered light collected will range from $\theta = 0$ to 48.5°. Based on the angle of incidence, the maximum observable spin wave wavevector can be calculated from Eq. 4.1 in Chap. 4 and is 17.7 μm^{-1}.

The CMOS camera is a model DCC1545M monochromatic camera from Thorlabs. The camera plays two roles: it allows for observing the location of the laser spot on the sample and it allows for sample stabilization in order to counter thermal drift. Figure 3.10 is a screenshot of the micro-BLS software. The magnetic sample in this image is of darker contrast compared to the substrate and is shaped like a pound key. The red crosshair represents the location of the laser spot. The laser spot does not appear since its intensity would saturate the image so it is filtered out with a notch filter that is notched at a wavelength of 532 mn. The green area is a spatial scanning ROI. The ROI can be set to allow for two-dimensional spatial scans as shown. The red box represents the stabilization region where the contrast is mapped. The software monitors the contrast inside the red box and if the sample drifts then it will make small adjustments to the sample position to maintain the mapped contrast. This is important because some scans can take many hours to complete. The yellow box is a type of ROI for the red box that sets the limit on where the red box will search for the mapped contrast.

In order for the position stabilization to be effective, a set of high precision translation stages from Newport was used. The two-dimensional lateral stages were model number XMS50 and the vertical focusing stage was model number GTS30V. The lateral stages are quoted as having a precision of 1 nm and the vertical stage is quoted as having a precision
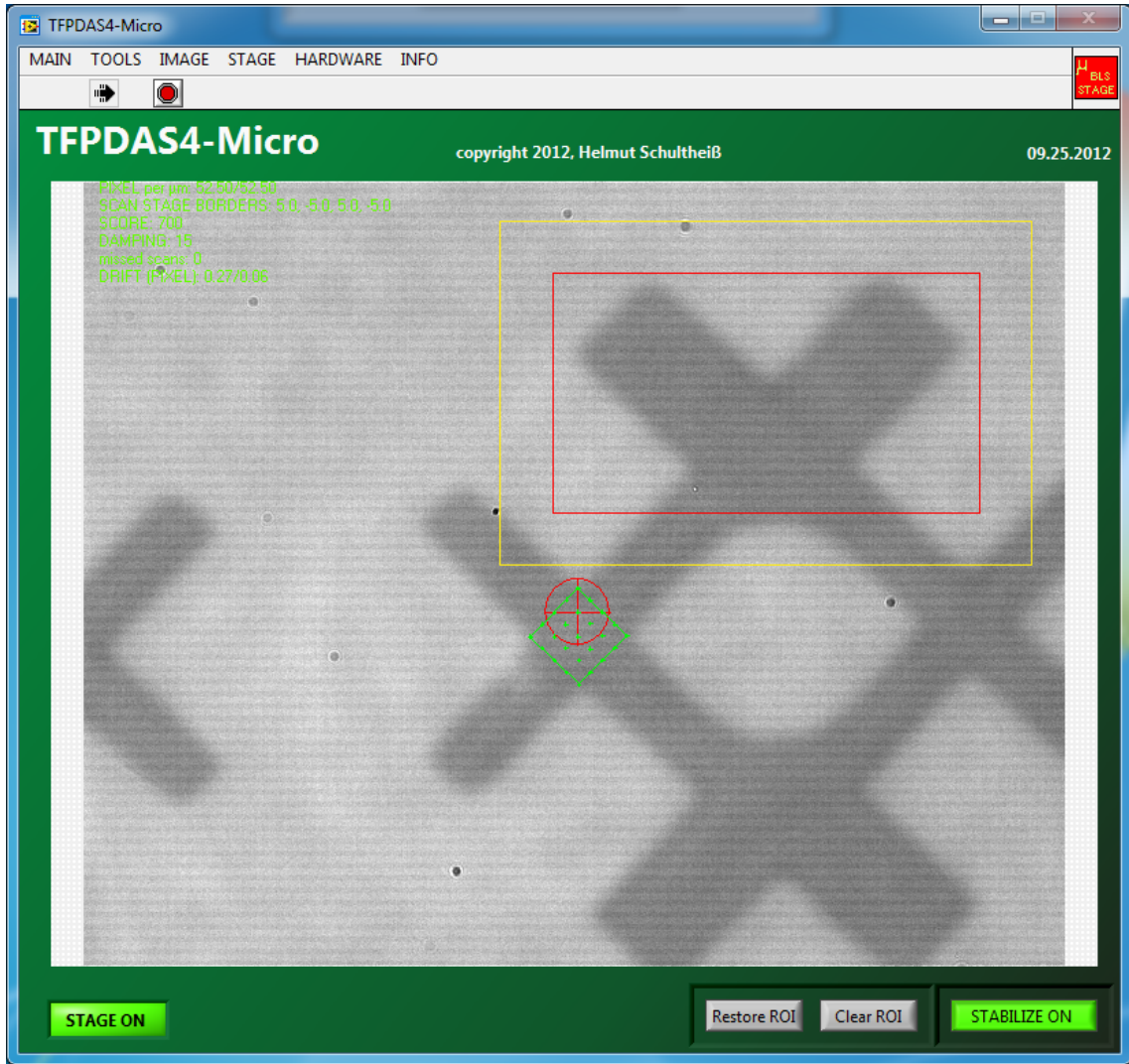
FIGURE 3.10.   Screenshot of the micro-BLS software. The size of entire pound key structure is approximately 12×12 μm^2.

of 50 nm. With these specifications, these stages are more than sufficient to correct for thermal drift and to conduct fine spatial scans. The vertical translation stage combined with a photodiode is used to automatically maintain the focus of the sample.

The micro-BLS software was written by Schulteiβ [72]. The micro-BLS software works independently from the TFPDAS4 software except when performing complex spatial scans. The software runs the stabilization and sample focusing using input from the camera, stages, and photodiode. When conducting complex spatial scans, the positions of the two lateral

stages corresponding to scan point coordinates are used as scan parameters. A more detailed explanation on the operation of the micro-BLS software can be found in Ref. [73].

3.4. Conclusions

The focus of this chapter was to examine the experimental BLS apparatus. A discussion on some important light scattering terminology was included. These terms are Rayleigh, Raman, Stokes, anti-Stokes, and Brillouin. Along with conservation of energy and momentum, MOKE is discussed. The BLS technique is broken down into two configurations: conventional and micro. The conventional BLS is an excellent choice when measuring spin waves in continuous films. When high spatial resolution is needed for microstructures, the micro-BLS is more appropriate because its resolution is hundreds of nanometers compared to the conventional BLS, which is tens of micrometers.

CHAPTER 4

Exchange Parameter of FeCo Alloys

4.1. Introduction

An important component of current magnetic recording read/write heads is $Fe_{65}Co_{35}$ (FeCo hereafter). This FeCo alloy composition is of particular interest because of its uniquely high magnetization (24.0 kG) and magnetically soft anisotropic properties [74–77]. A key magnetic parameter is the exchange parameter or simply exchange. The exchange parameter α determines the short range magnetic ordering of electron spins. The exchange parameter has been previously measured in various compositions of FeCo [78] but not for $Fe_{65}Co_{35}$.

The exchange parameter is a parameter that is mostly determined experimentally. A theoretical approach to calculating α has been proposed in the Ref. [79] and [80] but these models show only limited agreement for various metals. The experimental methods that can be used to determine α are neutron scattering [81, 82], magnetization versus temperature curves [83], coupling between two ferromagnetic layers [84], and the most common method being BLS [78, 85–88]. BLS is an excellent choice for determining α because it can be used to observe different spin wave modes, which allows the spin wave dispersion relation to be fitted to the observed spin wave frequencies.

BLS studies typically observe magnetostatic surface wave (MSSW) spin waves, commonly known as the Damon-Eshbach (DE) spin waves and perpendicular standing spin waves (PSSW) that were thermally excited at room temperature. The DE spin wave mode is a mode that propagates along the film surface, whereas the PSSW modes are standing spin waves across the thickness of the film. Quantization of the PSSW wavevector is given

as κ_n in Eq. 2.12. Fits to careful measurements of the frequencies of these spin wave modes can be used to measure α.

This chapter will present external magnetic field-dependent BLS measurements for a series of FeCo film of three different thicknesses. The observed frequencies of thermally excited DE and PSSW spin wave modes are fitted to the dispersion relations to determine the exchange parameter α and the Landé g-factor g. The fits show that surface anisotropies play a negligible role for these films and that the determined exchange parameter of $\alpha = 1.53 \pm 0.04 \times 10^{-13}$ cm^2 was much higher than the value previously used by Seagate Technologies: $\alpha = 4.42 \times 10^{-15}$ cm^2. The results in this chapter can be found in Ref. [89].

4.2. Sample and Experimental Setup

The thin film samples were provided by Seagate Technologies. Three film thicknesses were provided: $t = 125$, 173, and 250 nm. For proprietary reasons, details of how the films were fabricated was limited. They reported that the FeCo films were deposited on silicon wafers that were seeded with a 1 nm thick Permalloy (Ni$_{80}$Fe$_{20}$) film. The saturation magnetization was determined to be $4\pi M_s = 24.0 \pm 0.1$ kG using static hysteresis measurements. Some details of the fabrication can be found in Ref. [89].

The conventional backward scattering BLS configuration that is explained in Chap. 3 was used to investigate the thermal spin waves in this chapter. The conventional BLS was used because the samples were continuous films and the spatial resolution of the micro-BLS was not necessary. The mirror spacing of the interferometer was set to 3 mm, which corresponds to a free spectral range of 50 GHz. This mirror spacing proved small enough to observe the DE mode as well as several PSSW modes. The samples were opaque so a backward scattering geometry was required to measure the scattered photons. A schematic

of the scattering geometry is shown in Fig. 4.1. The samples were placed in an external magnetic field H that was perpendicular to the plane of incidence. The normal of the film was rotated at an angle $\phi > 0$ relative to the direction of the incident photons.

In this geometry, the majority of the collected photons are back-scattered 180° with respect to the incident photons, hence, DE spin waves with wavevectors

$$k = 2q_i \sin \phi \qquad (4.1)$$

are accessed. In Eq. 4.1, q_i is the wavevector of the incident photons which is equal to $2\pi/\lambda$ where $\lambda = 532$ nm. For the measurements discussed in this chapter, ϕ was held constant at 45°, which corresponds to a DE spin wave wavevector of 1.67×10^5 cm^{-1}.
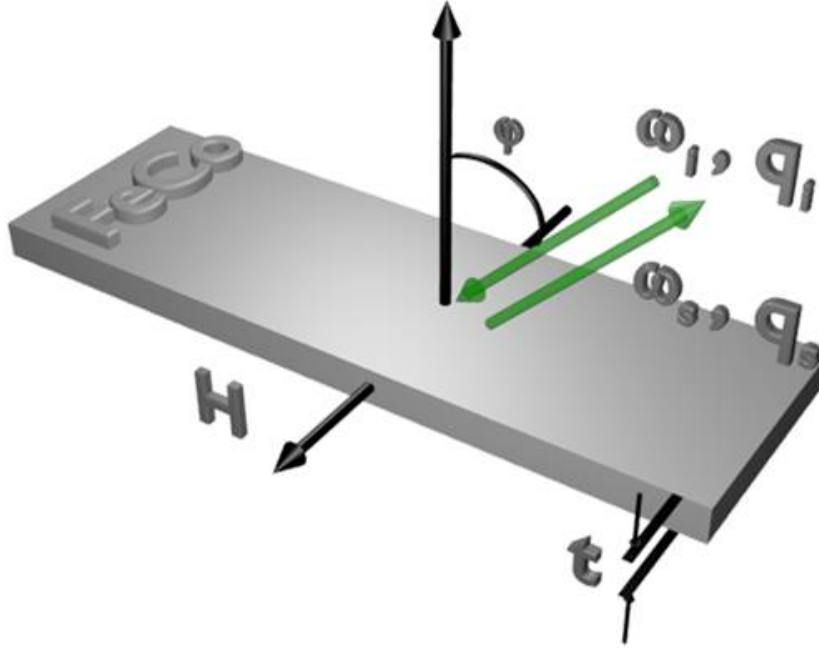
FIGURE 4.1. Illustration of the scattering geometry used for the FeCo films discussed in this chapter. The frequency and wavevector of the incident (scattered) photons are denoted as ω_i (ω_s) and q_i (q_s), respectively. H is the external magnetic field and t is the film thickness. Both of these parameters were varied.

4.3. Experimental Results

BLS spectra were collected as a function of film thickness t and external magnetic field H. The DE and PSSW spin wave modes were identified in these spectra and fitted to dispersion relations discussed in Sec. 4.4. The DE mode and the PSSW modes can be easily distinguished from one another since the DE mode has a relatively large intensity as compared to the PSSW modes and only shows up on one side of the spectra. Switching the external magnetic field direction by 180° causes the DE mode to switch to the other side of the spectrum, while the PSSW modes remain unchanged. This is due to the fact that the DE mode is a directional spin wave mode. It propagates along the film surface at a right angle to H. Since it decays exponentially across the film thickness and the skin depth of the film is rather small compared to the film thickness, only the DE mode on the top film surface is observed. The PSSW modes, on the other hand, appear on both sides of the spectra. The PSSW modes are standing spin wave modes across the film thickness and their appearance on both the Stokes and anti-Stokes sides of the spectra can be thought of as two counter-propagating spin waves with a net zero wavevector. The wavevectors of the PSSW modes are quantized and are given by Eq. 2.8.

4.3.1. External Magnetic Field-Dependent BLS Spectra. For the three film thicknesses under investigation, BLS spectra were collected to observe the spin wave frequencies as a function of H. Figure 4.2 shows the spectra for $t = 125$ nm. The data were vertically shifted to include multiple spectra on the same plot for comparison. The external magnetic field was varied from 500 to 2000 Oe in steps of 250 Oe. Representative spectra are shown in Fig. 4.2. The DE mode appears on the Stokes side of the spectra and is labeled. The PSSW modes are numbered in integer steps in increasing frequency starting from the lower

frequencies. All spin wave frequencies increase with an increase of H, which is consistent with Eq. 2.16 and 2.18.
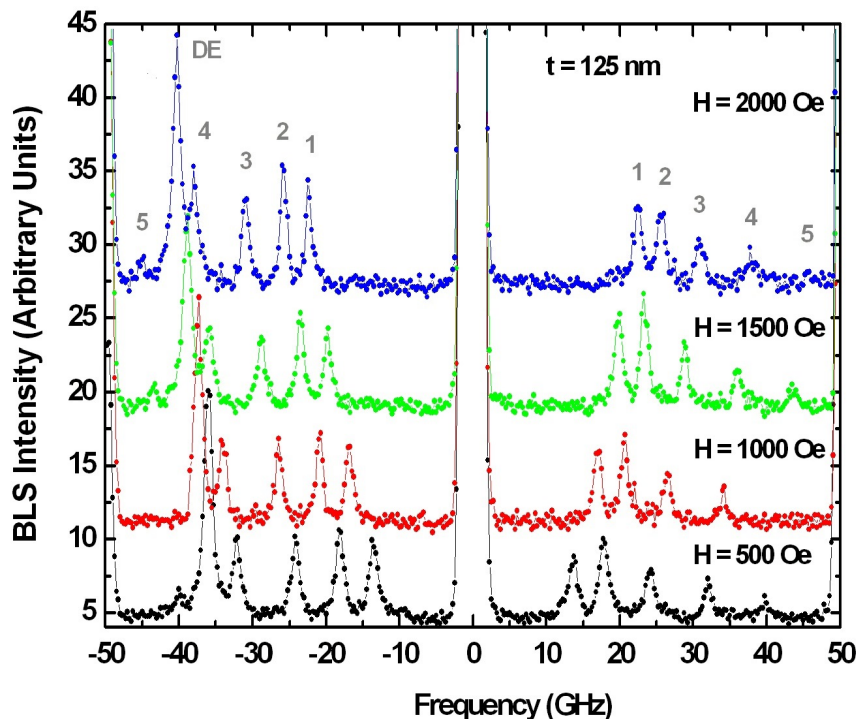
FIGURE 4.2. External magnetic field-dependent BLS spectra for a selected thickness of $t = 125$ nm. H was varied from 500 to 2000 Oe in 250 Oe steps (steps of 500 Oe are shown above). The DE mode is labeled and the PSSW modes are numbered.

4.3.2. THICKNESS-DEPENDENT BLS SPECTRA. The BLS spectra for three different thickness of FeCo in an external magnetic field of $H = 1500$ Oe are shown in Fig. 4.3. As with Fig. 4.2, the data have been shifted vertically to compare multiple spectra on the same plot. The DE mode is labeled and the PSSW modes are numbered for the two thinnest samples. With increasing film thickness, the PSSW modes decrease in frequency. The higher frequency PSSW modes have a larger change in frequency and eventually all the PSSW modes merge to form a bulk volume mode [90]. In contrast, the DE mode changes little with frequency. The cause of these thickness-dependent effects will become evident in Sec. 4.4.
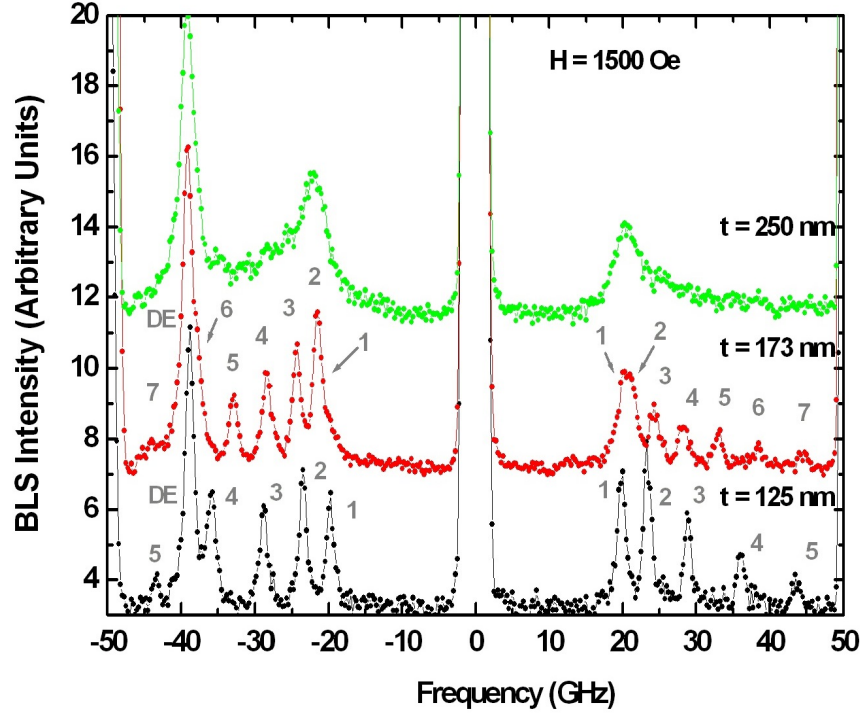
FIGURE 4.3. Film thickness-dependent BLS spectra for a fixed external magnetic field of $H = 1500$ Oe. Three film thicknesses were measured: $t = 125$, 175, and 250 nm. The DE mode is labeled and the PSSW modes are numbered.

4.4. DISPERSION RELATION FITS AND DISCUSSION

The spin wave frequencies extracted from the BLS spectra in Fig. 4.2 and 4.3 are summarized in Fig. 4.4 and 4.5, respectively. The frequencies corresponding to the Stokes spectra are plotted as black circles and the frequencies corresponding to the anti-Stokes spectra are plotted as red triangles. The frequencies were determined by performing a Gaussian fit to each of the individual peaks.

The solid lines in Fig. 4.4 and 4.5 represent fits to the data using Eq. 2.16 and 2.18. A nonlinear least squares fit was performed on the DE and PSSW modes using α and g as free parameters. Recall that g is the Landé g-factor and is related to the gyromagnetic ratio by $\gamma = g\mu_B \hbar$, where μ_B is the Bohr magneton and $\hbar$ is the reduced Planck constant. Equation 2.18 depends on both α and g and the two parameters are correlated, whereas, Eq. 2.16
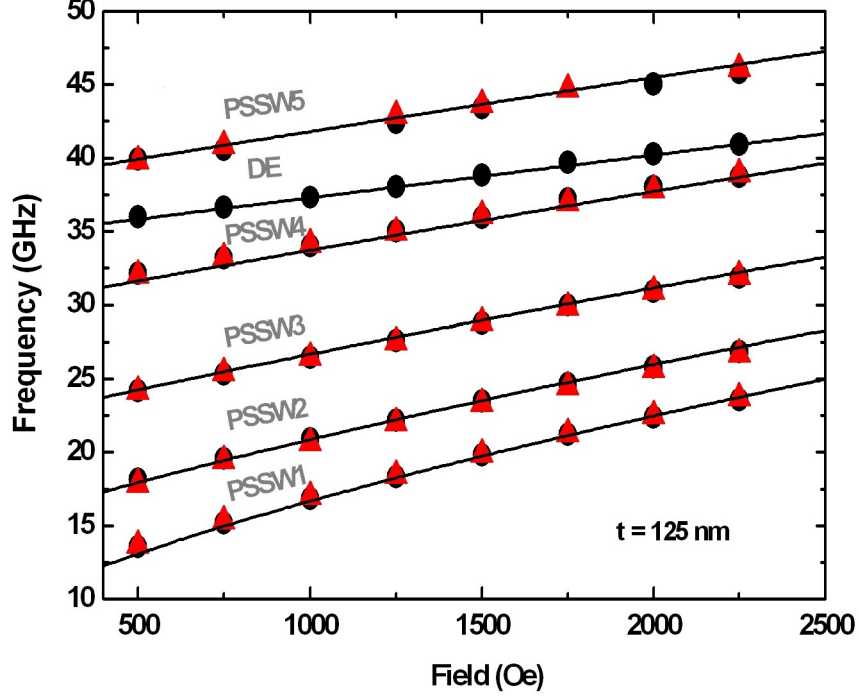
FIGURE 4.4. BLS frequencies extracted from Fig. 4.2 as a function of H for t = 125 nm. The black circles (triangles) represent frequencies from the Stokes (anti-Stokes) spectra. The solid lines are calculated fits at t = 125 nm, and using α and g as free parameters. The saturation magnetization was $4\pi M_s$ = 24.0 ± 0.1 kG. The best fit parameters for α and g are 1.53 ± 0.04 × 10^{-13} cm² and 2.07 ± 0.02, respectively

depends only on g. To eliminate the correlation between α and g, the DE mode was first fitted to Eq. 2.16 to obtain a value for g. Next, the PSSW modes were fitted for α using the previously determined value of g. The fits yield values of α = 1.53 ± 0.04 × 10^{-13} cm² and g = 2.07 ± 0.02.

The fits using Eq. 2.16 and 2.18 with unpinned surface spins agree well with the spin wave frequencies collected in this chapter, which is consistent with negligible surface anisotropies. Fits to the data were also conducted in Ref. [91] using a more involved numerical model for the dispersion relations that includes out-of-plane K_S and in-plane K_{SP} surface anisotropies [27, 92]. The surface anisotropies from these fits are K_S = 1.4 ± 0.1 erg/cm² and a K_{SP} consistent with zero. The values of α obtained from both fits were similar, hence, Eq. 2.16
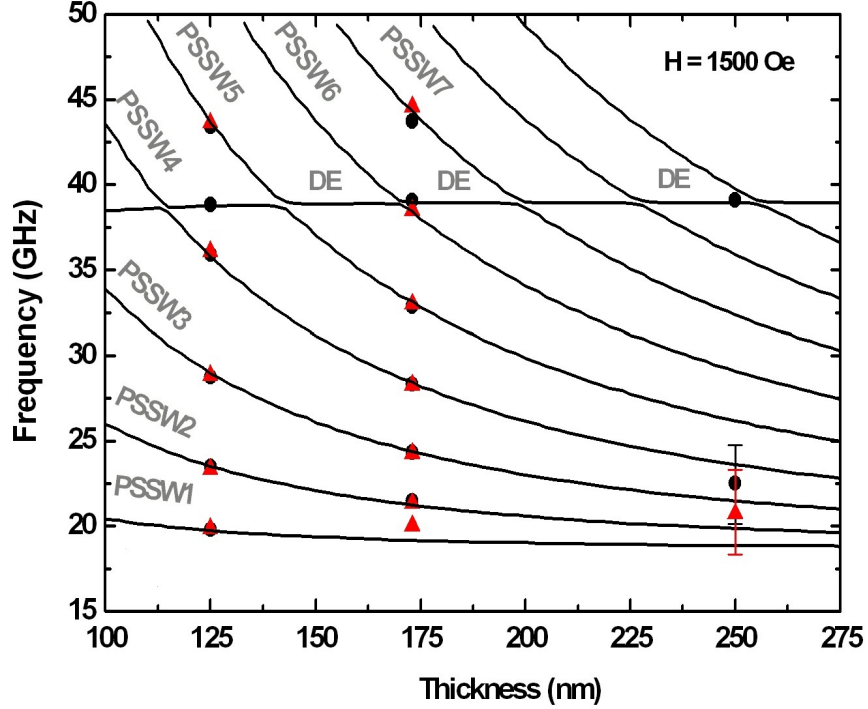
FIGURE 4.5. BLS frequencies extracted from Fig. 4.3 as a function of t for H = 1500 Oe. The black circles (triangles) represent frequencies from the Stokes (anti-Stokes) spectra. The solid lines are calculated fits at H = 1500 Oe, and using α and g as free parameters. The saturation magnetization was $4\pi M_s$ = 24.0 $\pm$ 0.1 kG. The best fit parameters for α and g are $1.53 \pm 0.04 \times 10^{-13}$ cm^2 and 2.07 ± 0.02, respectively.

and 2.18 are sufficient to describe the spin wave frequencies and the surface anisotropies are negligible. Appendix A of Ref. [88] discusses a situation where only even PSSW modes might be observed in the case that the magnetization profile of the odd modes cancel. Fits with only even PSSW modes were conducted and yielded an unrealistically low exchange parameter of $\alpha = 3.88 \times 10^{-14}$ cm^2.

Figure 4.6 shows that the value of α for Fe$_{65}$Co$_{35}$ determined in this investigation agree well with other compositions of FeCo alloys obtained from Ref. [82] and [78]. The value of g appears to be reasonable and is similar to values reported in Ref. [78] for other FeCo compositions.
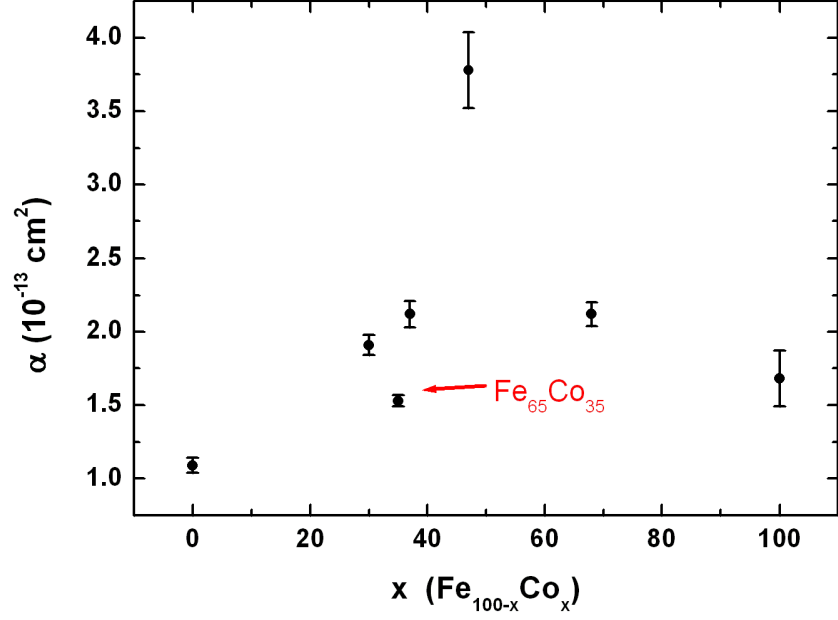
FIGURE 4.6. Comparison of exchange parameters as a function of FeCo composition. α for $Fe_{65}Co_{35}$ is labeled and was determined in this chapter. The value of α for 100 percent Fe can be found in Ref. [82] and all other value can be found in Ref. [78].

4.5. CONCLUSIONS

This chapter provided experimental results for one of the many uses of BLS: determination of the exchange parameter α. In summary, external magnetic field- and film thickness-dependent BLS spectra were collected to observe both the DE and PSSW spin wave modes $Fe_{65}Co_{35}$. The PSSW spin wave modes were observed up to the 7th order. Dispersion relations were fitted to the spin wave frequencies and yielded an exchange parameter of $\alpha = 1.53 \pm 0.04 \times 10^{-13}$ cm^2 and a Landé g-factor of $g = 2.07 \pm 0.02$. The value of α agrees well with reported values in literature and g is reasonable compared with the Landé g-factor of a free electron of 2.0 and other FeCo alloys that are typically reported slightly higher. The exchange parameter is often reported in the literature as A with units of erg/cm in CGS and units of J/m in SI. The relationship between α and A is $\alpha = 2A/4\pi M_s^2$. For completeness, α expressed as A is $3.5 \pm 0.1 \times 10^{-6}$ erg/cm in CGS and $3.5 \pm 0.1 \times 10^{-11}$ J/m in SI.

The value used by Seagate Technologies for modeling prior to this work was $A = 1 \times 10^{-6}$ erg/cm, the value of Permalloy, much different then the real value reported here.

CHAPTER 5

TIME-EVOLUTION OF NONLINEAR SPIN WAVE PROCESSES

IN YTTRIUM IRON GARNET THIN FILMS

5.1. INTRODUCTION

The magnetic properties of yttrium iron garnet (YIG), $Y_3Fe_5O_{12}$, have been extensively studied over the last few decades. A summary of past research on YIG can be found in Ref. [93]. YIG, a material that possesses a low magnetic damping parameter, has proven to be a reliable device as a bandpass filter for signal processing [94–96]. YIG is also an ideal material to study spin wave propagation because its low magnetic damping allows spin waves to propagate over millimeter distances, as will be seen later in this chapter.

Recent advances in spintronics [97–100], the use of an electron's spin degree of freedom to transfer information, has motivated new research on spin wave propagation. Of particular interest is developing a better understanding of the nonlinear processes that can be used to excite short wavelength spin waves (exchange spin waves). These spin waves are important because they typically have a higher velocity than dipole-exchange spin waves and their wavelengths are on the length scale of spintronic devices. Typically, spin waves are excited by an alternating magnetic field at microwave frequencies produced by a microstrip antenna. Two factors that can restrict the spin waves being directly excited by the antenna are the antenna width and the amplitude of the microwaves. These two restrictions will be discussed is Sec. 5.3.

This chapter will present work on two specific types of nonlinear spin wave processes in YIG; namely, the three magnon splitting and confluence processes. The three magnon splitting process involves the conversion of magnons that are pumped at frequency f_p into

two magnons (splitting magnons) both with frequency $f_p/2$. The confluence process is the reverse process, where two splitting magnons recombine to a single magnon with frequency f_c. Previous work on these processes includes mapping of the involved wavevectors by BLS [101] and the time-evolution of the splitting process by time-resolved BLS [102]. Reference [102] used wavevector selective and time-resolved BLS to observe the splitting magnons. They saw that the splitting magnons form a stationary wedge profile that has angles of about 5°-15°. Their measurements were conducted in the MSSW configuration and were not sensitive to the confluence magnons, only to the pumping and splitting magnons. Reference [101] used wavevector selective BLS and reported on the first BLS observation of confluence magnons in the MSBVW configuration. They saw that the confluence magnons propagated at 45°relative to the pumping magnons. The work presented in this chapter is the first work that reports on the time-evolution of the confluence process and will build off of Ref. [101]. Furthermore, the time-resolved BLS used in this work is superior to the technique used in Ref. [102] because magnons at all frequencies of interest were recorded in the same set of measurements. Hence, measurement of the splitting and confluence magnons in the same data set is possible. The temporal and spatial profile of the spin waves will be analyzed to determine the position away from the antenna that these processes occur and any time delay between the development of a population of splitting magnons and the onset of the confluence magnons.

5.1.1. DISPERSION RELATION AND CONSERVATION LAWS. The three magnon splitting and confluence processes are nonlinear processes that are observed above a power threshold. This power threshold is measured in Sec. 5.3.2. A way to visualize the three magnon splitting and confluence process is through applying the conservation laws using the spin wave dispersion relations. Recall that the energy and momentum of a magnon are given as

$\hbar\omega$ and $\hbar k$, respectively; these two quantities should be conserved. Note that $\omega = 2\pi f$ and $k = 2\pi/\lambda$. To satisfy energy conservation, a pumping magnon with energy $\hbar\omega$ can convert into two splitting magnons with energy $\hbar\omega/2$. It has been experimentally observed [103] that the two splitting magnons do not necessary split to exactly $\hbar\omega/2$. Conservation of energy allows for the splitting magnons to split into energies above and below $\hbar\omega/2$ as long as the sum of their energies equate to $\hbar\omega$. The pumping magnons have momentum or wavevectors near $k = 0$; this is discussed in Sec. 5.3.1. Along with energy conservation, momentum must be conserved as well. This leads to the splitting magnons to have nonzero anti-parallel wavevectors.

Figure 5.1 shows the calculated MSBVW dispersion relations for the first 5 thickness modes calculated using the parameters given in the figure caption, which include material parameters appropriate for the YIG film and the external magnetic field used for these measurements of $H = 337$ Oe. The calculation were done using unpinned surface spins in Eq. 2.10. In this case, the frequency of the pumping magnons is set at $f_p = 2.5$ GHz; near the highest MSBVW frequency for this H. It appears that the dispersion curve does not approach f_p at $k = 0$ but the theory does not completely describe the dispersion relation behavior for small wavevectors [23]. In Sec. 5.3.1 it is shown that the parameters used to calculate this dispersion relation accurately represent the spin waves studied in this chapter.

Magnons pumped at f_p (solid square) at sufficiently high microwave powers split into a pair of magnons that satisfy the conservation laws discussed earlier. Two possible magnon pairs that satisfy these laws are shown: the triangles and the circles. The shaded region represents possible energy states the pumping magnons can split into. Confluence magnons with frequency f_c represent a state formed by the recombination of two splitting magnons that have frequencies below $f_p/2$. These magnons are shown as an open triangle and an open
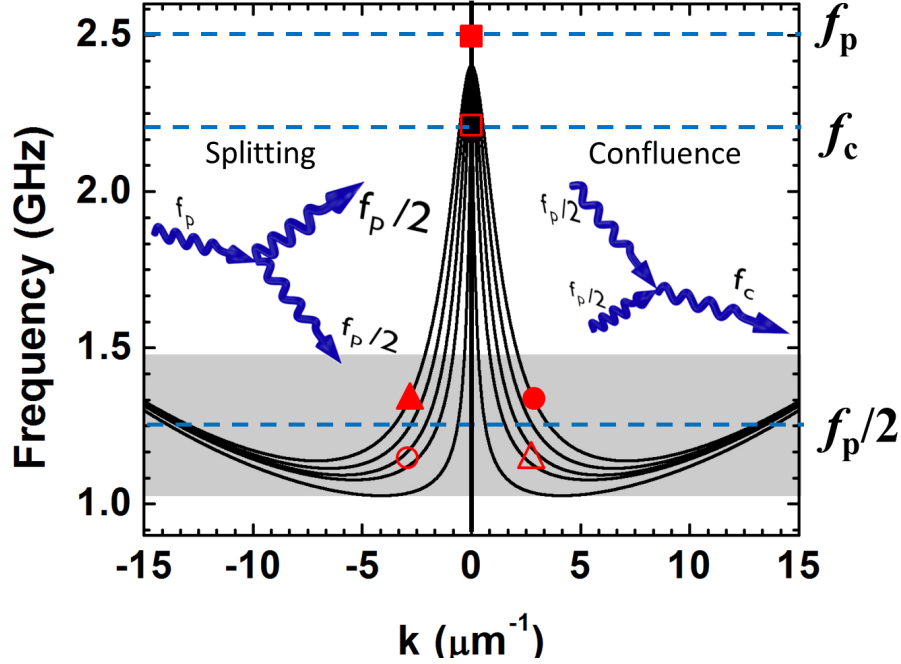
FIGURE 5.1. Calculated dispersion relation for YIG in the MSBVW configuration. The calculation were done using $H = 337$ Oe, $\gamma/2\pi = 2.8$ MHz/Oe, $4\pi M_s = 1830$ G, $t = 11.6$ μm, and $\alpha = 3\times10^{-12}$ cm^2. Also illustrated are the splitting and confluence processes.

circle. In the case of a purely MSBVW dispersion relation, the splitting magnons above $f_p/2$ (solid triangle and solid circle) have no possible states above f_p to recombine into. It can been seen in Fig. 5.1 that the splitting magnons are not restricted to low wavevectors as the pumping and confluence magnons are. Because of the shape of the dispersion curve, the group velocities $v_g = d\omega/dk$ for splitting magnons are slower than f_p and f_c magnons.

5.2. EXPERIMENTAL SETUP

The BLS measurements were performed in the MSBVW configuration. In this configuration, H is applied parallel to the spin wave propagation direction. One-dimensional time-resolved BLS measurements were performed to study the three magnon splitting and confluence processes in YIG. The time-resolved measurements provide direct temporal information

of these nonlinear magnons. These data, coupled with the one-dimensional scans, allow for group velocities to be extracted and compared with calculated dispersion relations. The experimental setup is constructed in the conventional forward scattering geometry (Chap. 3) with time-resolved BLS. The mirror spacing of the TFP used for measurements presented in this chapter was 15 mm. This corresponded to a free spectral range of 10 GHz, which was more than enough to allow for observation of magnons at f_p, $f_p/2$, and f_c, which will be $\leq$ 2.5 GHz.

Figure 5.2 shows a schematic of the YIG sample and scattering geometry used. The YIG film used in this study had a thickness t of 11.5 μm. Determination of this thickness is discussed in Sec. 5.3.1. The film had a length of 37 mm and a width w of 2.2 mm. The film was placed on top of a transducer antenna with a width $d = 50$ μm, where pulse-modulated microwaves were used to excite magnons at a pumping frequency f_p. Figure 5.3 shows the microwave components used in the setup. High and low microwave power-dependent measurements are discussed in Sec. 5.3.2. Unless stated otherwise, the measurements for this chapter were done at a high microwave power of 575 mW and a pumping frequency of $f_p = 2.5$ GHz.

A pulse width of 5 μs was chosen to ensure enough energy was going into the nonlinear processes so that $f_p/2$ and f_c could be excited and reach a steady-state population. To avoid possible heating effects, a large pulse spacing of 25 μs was chosen. This pulse spacing also ensured that the dynamics of the magnetic system were given enough time to relax before the onset of the following pulse. Measurements made with varied pulse widths are discussed in Sec. 5.3.2.

The same microwave pulses were used to synchronize the time-resolved setup of the experiment. The microwave pulse triggered the Fast ComTec P7887 time-of-flight analyzer
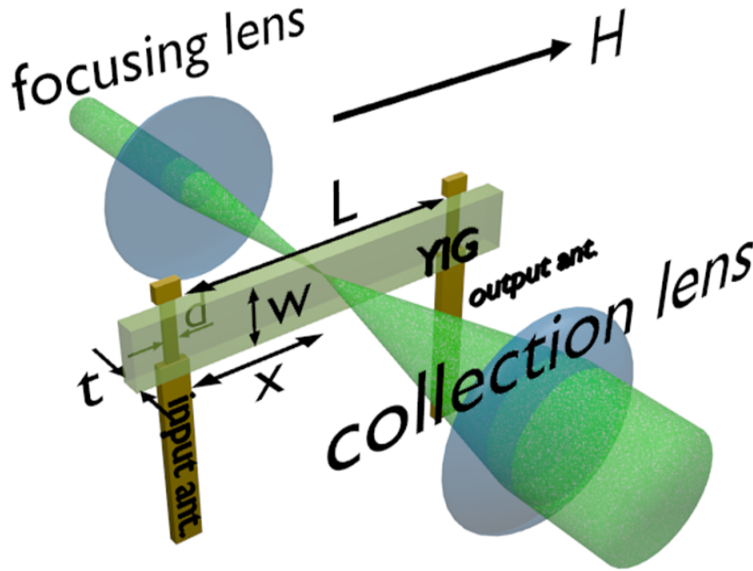
FIGURE 5.2. Schematic of the BLS forward scattering geometry. A lens is used to focus the incident light onto the YIG surface and another lens is used to collected the scattered light that is transmitted through the YIG. The external magnetic field H is applied along the long axis of the YIG film. The distance of the probing laser from the input antenna x was varied to obtain one-dimensional scans. The scattered light is collimated and directed to the TFP for analysis.
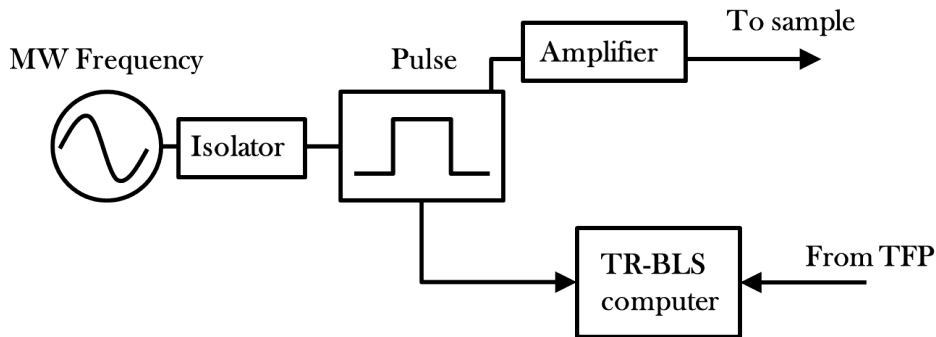
FIGURE 5.3. Schematic of the microwave components used to excite spin waves in the time-resolved BLS setup. A frequency generator was set to 2.5 GHz and gated by a pulse generator. The pulsed microwaves were then amplified. The pulses triggered the timer in the TR-BLS computer. An isolator is placed between the frequency and pulse generators to stop back-reflections from going back into the frequency generator and affecting the output power of the microwaves.

to start its timer. Once a photon was detected by the photodetector in the TFP, a signal

was sent to the time-of-flight analyzer to stop its timer. This time difference corresponds

to the time-of-flight of incident photons that have inelastically scattered from the YIG film. The time-of-flight analyzer allowed for clocking of the magnon arrival times with a resolution of up to 250 ps. For these measurements, a time resolution of 2 ns was used. This time resolution was more than sufficient to resolve the arrival times between magnons.

The spatial part of the experiment was set up so that one-dimensional scans were performed along the long axis of the YIG strip and perpendicular to the input antenna, as shown in Fig. 5.2. To conduct the scans, a Newport TRA25CC motorized actuator was used to vary the distance x of the probing laser from the input antenna. The copper block on which the antenna was mounted combined with the solid angle formed by the scattered light constrained x to a minimum value of 2.75 mm. A total scan range of 2.75 mm to 4.00 mm in steps of 0.125 mm was used.

5.3. Experimental Results

5.3.1. Network Analyzer Measurements. In the nonlinear three magnon splitting process, H and t play critical roles in determining whether or not these processes will occur. For these measurements, the wavevector of f_p is $k \approx 0$. The wavevector is actually finite but it is much smaller than that of $f_p/2$ that it can be approximated as zero. The upper limit of k that can be efficiently excited by the antenna is known as the wavevector cutoff,

$$k_{cutoff} = \frac{\pi}{d},$$

(5.1)

where d is the width of the antenna. For these measurements, $k_{cutoff} = 0.06~\mu\text{m}^{-1}$, which is close enough to zero that f_p lies near the ferromagnetic resonance (FMR) frequency for this film. When H is increased, the dispersion relation curve will shift vertically in frequency so that the frequency increases for all k. The shape of the curve including the difference between

f_{max} and f_{min} changes little with H. Consequently, f_p can be increased to a frequency where $f_p/2$ lies below the dispersion curve. In this case, the f_p magnons have no possible energy states to split into and the three magnon splitting process would not be observed. To ensure that the splitting process exist for these measurements, t was determined for this YIG film and then H and f_p were chosen to be sufficiently low that the dispersion relation allowed for $f_p/2$ magnons.

The pumping frequency $f_p = 2.5$ GHz was chosen to match a previous study of the splitting and confluence processes [101]. To chose appropriate values of H and to determine t, an Agilent E8361A General Purpose Network Analyzer (PNA) was used to measure the transmission loss, or S$_{21}$, and the change in phase of the spin waves being transmitted through the film as a function of frequency in the microwave regime. In this configuration, an output antenna was placed opposite to the input antenna, shown in Fig. 5.2, at a distance $L = 6.0$ mm. S$_{21}$ compares the signals sent to the input antenna with that received at the output antenna.

Figure 5.4 shows extracted PNA data. (a) shows the transmission loss as a function of frequency for $H = 337$ Oe. The onset of the curve above noise at higher frequencies occurs at the FMR frequency. The profile of the curve tails off at lower frequencies, which is consistent with the dispersion relation for MSBVW spin waves. The onset of the transmission loss profiles as a function of H is shown in (b). The blue line is a linear fit to guide the eye. The external magnetic field of 337 Oe was chosen such that $f_p = 2.5$ GHz corresponds to the maximum of the MSBVW dispersion relation.

The phase change of the transmission loss was collected to determine the thickness of the YIG film. For these measurements, the YIG film was placed in the MSSW configuration. This configuration was used in order to compare thickness values determined from other
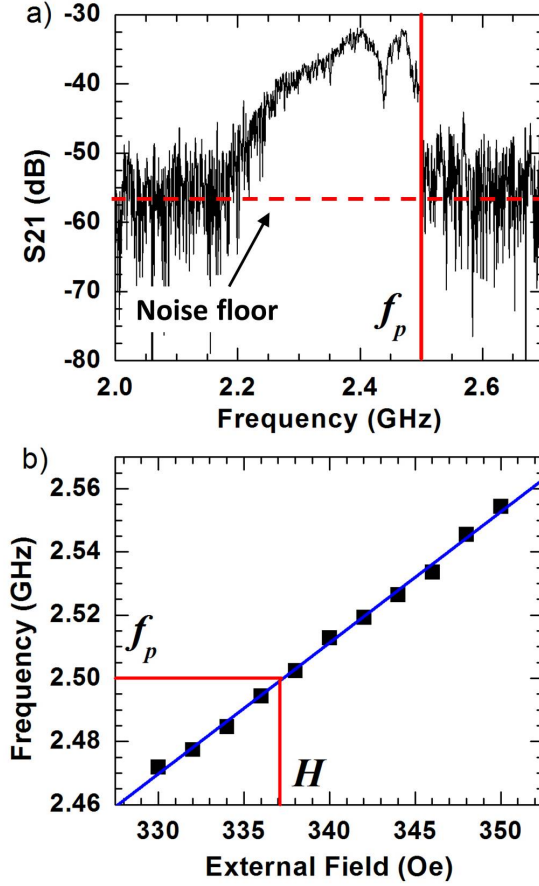
FIGURE 5.4. a) Transmission loss and b) extracted frequency of the onset of the curve versus H. a) shows the transmission loss profile in the MSBVW configuration for the YIG film used in this experiment at $H = 337$ Oe. The red dashed line is the noise floor. The frequency of the 10% rise of the transmission loss curve as a function of field is plotted in b). The blue line is a linear fit used to guide the eye. The value of $H = 337$ Oe was determined by the chosen f_p of 2.5 GHz.

sources [104]. In order to determine the film thickness, the unwrapped phase must be converted into the spin wave wavevector using

$$k = \frac{\phi}{L}, \tag{5.2}$$

where ϕ is the phase measured by the PNA and L is the separation between the input and output antenna. Once the PNA information is successfully translated into wavevector versus frequency, the dispersion relation (Eq. 2.16) can be used to fit for the film thickness.

Figure 5.5 shows the MSSW dispersion relation measured at two different external magnetic field values of $H = 337$ and 1000 Oe. Two curves are shown for each external magnetic field value because the sample had YIG on both sides of a substrate that was approximately 1 mm thick. The noise at the high frequency end of the curves represent phase changes due to the wires and can be neglected in the fit. It is observed that curves from both sides of the film lie on top of one another, confirming that they have the same thickness. To reduce the correlation between $4\pi M_s$ and t, the FMR frequency values ($k = 0$) were fitted with Kittel's equation (Eq. 2.7) with $\gamma/2\pi = 2.8$ MHz/Oe to determine $4\pi M_s$. Note that Eq. 2.7 does not depend of film thickness. This fit gave a $4\pi M_s$ of 1830 $\pm$ 20 G. A nonlinear least squares fit was performed on the curves using t as a shared fitting parameter. This fit is shown as the blue lines in Fig. 5.5 and gave a t of 11.6 $\pm$ 0.1 μm.
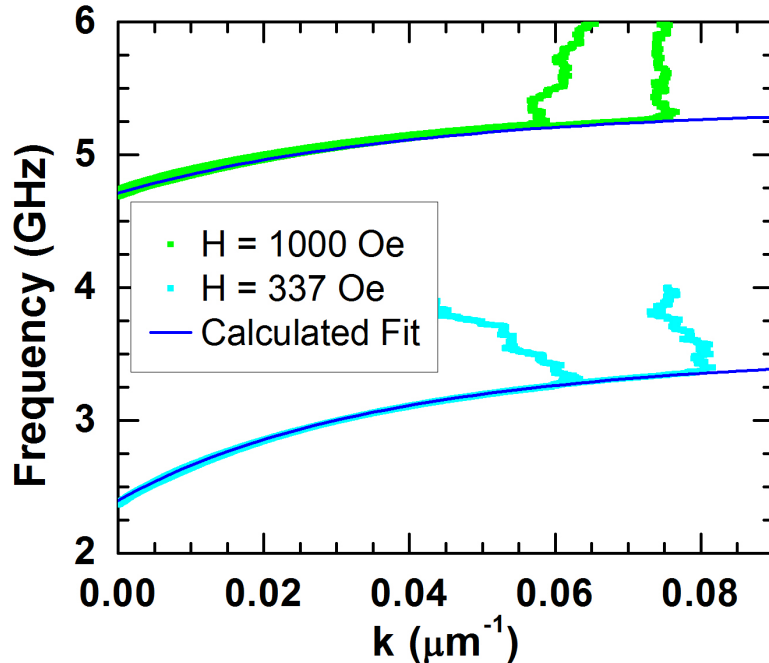
FIGURE 5.5. Extracted dispersion relation curves from the PNA. The two curves for each external magnetic field value represents the two surfaces of the film. The solid lines are fits using Eq. 2.7 with $4\pi M_s$ as a fitting parameter. The value of γ used was $\gamma/2\pi = 2.8$ MHz/Oe.

5.3.2. POWER- AND PULSE WIDTH-DEPENDENT MEASUREMENTS. The correct field and frequency combination discussed in Sec. 5.3.1 allows for the possibility for the three magnon splitting and confluence processes to occur. The other critical parameter is the microwave power used to excite f_p magnons. There exist a power threshold in which the relationship between the magnons generated at f_p is no longer linear in the excitation power. In this event, the increase of microwave power will go into populating nonlinear magnons, namely $f_p/2$ and f_c magnons. A microwave amplifier of 50 dB was used to ensure that the measurements were conducted in the nonlinear regime. Confirmation that the measurements were done in the nonlinear regime can be seen in Fig. 5.6 and Fig. 5.7.
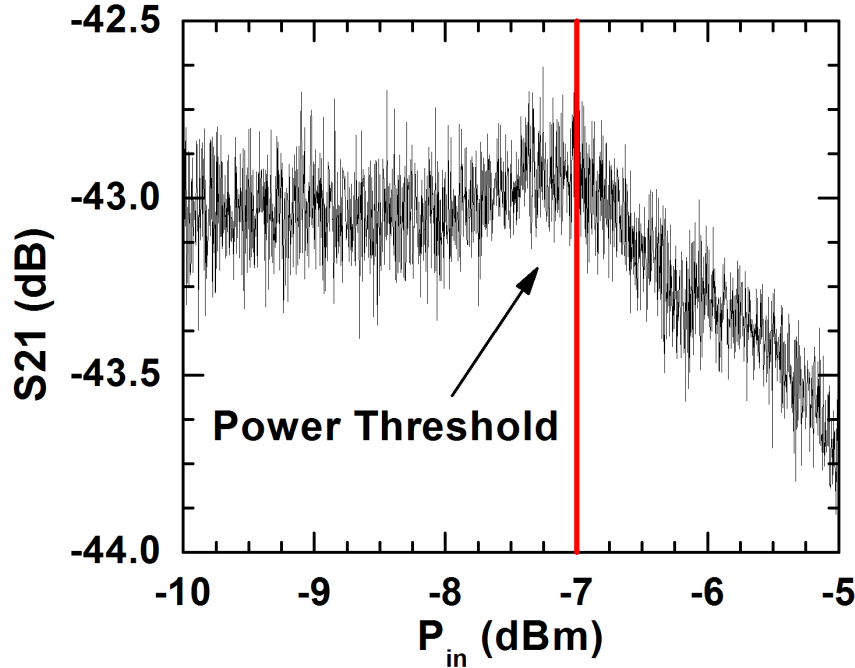
FIGURE 5.6. Transmission loss versus input microwave power. The nonlinear power threshold is observed at -7 dBm or 200 μW. The external magnetic field and the pumping frequency was $H = 337$ Oe and $f_p = 2.5$ GHz, respectively.

Figure 5.6 shows the PNA measurements for S_{21} as a function of input power for $H = 337$ Oe and $f_p = 2.5$ GHz. For input powers below -7 dBm, the transmission loss is constant

57
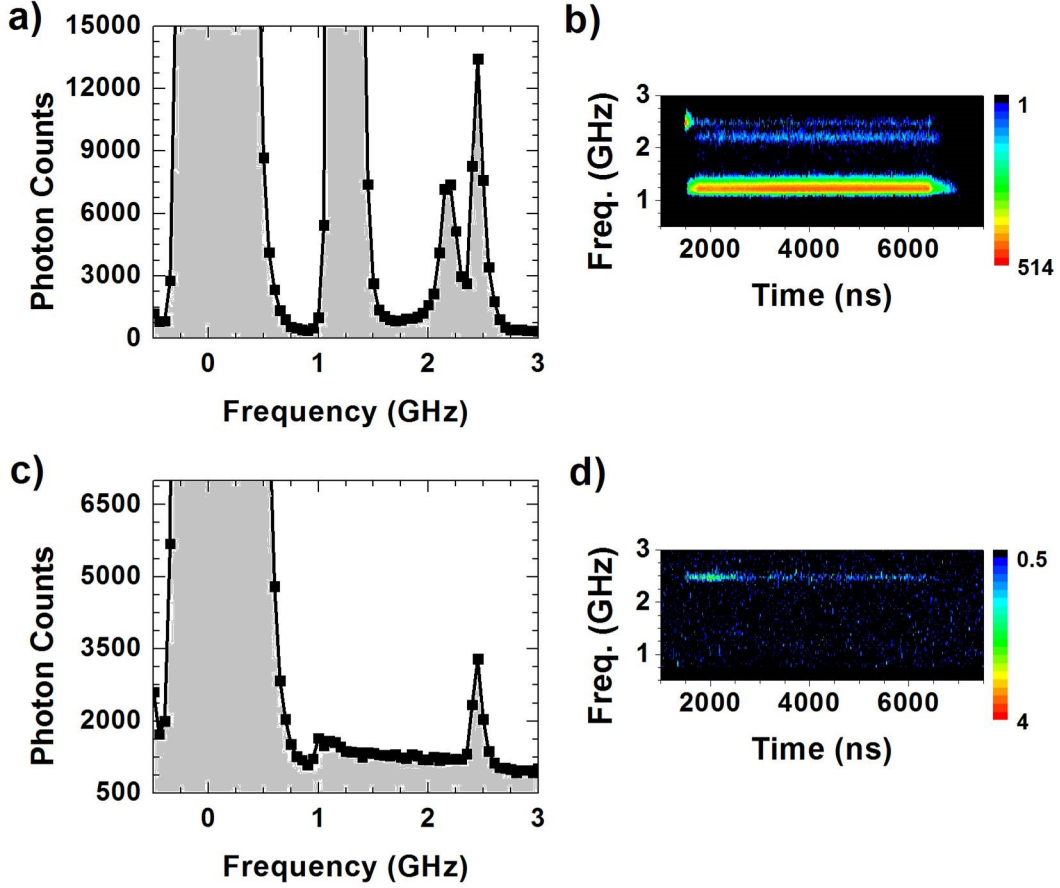
FIGURE 5.7. High and low power BLS spectra and their respective time-resolved spectra. The high power spectra are shown in a) and b) while the low power spectra are shown in c) and d). These spectra were measured at x = 2.75 mm and in an external magnetic field H = 337 Oe. The high and low power measurements were performed with microwave powers of 575 mW and 260 μW, respectively. f_p is at 2.5 GHz, $f_p/2$ is at 1.25 GHz and f_c is at 2.2 GHz.

around -43 dBm. This region corresponds to the linear excitation of magnons with frequency f_p. As the input power is linearly increased the transmitted output power increases linearly, as well. Once the input power exceeds -7 dBm, the transmission loss is no longer constant. The power threshold is at -7 dBm or 200 μW. This power threshold is comparable to the reported power threshold in Ref. [103]. When the input power passes this threshold, the transmitted output power no longer increases linearly with respect to the input power. This loss in power at f_p goes into exciting $f_p/2$ and f_c magnons.

Figure 5.7 shows the high and low power BLS spectra for $f_p = 2.5$ GHz. (a) and (c) are the BLS spectra, while (b) and (d) are their respective time-resolved spectra. The high power spectra (a) and (b) were performed with a microwave power of 575 mW and the low power spectra (c) and (d) were performed with a microwave power of 260 μW. These powers were measured with a Agilent E4419B power meter. The power was measured after all the microwave components and represents the power at the input antenna. The high power spectra show three distinct peaks at $f_p = 2.5$ GHz, $f_p/2 = 1.25$ GHz, and $f_c = 2.2$ GHz. In contrast, the low power measurements show only one peak at f_p. Both time-resolved spectra (b) and (d) show arrival times of magnons at f_p, but (b) shows the arrival times of additional magnons with frequency $f_p/2$, and f_c. It should be noted that the distance from the antenna remained constant at $x = 2.75$ mm. This means that the difference in intensities between the high and low power measurements is mainly due to the microwave power itself rather than the additional decay of propagating magnons due to damping.

Besides the appearance of $f_p/2$ and f_c magnons in the high power measurements, the peak corresponding to f_p is shorter in time than the low power measurements. The f_p signal was integrated over a frequency range of 2.3-2.7 GHz. The integrated signal is shown in Fig. 5.8. The signal starts around 1500 ns and ends around 6500 ns for a pulse width of 5 μs. The high power signal shows a sharp and intense peak at the beginning of the signal, while this is absent in the low power signal. The low power signal does show a less pronounced "hump" at its onset because it is still in the nonlinear power regime but is not efficiently exciting splitting magnons. Its maximum intensity compared to the signal background of the pulse width is significantly lower than that of the high power signal. The signal background is shown is Fig. 5.8 as the dotted line and is referred to as the detectable signal that is

59

relatively flat and contained within the pulse width. The signal background of the pulse width is seen as magnons that are not contributing to $f_p/2$ and f_c magnons.
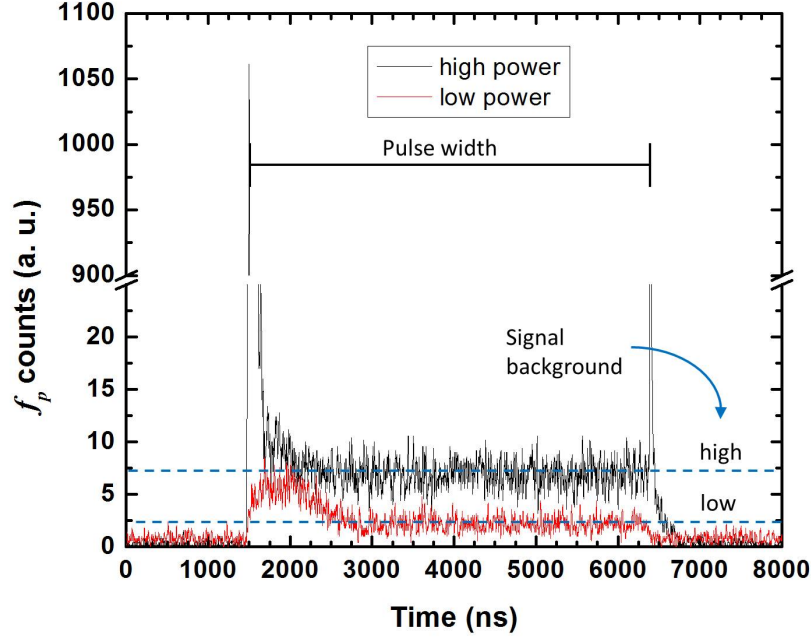
FIGURE 5.8. Integrated high and low power f_p counts for a frequency range of 2.3-2.7 GHz measured by time-resolved BLS. The high and low powers were 575 mW and 260 μW, respectively. The signal background is denoted as the signal that is above noise which corresponds to f_p magnons that are not converting into $f_p/2$ magnons.

One would expect that in the absence of nonlinear magnons (lower powers), the signal would be more square-like. The fact that this is not the case as the power is increased means that the energy difference contained in a square-like signal compared to those in Fig. 5.8 must contribute to the excitation of nonlinear magnons. This is known as pulse narrowing [103] and is widely observed for nonlinear process. The sharp and intense peak at the end of the high power signal can be explained by the fact that the directly pumped magnon populations are lower at the beginning and the end of the pulse and the system is temporarily below the threshold for the splitting process. The $f_p/2$ and f_c magnons, in

contrast, show a relatively constant spectra for the full 5 μs, which will be discussed in more detail later in this chapter.

The microwave pulse parameters are also an important consideration for the excitation of nonlinear magnons. Figure 5.9 shows BLS spectra obtained with pulse widths of 1, 2, 3 μs, and infinity (CW). The parameters that remained constant throughout these measurements were the external magnetic field $H = 350$ Oe, the generator output power of $P = 18$ dBm and the pulse rate of 4 μs. Considering just the Stokes side of the spectra, at shorter pulse rate (a) the $f_p/2$ magnons are comparable in intensity to the f_p magnons. As the pulse width is increased (b)-(c) the $f_p/2$ peak starts to grow noticeably larger than the f_p peak and the formation of f_c starts to become apparent. The CW measurement shows that the f_p peak is suppressed and only the $f_p/2$ peak can be seen. On the rise and fall of the pulse, f_p magnon are excited and propagate without conversion to $f_p/2$ magnons because the power drops below threshold.

5.3.3. ONE-DIMENSIONAL SCAN. In order to determine the group velocities of f_p, $f_p/2$, and f_c magnons, one-dimensional spatial scan were performed. Figure 5.10(a) and (b) are the same as in Fig. 5.7. They are shown mainly for comparison with (c) and (d). The comparison of the two is at the closest (a)-(b) and furthest distance (c)-(d) from the antenna. These distances are $x = 2.75$ mm and $x = 4.00$ mm. Figure 5.10 shows that at $x = 4.00$ mm magnons are still being detected meaning that the loss in microwave power due to damping is not significant enough to lower the power below the detection threshold. Time-resolved BLS spectra were collected for intervals of 0.125 mm between these two points.

Figure 5.11 shows the integrated arrival times for f_p, $f_p/2$, and f_c magnons. The time-resolved spectra in Fig. 5.10 as well as those recorded at other distances were integrated for each arrival time within frequency ranges that correspond to f_p, $f_p/2$, and f_c. These ranges
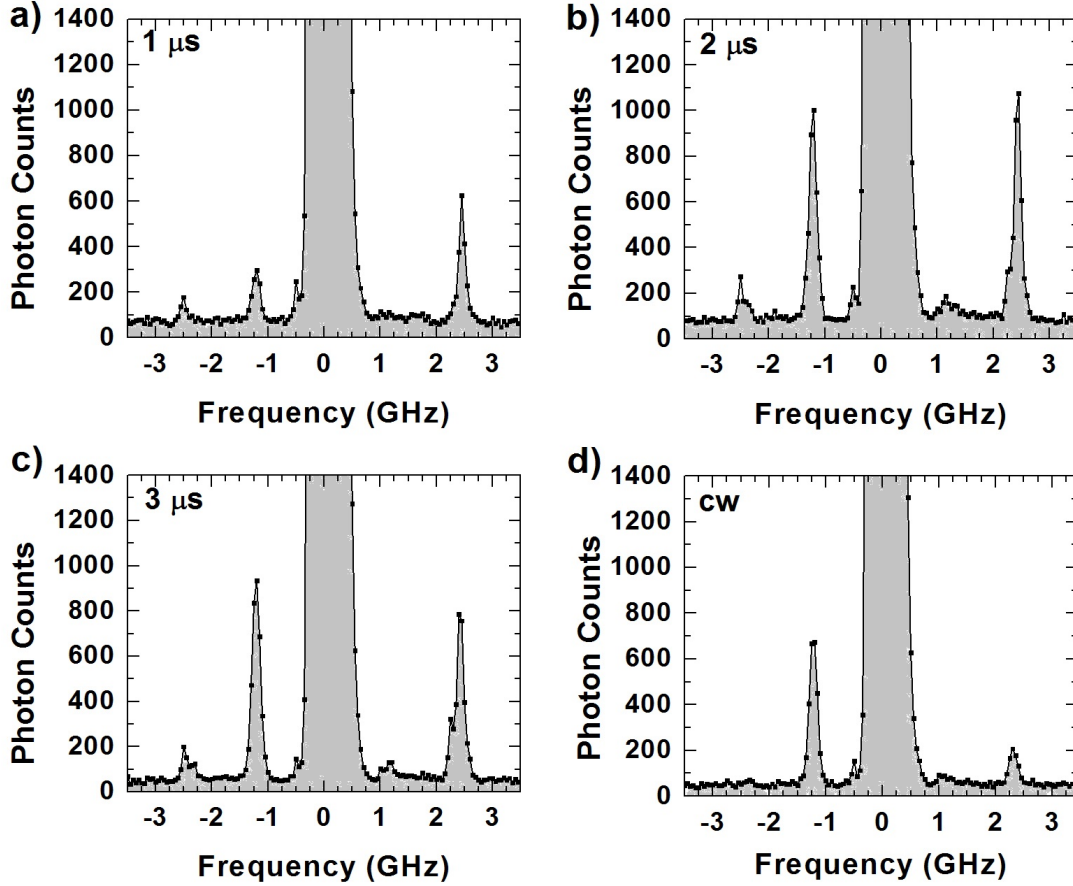
FIGURE 5.9. Pulse width-dependent measurements for pulse widths of a) 1 μs, b) 2 μs, c) 3 μs, and CW. These measurements were performed at a $H = 350$ Oe, $f_p = 2.5$ GHz, generator output power of $P = 18$ dBm, and a pulse rate of 4 μs.

are given in the figure caption. The intensities have been scaled and a vertical shift that was proportional to x was added so that they can be compared on the same plot. The scaling was necessary because spin wave signals further away from the antenna were low. The scaling was done by normalizing the data to a baseline that was taken as the signal background. The two dotted red vertical lines represent the pulse width, 5 μs, of the microwave pulse where the start of the pulse was chosen such that it coincides with the start of the f_p signal at $x = 2.75$ mm. These lines are there to illustrate the pulse length and to show that there is a time delay between the first arrival times of $f_p/2$ magnons as compared to the f_p magnons
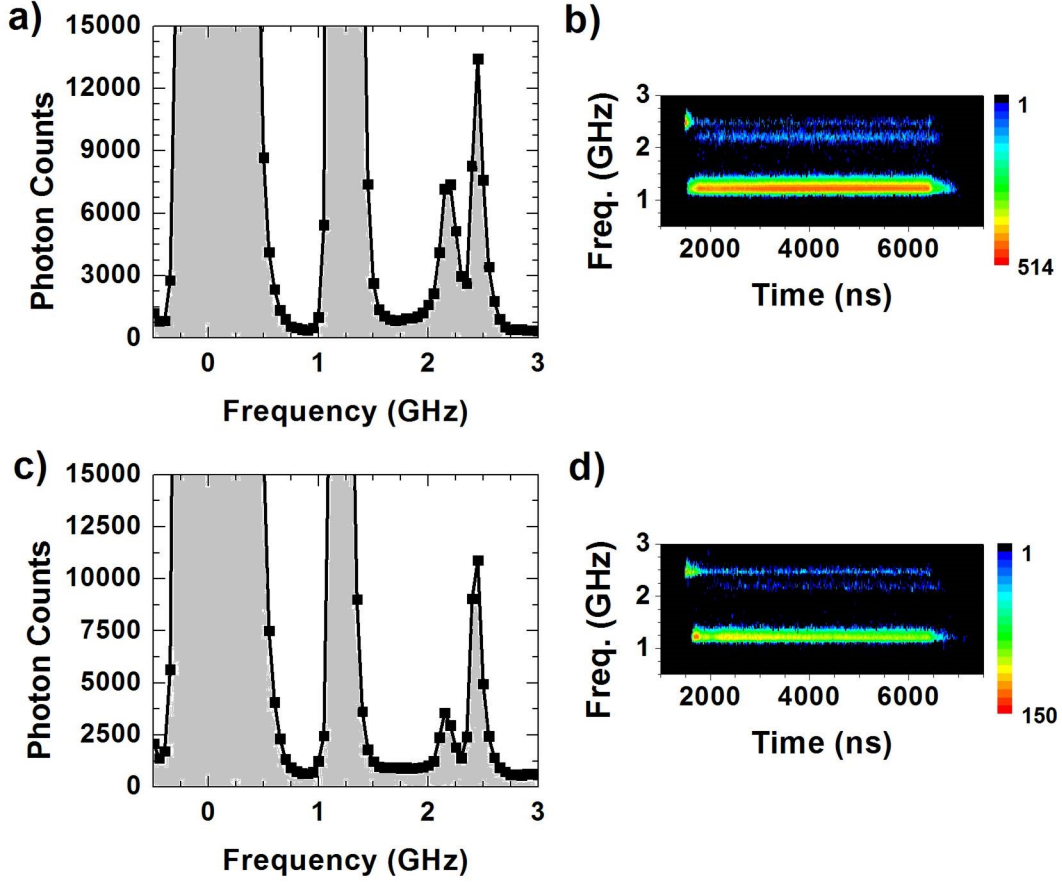
FIGURE 5.10. Selected raw BLS and time-resolved spectra. a) and b) are spectra for $x = 2.75$ mm while c) and d) are spectra for $x = 4.00$ mm. These measurements were performed at a $H = 337$ Oe, $f_p = 2.5$ GHz, microwave power of 575 mW, a pulse duration of 5 μs, and a pulse rate of 25 μs.

and the first arrival times of the f_c magnons as compared to the $f_p/2$ magnons. The initial peak in (c) is due to the spread in frequencies of the f_p magnons. This spread can be seen in Fig. 5.10(b).

The f_p signal (a) broadens as x increases and a second peak starts to form. This secondary peak corresponds to magnons that are traveling at a slower velocity because of their later arrival times compared to the initial peak. The $f_p/2$ signal (b) arrives later in time than the f_p signal, which suggest that the $f_p/2$ magnons are traveling slower than the f_p magnons. This is expected based on the slopes of the dispersion relation curve corresponding to f_p and
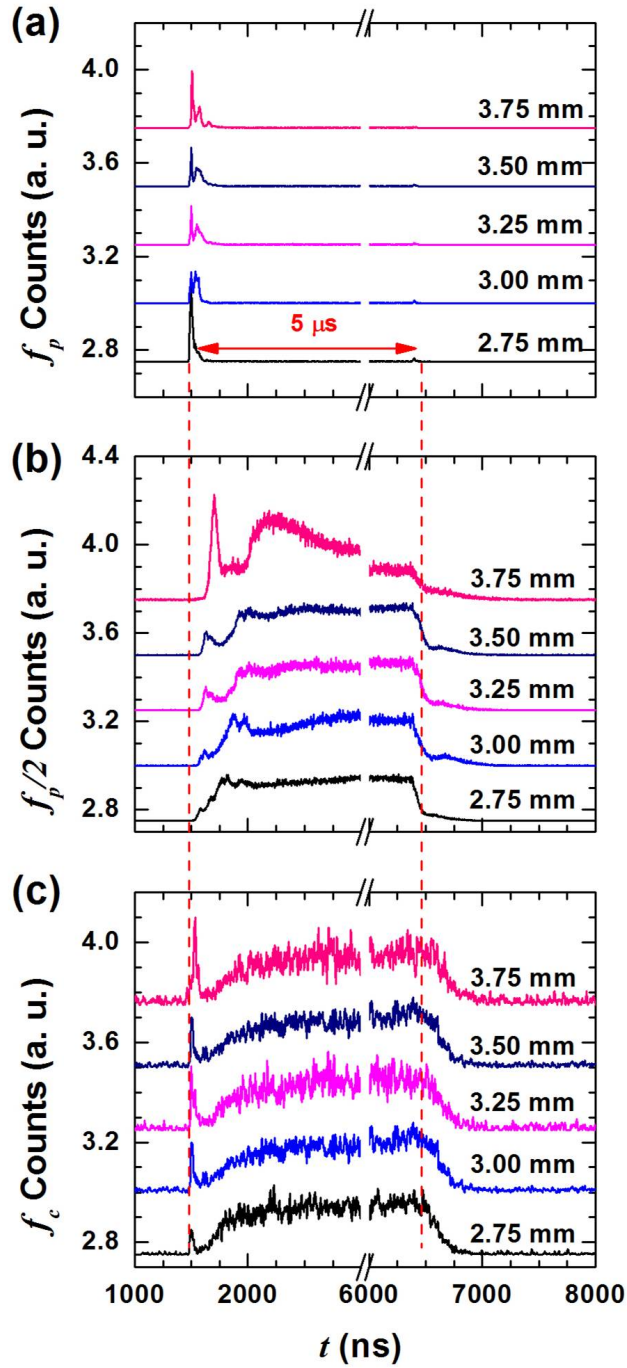
FIGURE 5.11. Extracted time-resolved signals for specific frequency ranges corresponding to a) f_p, b) $f_p/2$, and c) f_c. The frequency ranges for f_p, $f_p/2$, and f_c were 2.3-2.7 GHz, 1.0-1.5 GHz, and 2.1-2.3 GHz, respectively. These measurements were performed at a $H = 337$ Oe, $f_p = 2.5$ GHz, microwave power of 575 mW, a pulse duration of 5 μs, and a pulse rate of 25 μs

$f_p/2$. As x increases a secondary peak is seen to form in the $f_p/2$ signal. These secondary peak are consistent with the peaks observed in Ref. [103].

5.4. Discussion

Given the temporal and spatial information from the one-dimensional scans, one can extract the group velocities of the magnons with a simple linear fit of the position as a function of the magnon arrival time. Calculated group velocities can be determined directly from the derivative of the dispersion relation (Eq. 2.10) with respect to the wavevector k: $v_g = d\omega/dk$.

The arrival times of the integrated time-resolved signals from Fig. 5.11 for the 10, 50, and 90 percent of the rise time were extracted and plotted in Fig. 5.12. The arrival times for the two peaks in Fig. 5.11 for f_p and $f_p/2$ magnons are also plotted. A linear least squares fit was performed to determine the group velocities from the different magnon arrival times, which are shown as the blue solid lines. Note that the position is on the x-axis and the time on the y-axis in these plots.

The arrival times of the two peaks for each of the f_p and $f_p/2$ magnons were determined by eye using a plotting program. The uncertainties in times associated with these peaks were taken from the time resolution used in the experiment of 2 ns. The high signal-to-noise in the f_p and $f_p/2$ signals allows for straightforward extrapolation of 10, 50, and 90 percent of the rise time. The uncertainty associated with these values was taken as 2 ns. In contrast, the low signal-to-noise in the f_c signal made it difficult to estimate the risetimes directly so a fitting routine was used to determine suitable rise time values. A cumulative Gaussian distribution was used because it provides a reasonable representation of the signal shape. To determine the uncertainties in the f_c signal, two lines were drawn from the minimum to the
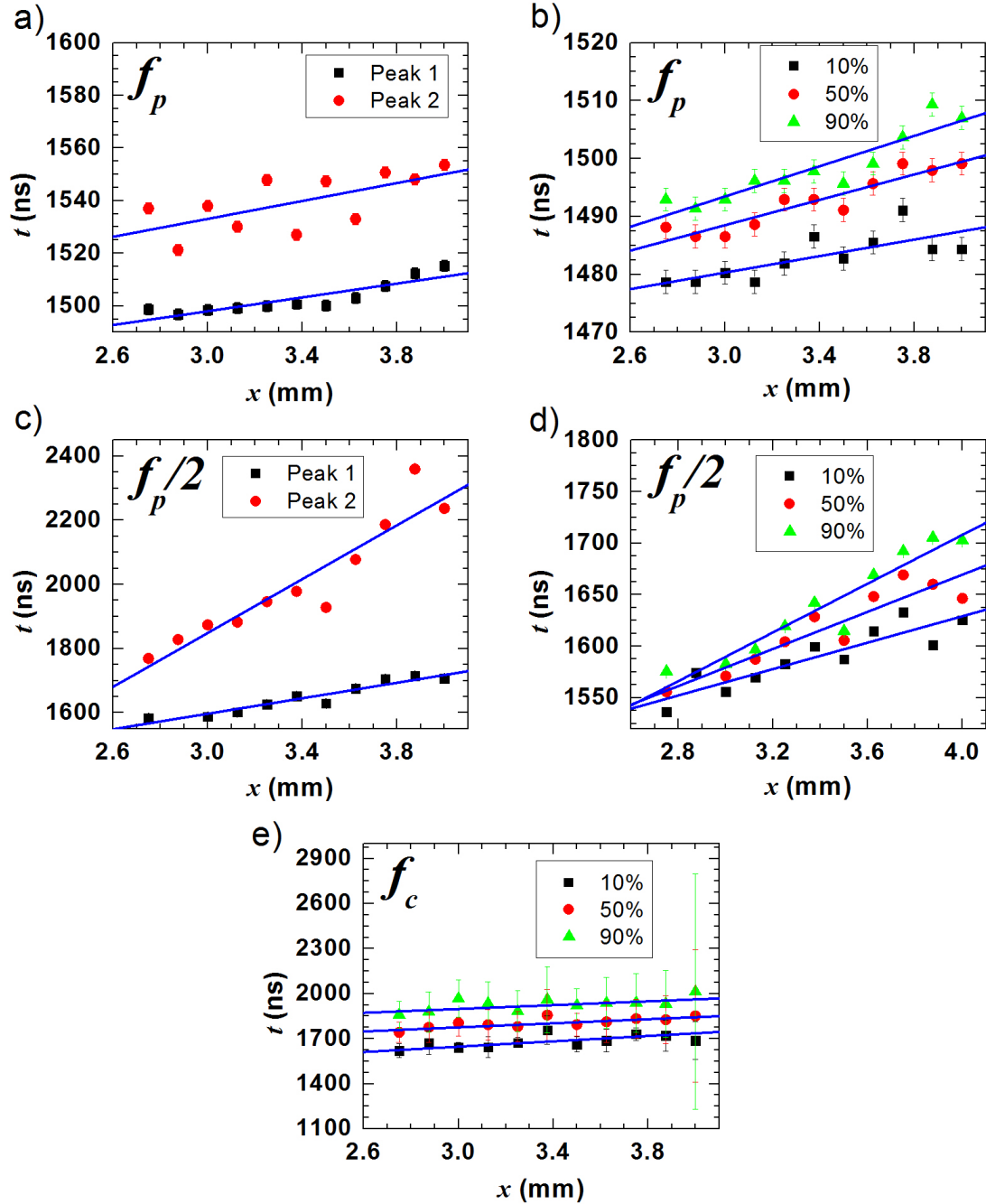
FIGURE 5.12. a)-e) Arrive times taken from Fig. 5.11. a) and c) are the arrival times for the peaks in f_p and $f_p/2$, respectively. b),d), and c) are the arrival times based on the 10, 50, and 90 percent of the rise. The (blue) solid line is a linear fit that was used to extract the group velocities of those magnons.

maximum values of the signal. The separation of these two lines were set to encompass all the noise in the risetimes. The uncertainties for the percentage of the risetime was taken as the separation of these lines (in time) at their respective values of 10, 50, and 90 percent. For all of these measurements, the uncertainty in position was due to the systematic uncertainty in the translation actuator and is taken as 10 μm.

The arrival time data as a function of position were fitted using a straight line linear least squares fit and the slope, intercept, and group velocities are tabulated in Table 5.1. The slope and the intercept were parameters used in the linear least squares fit. Their associated uncertainties were fitting uncertainties of the parameters. The slope and intercept both have physical meaning; the group velocity is obtained from the inverse of the slope of the magnons and the intercept represents the time of flight of a photon after interacting with a magnon plus any delay time from formation processes or time spent as another magnon. The uncertainties in the table are the uncertainties in the fit parameters and in the case of v_g, the uncertainty was calculated from these uncertainties.

TABLE 5.1. Fitted magnon group velocities.

Magnon Type	Risetime Position	Slope (ns/mm)	Intercept (s)	v_g (μm/ns)
f_p	peak 1	13 ± 2	1459 ± 5	76 ± 13
	peak 2	17 ± 2	1482 ± 5	59 ± 23
	10%	7 ± 2	1459 ± 5	140 ± 40
	50%	11 ± 2	1456 ± 5	91 ± 11
	90%	13 ± 2	1454 ± 5	76 ± 11
$f_p/2$	peak 1	121 ± 2	1234 ± 6	8 ± 1
	peak 2	421 ± 2	588 ± 5	2 ± 1
	10%	64 ± 2	1373 ± 5	16 ± 3
	50%	90 ± 2	1309 ± 6	11 ± 2
	90%	118 ± 2	1235 ± 6	8 ± 1
f_c	10%	89 ± 46	1380 ± 151	11 ± 6
	50%	68 ± 89	1572 ± 284	15 ± 19
	90%	64 ± 123	1706 ± 391	16 ± 30

Figure 5.13 shows selected data from Fig 5.12 replotted. The arrival times of the f_p peak and the 10 percent of the $f_p/2$ rise are shown in (a). Similarly, (b) shows the arrival times of the $f_p/2$ peak and the 10 percent of the f_c rise. The insets are there to clarify where in the signal the data are taken from. These arrival times are chosen because the peaks show where the population of the respective magnons are at a maximum before the onset of the nonlinear splitting process, and the 10 percent of the rise represents the onset of the newly generated population of magnons above noise.

To better understand these nonlinear processes, one must consider the sequence of events for these processes. First, f_p magnons are pumped by the antenna, then they split into $f_p/2$ magnons and then some fraction of the $f_p/2$ magnons will recombine to form f_c magnons. Keeping this mind, the intercept from Table 5.1 would suggest that the $f_p/2$ magnons form before the f_p magnons if they were formed at the antenna ($x = 0$). Since this is not the case based on the sequence of events, the $f_p/2$ magnons must form at a distance x_0 away from the antenna. The pulse narrowing of the f_p signal means that after a short period of time, approximately the peak width, the majority of the f_p magnons split into $f_p/2$ magnons. This would suggest that the FWHM of the f_p peak would indicate the time required to achieve a sufficient f_p populations to initiate the splitting into $f_p/2$ magnons. The FWHM value is approximately 30 ns. The position at which the two lines in Fig. 5.13(a) intersect provides a reasonable estimate for x_0. This position is calculated by setting the two linear fit equations equal to one another and solving for x_0. This yields a value of $x_0 = 1.7 \pm 0.2$ mm. This uncertainty is based on the uncertainties in the slope and intercept values in Table 5.1.

After the $f_p/2$ magnons have formed, some fraction will recombine to form the f_c magnons. Since the $f_p/2$ magnons travel more slowly than the f_c magnons, the f_c magnons will likely form in a region near x_0. If $f_p/2$ magnons are forming near x_0, this sets a lower
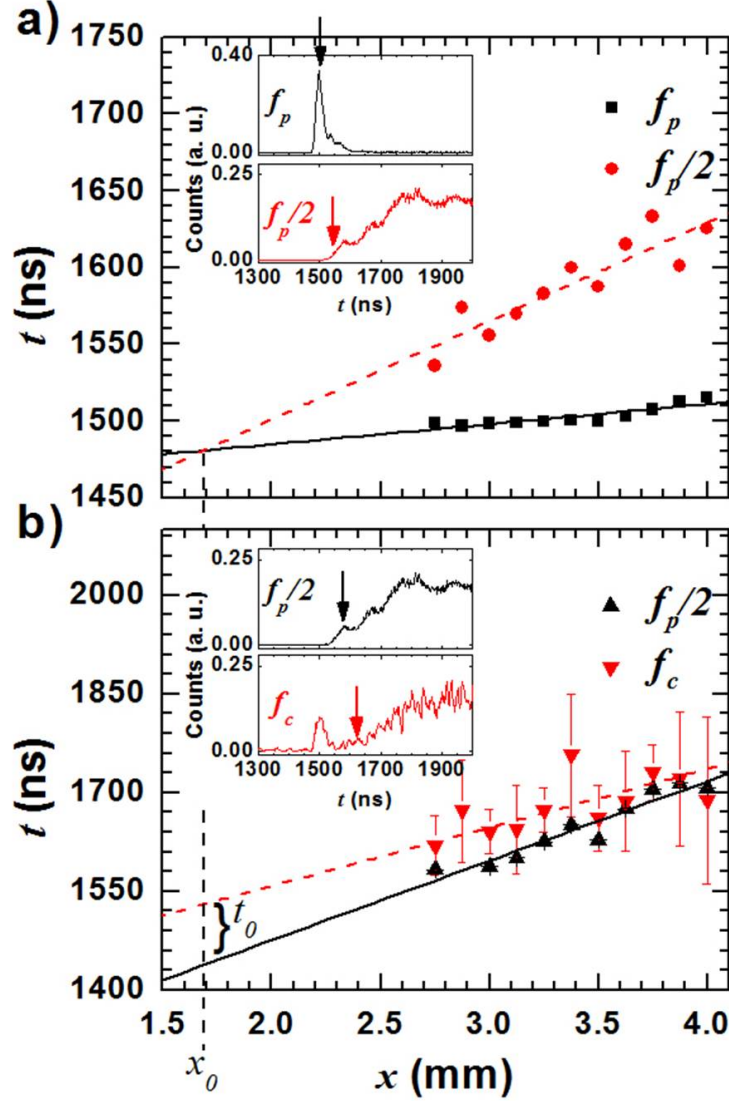
FIGURE 5.13. a) Arrival times as a function of x for f_p and $f_p/2$ magnons. The (black) squares represent the arrival times of the pumping magnons at their maximum population before converting into splitting magnons. The (red) circles represent the onset of the arrival times for the splitting magnons. The inset in a) is a scaled version of the data from Fig 5.11. b) Arrival times as a function of x for splitting and confluence magnons. b) is analogous to a) except now the splitting magnons take on the role of converting into confluence magnons. The time difference between the confluence and splitting magnons at x_0 is taken as the time for the conversion of splitting magnons into confluence magnons and is denoted as t_0.

limit for the distance from the antenna that the f_c magnons can form. In Fig. 5.13(b) the

lines do not intersect before the first measurement at $x = 2.75$ mm or the upper limit of

formation. The separation of the lines at a given position less than $x = 2.75$ mm and greater than x_0 may correspond to the time it takes for f_c magnons to form. With the current dataset, there are two parameters that describe the formation of f_c magnons: the formation time and position. The limited theory available in the literature [23] leads to the consideration of the simplest case; f_c magnons form at the same position that the $f_p/2$ magnons form, x_0. At this position the formation time can be calculated by subtracting the times from the two lines at x_0. This yields a value of $t_0 = 90 \pm 170$ ns. This can be interpreted as the approximate time that it takes for an $f_p/2$ magnon to find a suitable confluence pair. In this time, the $f_p/2$ magnons probably move 1.3 mm or less from x_0 so f_c magnons are expected to form at a distance less than approximately 3 mm.

5.5. Conclusions

This chapter provided experimental results on the nonlinear three magnon splitting and confluence processes. A detailed microwave measurement was conducted to better understand the microwave power requirements to operate in the nonlinear regime. The time- and space-resolved BLS measurements offered insight into the formation of these processes. By determining the group velocities of the magnons associated with each process, a simple extrapolation of the position away from the antenna that the splitting magnons form, x_0, and the time of formation of the confluence magnons, t_0. The value for x_0 appears reasonable for the setup of this experiment and can be tested by measuring whether or not $f_p/2$ magnons can be measured at values of $x < x_0$. Unfortunately, the setup used here is limited to a minimum value of $x = 2.75$ mm.

CHAPTER 6

Spin Dynamics in Confined Metallic Microstrips

6.1. Introduction

Micrometer-sized structures (microstructures) involving metallic magnetic materials are of interest both because the confinement leads to altered spin wave physics and due to the potential for technological applications. The spin wave physics becomes interesting when the dimensions of the microstructures are comparable to the spin wave wavelength, which is typically on the order of a few micrometers. The spin wave measurements discussed so far in this thesis have been for continuous thin films. In continuous thin films, the spin wave wavevectors are quantized along the thickness of the film but not along the plane parallel to the film surface. Microstructures introduce spin wave quantization or confinement along the film surface, which leads to modifications to the dispersion relations presented in Chap. 2. Some of the technological applications where magnetic microstructures are important include magnetic random access memory (MRAM) [105–108] and magnonic logic devices [109–112].

Microstructures come in various forms but the most commonly studied, also studied in this thesis, are microstrips [113–116]. Microstrips are useful in studying spin wave physics because the spin wave confinement parallel to the film surface is only along one direction. Previous studies on microstructures have investigated spin waves in Permalloy ($Ni_{80}Fe_{20}$) microstrips that varied in width from 1 to 5 μm. They observed spin wave edge modes [113], spin wave interference [114], spin wave phase fronts [115], and nonlinear effects [116] using micro-BLS. Although micro-BLS is not the only technique for studying spin waves in microstructures, it has its advantages over techniques like MOKE, the measure of the

polarization of scattered light, because it provides a means to directly observe the spin wave frequencies.

This chapter will present work on spin wave propagation in low anisotropy Permalloy and perpendicular anisotropy CoNi microstrips. The Permalloy microstrips were grown at Argonne National Laboratory by Helmut Schultheiβ and Katrin Vogt. Spin wave propagation in the Permalloy microstrips were experimentally observed with micro-BLS in the magnetostatic surface wave (MSSW), commonly known as the Damon-Eshbach (DE), configuration and the magnetostatic backward volume wave (MSBVW) configuration. The experimental observations were verified by proper modifications to the dispersion relations discussed in Chap. 2. The specific modifications will be outlined in the section that follows. The CoNi microstrips were grown at New York University by Ferran Macià and Andrew Kent. Measurements were conducted in an out-of-plane and in-plane external magnetic field. Note that to remain consistent with the terminology typically used in the literature, DE will be used instead of MSSW to denote surface spin waves and BV will be used instead of MSBVW to denote backward volume spin waves.

6.1.1. LATERAL CONFINEMENT. When discussing spin wave propagation in microstrips, there are four important terms all linked to demagnetization effects, that must be taken into consideration: (1) demagnetization field, (2) laterally quantized spin waves, (3) effective width, and (4) shape anisotropy. Although these terms are presented separately, it will be seen in this section that they are interrelated.

Term (1), the demagnetization field, arises from the dipolar field generated by the magnetic moments of the sample. Figure 6.1(a) illustrated the demagnetization field relative to the externally applied magnetic field $\mathbf{H}$ and the magnetization $\mathbf{M}$ of a sample with finite width. To easily understand the effect of the demagnetization field, consider a magnetically

soft alloy like Permalloy. In a sufficiently large externally applied magnetic field $\mathbf{H}$, the Zeeman field will dominate and $\mathbf{M}$ will point along $\mathbf{H}$ according to Eq. 2.1. The net dipolar field produced by $\mathbf{M}$ will point in the direction opposite to $\mathbf{H}$ in the center of the sample. This gives rise to an effective internal magnetic field that can be expressed as

$$H_{i,eff} = H_i - N_i M_i, \tag{6.1}$$

where i represents a Cartesian axis and N_i is a positive constant called the demagnetization factor along the i axis. It is clear from Eq. 6.1 that for nonzero demagnetization factors, $|H_{eff}|$ is less than $|H|$. $N_i M_i$ is the demagnetization field $H_{demag,i}$ and M_i is the component of $\mathbf{M}$ along the i direction and is at most the saturation magnetization M_s.
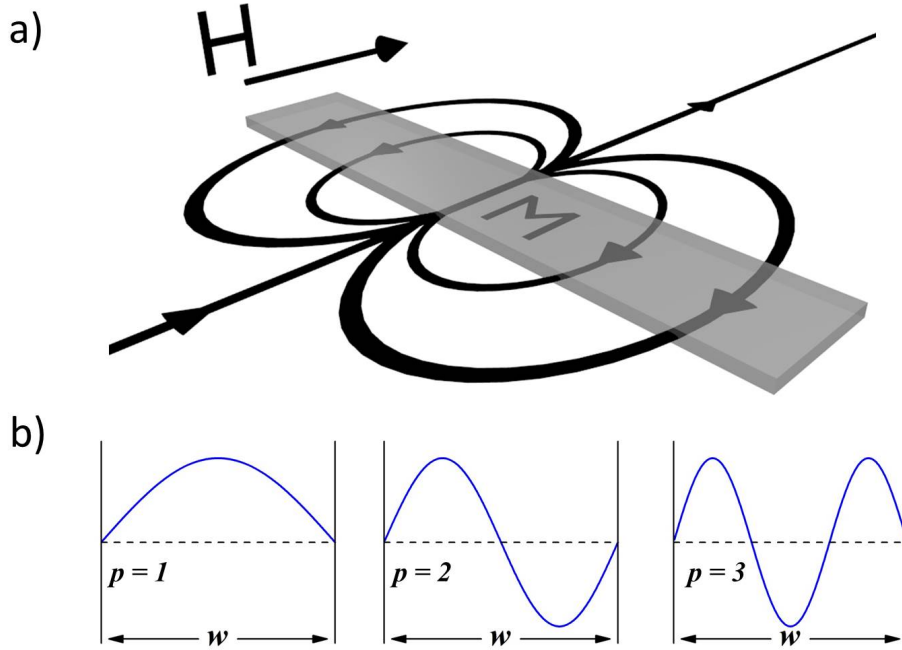
FIGURE 6.1. a) Illustration of the demagnetization field and b) spin wave mode profiles across the width of a microstrip. The demagnetization field reduces the total internal magnetic field giving rise to an effective magnetic field of $H_{eff} = H\text{-}H_{demag}$. The spin wave mode profiles in b) are shown with pinned spins on the lateral edges and the first three profiles across the sample width w are shown with mode index p.

The demagnetization factors for an infinite sheet and for a sphere are given in Ref. [1]. For an infinite sheet in the xy-plane, $N_x = N_y = 0$ and $N_z = 4\pi$. For a sphere, $N_x = N_y = N_z = 4\pi/3$. The demagnetization factors must, by convention, sum to 4π in CGS units. The demagnetization factors for a sphere are equal due to spherical symmetry, whereas, in an infinite sheet the demagnetization factors parallel to the plane are zero. Analytical expressions exist for demagnetization factors for a general ellipsoid [117, 118] but this is a poor approximation for microstrips with width w because of the difference in volume and geometry. A better approximation exist for $t \ll w$, which is the case with microstrips and is given as $N_y = 4\pi(2t/\pi w)$, $N_z = 4\pi$ - N_y, and $N_x = 0$ [119]. Here the long axis of the microstrip is taken along the x-axis the width is taken along the y-axis, and the normal of the film is taken along the z-axis. The values obtained using this approximation compare well to values obtained from micromagnetic simulations [120] performed by Ref. [91]. The values for H_{demag} for specific samples will be discussed in Sec. 6.2.5, where H_{eff} is used to calculate the spin wave dispersion relations.

Term (2), spin wave quantization, refers to the fact that spin waves will become quantized across the width of a microstrip when the spin wave wavelength is comparable to the size of the width. The comparable width and wavelength leads to lateral standing spin waves along the width of the microstrip. This is not to be confused with the perpendicular standing spin waves that are confined by the top and bottom surfaces of the film, which are much higher in frequency and have wavevectors $\kappa_n = n\pi/t$ because the film thicknesses studied here are typically on the order of tens of nanometers. The quantization of the wavevector described in Ref. [121] and [122] goes as

$$k_p = \frac{p\pi}{w},$$
(6.2)

where p is an integer multiple of the wavelength and w is the width of the microstrip. Now the total spin wave wavevector is modified from Eq. 2.12 to be

$$k_n^2 = k_x^2 + k_p^2 + \kappa_n^2.$$

(6.3)

Here $k_\parallel^2$ is taken as $k_x^2 + k_p^2$. k_x is the wavevector of the spin waves that propagate parallel to the long axis of the microstrip (x-axis). The description of k_p in Ref. [121] and [122] assumes pinned spins at the lateral edges of the microstrip. For pinned spins, $p = 1, 2, 3,$ $ldots$. As will be discussed with term (3), $w \rightarrow w_{eff}$ for microstrips.

A detailed discussion of term (3), effective width, is presented in Ref. [121] and [123]. The effective width arises from the demagnetization field. The internal field, or $\mathbf{H}_{eff}$ with terminology used in this chapter, is dependent on the demagnetization field $\mathbf{H}_{demag}$. When $\mathbf{M}$ is along a particular direction and uniform, $\mathbf{H}_{demag}$ is only anti-parallel to $\mathbf{M}$. Its magnitude is, however, highly nonuniform and drops off near the edges. The inhomogeneity of $\mathbf{H}_{demag}$, relative to $\mathbf{H}$, near the edges of the microstrips results in incomplete pinning, which is equivalent to pinned boundary conditions for a microstrip that extends past w. The analytical expression of the effective width is given as

$$w_{eff} = w \left[\frac{d}{d - 2} \right],$$

(6.4)

where d is a function of the aspect ratio $R = t/w$ and is defined as

$$d(R) = \frac{2\pi}{R[1 + 2ln(1/R)]}.$$

(6.5)

Also related to term (1) is term (4), shape anisotropy. Shape anisotropy is defined as a preferred direction of magnetization based on geometry called the easy axis and occurs

due to demagnetization field considerations. The effects of shape anisotropy are particularly important for magnetically soft alloys like Permalloy where the effects of other anisotropies are minimal. Other types of anisotropies are not discussed in detail in this thesis. The anisotropy involved in perpendicularly magnetized CoNi will be mentioned in Sec. 6.3. For further reading regarding other types of anisotropies, consider Ref. [1], [2], and [124]. The shape anisotropy energy of a saturated magnet is expressed as

$$\mathcal{E}_{shape} = \frac{1}{2} V \sum_{i=1}^{3} N_i M_i^2, \qquad (6.6)$$

where V is the volume and the term $N_i M_i$ are defined in the discussion of term (1). The shape anisotropy energy is minimized when the magnetization points along the axis i that corresponds to the smallest value of $N_i M_i$. For example, consider the geometry of a prolate ellipsoid. Following the calculations in Ref. [117], one finds that the demagnetization factor along the semi-minor axis is greater than the demagnetization factor along the semi-major axis. Based on energy minimization, the preferred direction of the magnetization is along the semi-major axis. For microstrips, the magnetization will point along the long axis of the microstrip in the absence of an external magnetic field due to the shape anisotropy.

Shape anisotropy is important in micrometer and nanometer sized structures and can be exploited. For example, figure 6.2 shows a pound key structure that contains a magnetic anti-vortex is shown in the lower right intersection. The anti-vortex was formed in the pound key structure using a two-step external magnetic field process discussed in Ref. [125]. A saturating magnetic field $\mathbf{H}_1$ is first applied at an angle of 45 °, as shown. The magnitude of $\mathbf{H}_1$ was chosen such that it is high enough to saturate the spins are along $\mathbf{H}_1$. The second magnetic field $\mathbf{H}_2$ was applied anti-parallel to $\mathbf{H}_1$. The magnitude of $\mathbf{H}_2$, is less than $\mathbf{H}_1$, and chosen such that the spins in legs 1 and 4 reverse direction while the spins in legs 2 and

3 remained the same, which occurs because the areas further out on legs 1 and 4 has lower shape anisotropy energy, hence they reverse at a lower magnetic field value.
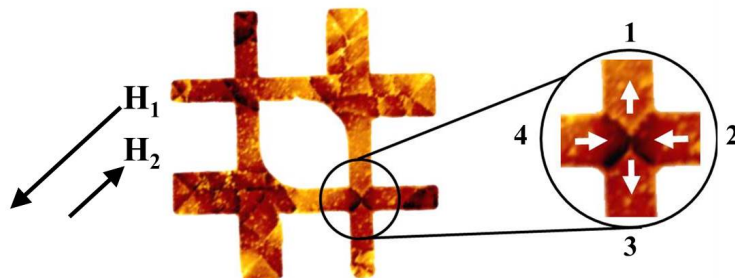
FIGURE 6.2. Magnetic force microscopy (MFM) image of a pound key structure showing the formation of an anti-vortex at one of the intersections. MFM measures the dipolar field from the sample and the arrows show the in-plane direction of magnetization. The overall dimension of the sample is $12 \times 12 \ \mu m^2$.

6.2. SPIN WAVE PROPAGATION IN PERMALLOY MICROSTRIPS

In the past decade, there have been numerous experimental studies of DE spin waves in Permalloy microstrips but BV spin waves have mostly been done by numerical simulations [126, 127]. This is likely due to the difficulty of directly exciting BV spin waves from a microwave antenna. The BV geometry offers convenience for applications since the spins naturally follow this geometry when not placed in an external magnetic field. Interference [128] and parametric excitation [129] techniques have been used to increase the efficiency of the BV spin wave generation. A direct comparison of the excitation efficiency of DE and BV spin waves has not, however, been done for microstrips. In this section, the efficiency of DE and BV spin waves that are directly excited by a microwave antenna are compared. Results of spin waves in a zero external magnetic field are also presented.

6.2.1. SAMPLE AND MICRO-BLS SETUP. The sample was fabricated using the cleanroom at Argonne National Laboratory by Helmut Schultheiβ and Katrin Vogt. The lithography process consists of laser writing and electron beam (e-beam) lithography, magnetron

sputtering, and liftoff. This was a multi-step process: (1) writing the microstrips with e-beam on a GaAs substrate, (2) deposition of the magnetic materials, which was 30 nm thick Permalloy, (3) writing the large structures of the microwave antenna, the contact pads for the picoprobes, with the laser writer, (4) writing the smaller structures of the microwave antenna that went over the microstrips with e-beam, and (5) deposition of the conductive materials that would carry the microwave current, which was 250 nm thick Au with a thin Cr adhesion layer.

Figure 6.3 shows the antenna and Permalloy setup. Figure 6.3(a) shows an illustration of the sample in the external magnetic fields in the DE and BV geometries. The Permalloy microstrip used in this study had a width $w = 2.5$ μm and the microwave antenna had a width $d = 2$ μm. (a) also shows the oscillating Oersted field produced by the microwave current that is used to excite spin waves. (b) is an image from the micro-BLS setup taken using a CMOS camera. The antenna was used to excite spin waves in the Permalloy microstrip at frequencies that varied from 2 to 10 GHz. Direction of the external magnetic field relative to the microstrip are shown corresponding to the DE and BV configurations. Both the top and bottom of the microstrip relative to the antenna in the CMOS image were measured to observe the reciprocity of the spin wave wavevector (spin waves traveling with opposite wavevectors). It is expected that DE spin waves with opposite wavevectors will have different excitation efficiencies, while BV spin waves with opposite wavevectors will have similar excitation efficiencies [130] For all measurements in this section the external magnetic field was held fixed at $H = 330$ Oe except when the field was turned off for the zero external magnetic field measurements. The micro-BLS setup discussed in Chap. 3 was used for the measurements because the dimensions of the microstrip was ideal for the resolution of the micro-BLS. The mirror spacing of the interferometer was set to 8 mm, which corresponds

to a free spectral range of 18.75 GHz. This frequency range was adequate to cover the spin

wave bandwidths for both the DE and BV spin waves for $H = 330$ Oe. Frequency and

one-dimensional spatial micro-BLS scans were used to observe spin wave generated by the

microwave antenna.
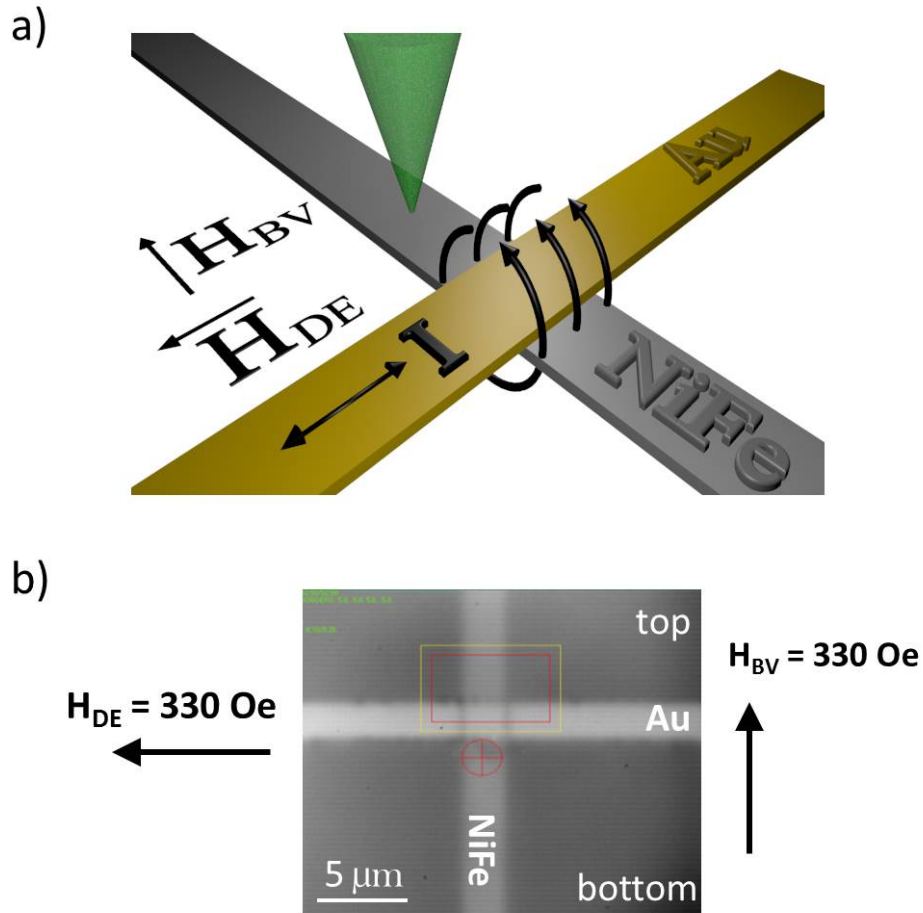
FIGURE 6.3. a) Illustration of the Permalloy microstrip sample and microwave antenna shown in the DE and BV geometries and b) a CMOS microscope image of the actual sample. The widths of the microwave antenna and Permalloy microstrips were $d = 2$ μm and $w = 2.5$ μm, respectively.

6.2.2. FREQUENCY-DEPENDENT MICRO-BLS MEASUREMENTS. Frequency-dependent

micro-BLS measurements were conducted where the frequency of the microwave current

used to pump the spin waves was varied from 3 to 10 GHz in 100 MHz steps. The generated

spin waves were measured at a distance $x = 1$ μm away from the antenna. The same integrated frequency range, the pumping frequency range, and the microwave power of 15 dBm were used for all measurements, as discussed in this subsection.

Although spin waves are pumped from a microwave antenna, thermal spin waves and side bands from the laser exist so a background subtraction must be performed on the data to allow for maximum signal to noise. Figure 6.4 illustrates how the background subtraction was performed. The complex micro-BLS plots are set up as BLS frequency f_{BLS} versus pumping frequency f_p. The intense horizontal peak seen at the top of the plots occur at $f_{BLS} = 0$. This is the reference peak from the laser. The main spin wave mode is identified as where f_{BLS} has a one-to-one correlation with f_p and is typically the most intense peak. The other modes are nonlinear modes but the analysis here will focus mainly on the main mode. Chapter 7 includes a discussion on further investigations into the nonlinear modes. A set of 5 background scans was collected for 1000 BLS scans with the microwave current turned off. The number of scans was the same as that of the one used for the measurements with the microwave source turned on. The set of background scans was averaged and subtracted directly from each dataset over the entire pumping frequency range.

The plots shown in Fig. 6.4 was an actual dataset for a DE configuration scan. Because the main spin wave mode was the mode of interest, the BLS signal was integrated over a frequency range of 1.25 GHz centered on f_p. The integrated frequency was plotted as a function of f_p and is shown in Fig. 6.5. (a) are the top and bottom spectra in the DE configuration while (b) shows the top and bottom spectra in the BV configuration. The BV spin waves are higher in frequency than the DE spin waves, which is expected based on their dispersion relations. A comparison of these frequency ranges with their dispersion relations
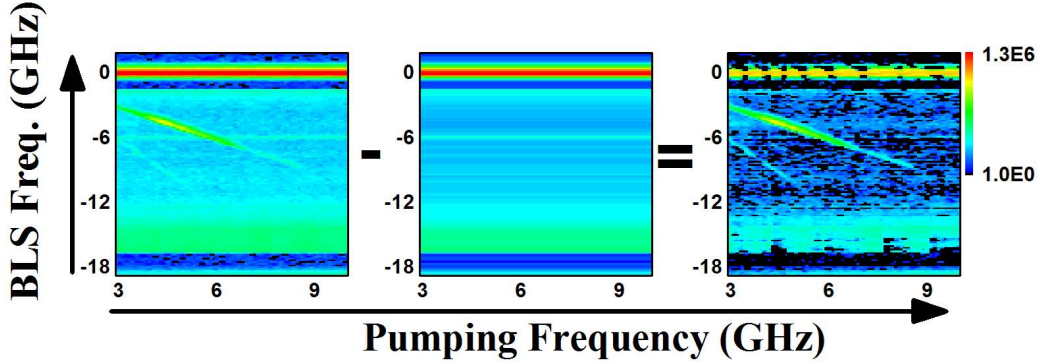
FIGURE 6.4. Background subtraction of the raw micro-BLS spectrum. A background scan was collected with the microwave source turned off. This background was subtracted from the raw spectrum shown on the left. The most notable noise was the band seen at 6 GHz. This was a side band of the laser and not a magnetic signal. After the background subtraction, the band at 6 GHz was suppressed. For proper comparison of the spin wave signal, all three plots are on the same intensity scale.

will be discussed in detail in Sec. 6.2.5. Also discussed in Sec. 6.2.5 will be the comparison of the intensities for each configuration.

6.2.3. SPATIAL-DEPENDENT MICRO-BLS MEASUREMENTS. Spin wave propagation was investigated through the measurements of one-dimensional spatial scans away from the antenna. A similar background subtraction and integration as described in Sec. 6.2.2 was used to analyze the measurements. The one-dimensional scan was made up of 28 points that spanned a total distance of approximately 7 μm. This distance is sufficient to capture the decay and was also the maximum distance that could be scanned without moving to a new reference point on the sample. The number of points was limited by the experimental resolution of the micro-BLS, which was 250 nm. To ensure that spin waves were measured as close to the antenna as possible, approximately 0.75-1 μm of the total distance was placed over the antenna.

The frequency scans in Figure 6.5 show that the DE and BV spin waves have different frequency profiles. The peak intensity occurs at 4.6 GHz for DE and at 6 GHz for the
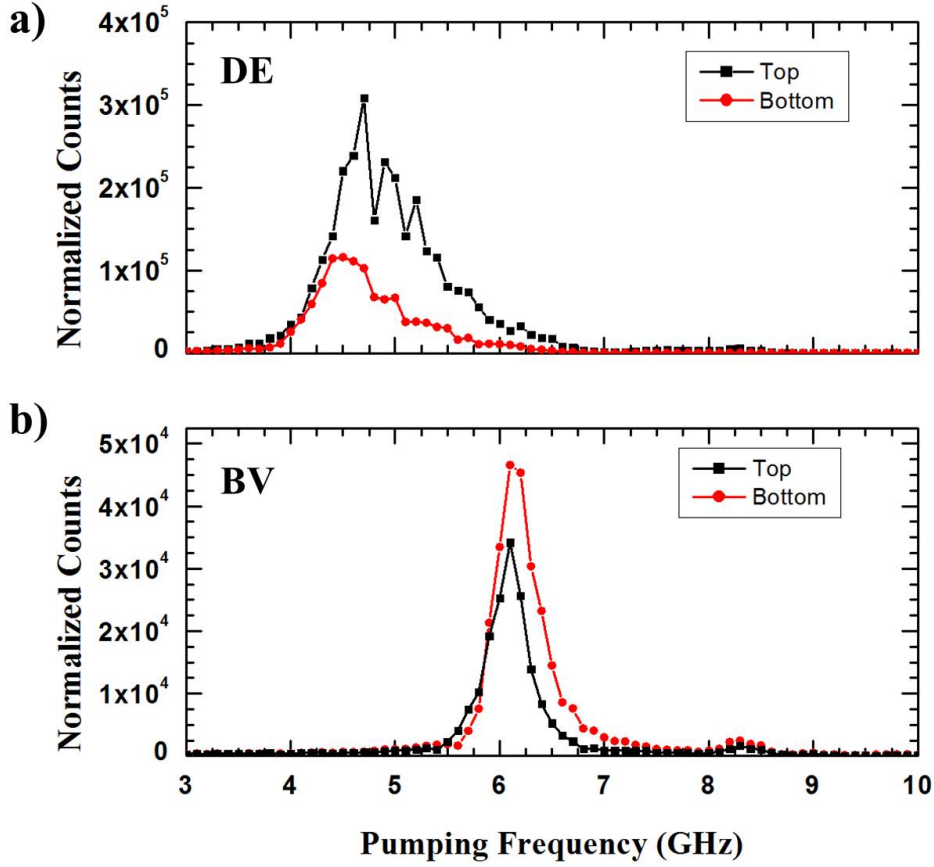
FIGURE 6.5. Integrated BLS counts as function of pumping frequency in the a) DE and b) BV configurations. Measurements were conducted on the top (black squares) and bottom (red circles) regions of the sample shown in Fig. 6.3(b). The external magnetic field and the microwave power for both cases was fixed at $H = 330$ Oe and at 15 dBm on the microwave generator, respectively.

BV spin waves. One-dimensional scans were conducted at these peak frequencies for each configuration. A large microwave power was chosen for these measurements to ensure that the signal could be easily observed at a large distance away from the antenna. The microwave power for the DE and BV measurements was 20 dBm.

Figure 6.6 shows top and bottom spatial micro-BLS measurements for the (a) DE and (b) BV configurations. The spatial measurements are plotted as spin wave intensities versus distance away from the antenna x. The signal was integrated over a 1 GHz frequency range and the same background subtraction method discussed in the previous section was

used. The bottom profiles show an exponential-like decay as a function of x, while the top profiles show a smooth but less rapid decay profile that is almost linear-like in behavior after approximately $x = 1$ μm. The behavior of these profiles will be discussed in Sec. 6.2.5.
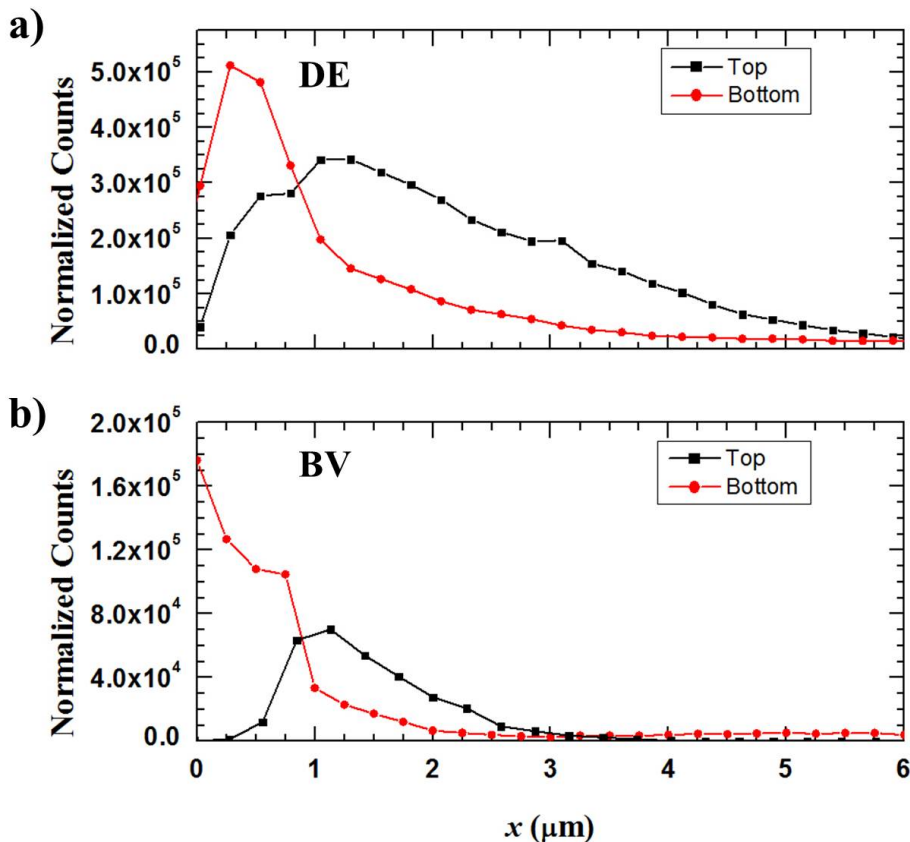
FIGURE 6.6. One-dimensional spatial micro-BLS spectra in the a) DE and b) BV configurations for a Permalloy microstrip 2.5 μm wide. As in Fig 6.5, measurements were conducted on the top (black squares) and bottom (red circles) of the sample. The bottom profiles show an exponential-like decay while the bottom profiles show linear behavior after approximately at $x = 1$ μm. The external magnetic field was held fixed at 330 Oe. The pumping frequency for the DE and BV measurements were 4.6 GHz and 6 GHz, respectively. The microwave power was set to 20 dBm on the microwave generator.

6.2.4. ZERO EXTERNAL FIELD MICRO-BLS MEASUREMENTS. Spin wave measurements were conducted in a similar manner as measurements discussed thus far in this chapter in the absence of an externally applied magnetic field ($H = 0$). Shape anisotropy ensures that

the magnetization will point along the long axis of the microstrip. The internal demagneti-zation field will point anti-parallel to the magnetization throughout most of the microstrip except for regions near the ends. The ends are far from the antenna so only the mid-section of the microstrip will be considered. Since $\mathbf{M}$ is along the wire, the spin waves will propagate in the BV configuration for $H = 0$.

Frequency-dependent measurements were made for pumping frequencies of 2 to 4 GHz in steps of 100 MHz. The microwave power was set to 15 dBm. The frequency scans were conducted at a fixed distance away from the antenna at $x = 1$ μm. Spatial-dependent measurements were also made over a total distance of 6.5 μm with a step size of approximately 232 nm (28 scan points) at a fixed frequency 2.9 GHz and at a microwave power of 18.5 dBm. This frequency was chosen because it corresponds to the peak intensity from the frequency-dependent scan. The microwave power used for these spatial scans were lower than in the previous sections because the generator produced unleveled signals above 18.5 dBm at a frequency of 2.9 GHz. The mirror spacing of the interferometer was set to 15 mm which corresponded to a FSR of 10 GHz.

Figure 6.7 shows frequency and one-dimensional spatial micro-BLS spectra for spin waves at $H = 0$. The frequency profiles are lower in frequency as compared to the BV measurements for $H > 0$ discussed in Sec. 6.2.2. This is expected since $\omega_H = 0$, which lowers the whole dispersion curve (Eq. 2.10). Consistent with Fig. 6.5(b) and Fig. 6.6(b), the bottom frequency profiles in (a) are slightly higher in intensity and the top spatial profiles in (b) show a linear-like decay after approximately $x = 1$ μm.

6.2.5. DISCUSSION ON PERMALLOY MICROSTRIPS. The data in Sec. 6.2.2, 6.2.3, and 6.2.4 were analyzed by comparing the peak intensities of the frequency profiles and com-paring the spin wave frequency range with the modified dispersions relations. The top and
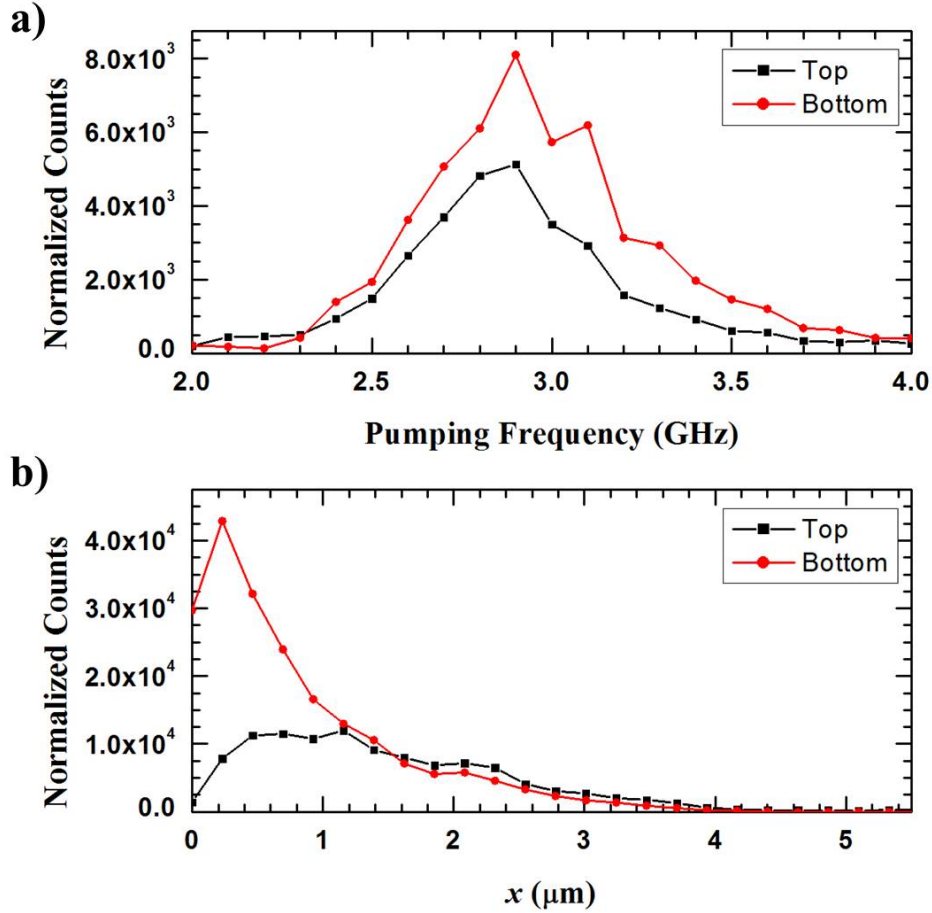
FIGURE 6.7. BLS a) frequency and b) spatial spectra for Permalloy microstrips with $H = 0$. The black (red) data are for the top (bottom) of the microstrip relative to the antenna. The microwave power for the frequency scans was 15 dBm from the generator. The spatial scans were done with a pumping frequency and a microwave power of 2.9 GHz and 18.5 dBm, respectively

bottom profiles were compared to each other for each configuration and then the individual configurations were compared to each other. The dispersion relations were modified to account for the quantized wavevector k_p and the demagnetization field H_{demag}.

Figure 6.8 compares the micro-BLS intensities versus frequency (Fig. 6.5) to the calculated dispersion relations. The measured spin wave frequencies are consistent with the calculated dispersion relation. The frequency ranges were limited by the maximum wavevector that can be excited by the microwave antenna. Based on the allowed wavevectors, the

accessible frequency range from the dispersion relation is $\Delta f = 6.35\text{-}5.87$ GHz for the BV configuration and $\Delta f = 5.81\text{-}4.43$ GHz for the DE configuration. This maximum wavevector is given by Eq. 5.1 in Chap. 5 and is 1.57 μm^{-1}, which is much smaller than the wavevector cutoff of the micro-BLS (17.7 μm^{-1}). The frequency with the highest BLS counts, which were frequencies chosen for the one-dimensional scans, were $f_{BV} = 6$ GHz and $f_{DE} = 4.6$ GHz for the BV and DE configurations, respectively. The red arrow is drawn to guide the eye to the wavevectors that correspond to f_{BV} and f_{DE}. These values were $k_{BV} = 0.94$ μm^{-1} and $k_{DE} = 0.41$ μm^{-1} according to the dispersion relations.

The dispersion relation was calculated using Eq. 2.10 by replacing H in the ω_H term with Eq. 6.1 and using Eq. 6.3 as the total spin wave wavevector. Only the lowest order modes, $n = 0$ and $p = 1$, are plotted. This mode has the highest excitation efficiency, which is inversely proportional to the quantization number [114]. The externally applied magnetic field was $H = 330$ Oe and the internal magnetic field (Eq. 6.1), which is $H\text{-}H_{demag}$, is 328 Oe and 248 Oe for the BV and DE configurations, respectively. The demagnetization field that was used to determine the internal magnetic field was calculated from micromagnetic simulations [120]. These internal magnetic field values agree well with the approximation given in Ref. [119], which yields $H_{DE} = 254$ Oe and $H_{BV} = 330$ Oe. The demagnetization field in the DE configuration is expected to be much lower and should tend towards zero for a long wire, as discussed in Ref. [121].

Figure 6.9 shows a comparison of the calculated dispersion relation to the measured spin wave intensities in Fig. 6.7(a). The dispersion relation is calculated with Eq. 2.10 using $H = 0$ in Eq. 6.1. At zero external magnetic field the internal magnetic field was due solely to H_{demag}, which was determined from micromagnetic simulations to be 2.3 Oe, which is essentially zero. The frequency range that corresponded to the spin wave bandwidth was

FIGURE 6.8. Comparison the of spin wave frequencies in Fig. 6.5 (right) with calculated dispersion relations (left). The calculations were done with the following parameters: $H_{DE} = 248$ Oe, $H_{BV} = 328$, $\gamma/2\pi = 2.93$ MHz/Oe, $4\pi M_s = 10000$ G, $\alpha = 2.8 \times 10^{-13}$ cm^2, and $w_{eff} = 2.6$ μm. DE spin waves (black) are shown in a) and BV spin waves (blue) are shown in b). The wavevector cutoff from the antenna is shown as a gray region in the dispersion plots. The frequency ranges that fall outside of the frequency range associated with $k = 0$ and k_{cutoff} are shown as gray regions in the micro-BLS spectra. Red arrows indicate the wavevectors of the spin waves that are most efficiently excited according to experimental measurements.

$\Delta f = 3.74\text{-}2.92$ GHz, according to the calculated dispersion relation. The corresponding spin wave wavevector for the most efficient frequency of 2.9 GHz was 1.58 μm^{-1}.

The FMR frequency is calculated using Eq. 2.5 with demagnetization factors of N_x = 0, $N_y = 0.092$, and $N_z = 12.47$ for microstrips. The value for N_y is calculated using
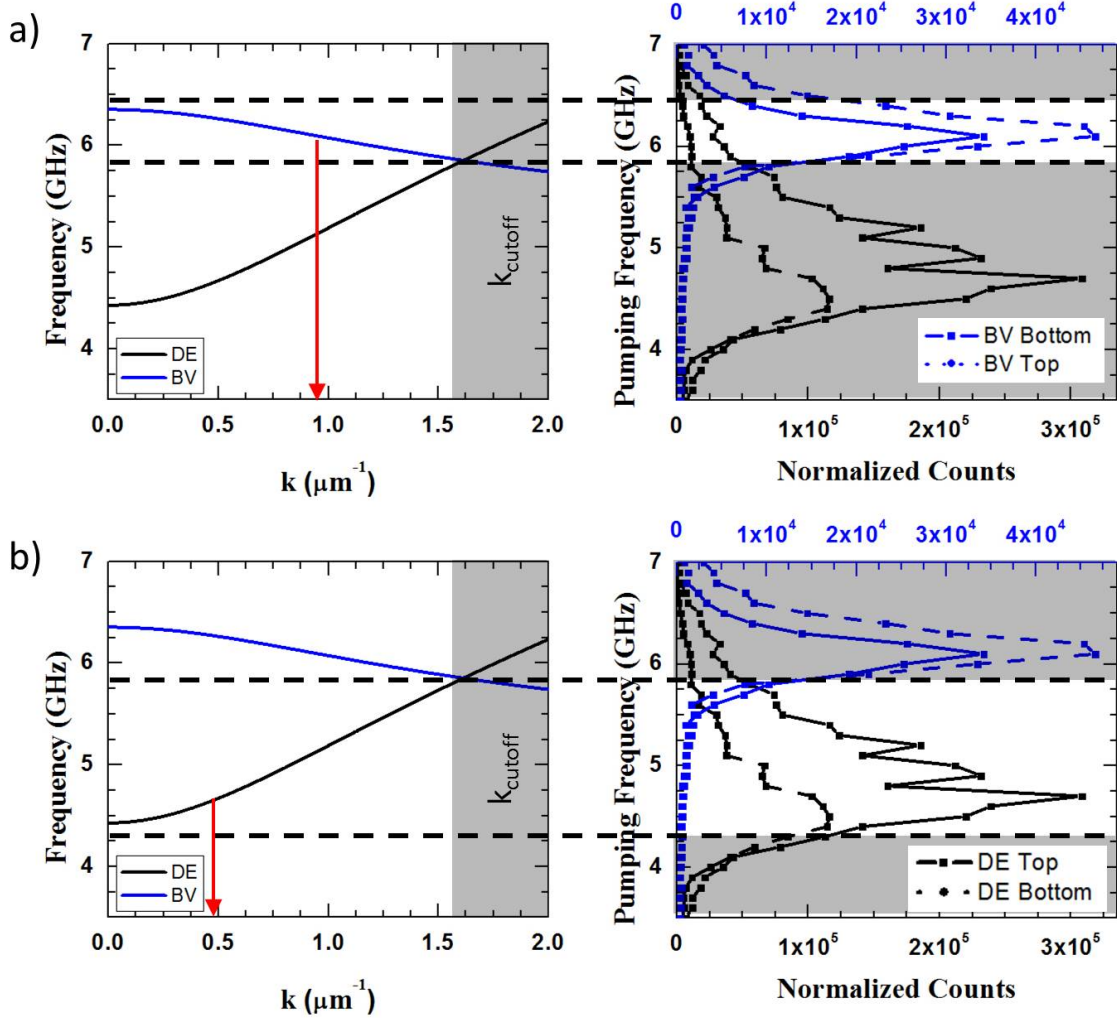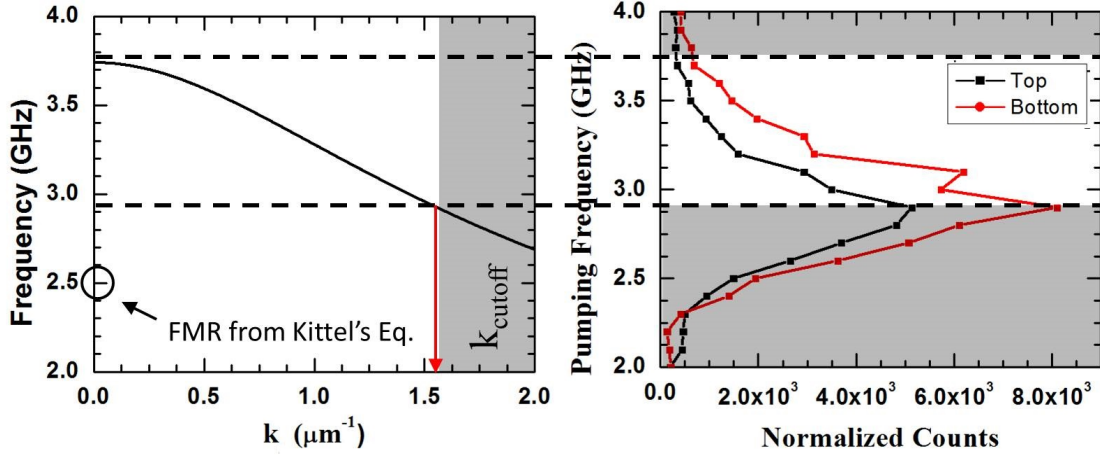
FIGURE 6.9. Comparison of the spin wave frequencies in Fig. 6.7(a) (right) with calculated dispersion relations (left). The calculations were done with the following parameters: $H = 0$, $\gamma/2\pi = 2.93$ MHz/Oe, $4\pi M_s = 10000$ G, $\alpha = 2.8 \times 10^{-13}$ cm^2, and $w_{eff} = 2.6$ μm. The wavevector cutoff from the antenna is shown as a gray region in the dispersion plot. The frequency ranges that are expected to be outside of the detection range are shown as gray regions in the micro-BLS spectra. The red arrow indicates the wavevector of the spin waves that are most efficiently excited. The FMR frequency using Eq. 2.5 is identified at 2.5 GHz.

the effective width w_{eff}. The determination of the demagnetization factors was discussed in Sec. 6.1.1. This yields an FMR frequency of 2.50 GHz, whereas the FMR frequency for an extended film with $H = 0$ tends towards zero. Hence the dynamic demagnetization contributions should be included in order to obtain reasonable agreement. Although the dispersion did take into account wavevectors that are quantized across the microstrip width, it did not take into account the dynamic demagnetization factors as Kittel's equation did. This is likely why the range of frequencies is consistent with the dispersion relation but the magnitude of the frequencies does not agree as well. A more complete calculations of the dispersion relation that takes into account the microstrip geometry and internal magnetic field is needed but is beyond the scope of this study.

A comparison of the spin wave intensities in Fig. 6.5 and 6.7(a) provides evidence of spin wave excitations in the BV geometry. The ratio of the DE intensities for the most efficient

frequency is 2.7. The large difference in intensities is expected due to the nonreciprocity of the DE spin waves [130]. The BV mode intensities on the other hand shows reciprocal behavior for opposing wavevectors. The ratio of the top and bottom BV peaks intensities are 1.4 for $H = 330$ Oe and 1.6 for $H = 0$. These ratios are close to the expected value of unity for BV spin waves. The ratio of intensities of DE spin waves versus BV spin waves at their respective peak intensities is approximately 10. The low efficiency of BV spin waves versus DE spin waves can be a reason for the lack of experiments reported in the literature using such spin waves in confined microstrips.

The spatial decay profiles shown in Fig. 6.6 and 6.7(b) show unexpected differences between the top and bottom measurements. Collectively, the top profiles show an exponential-like decay while the bottom profiles are linear-like after 1 μm. There is no physical reason why the two should show different functional behavior if the sample is symmetric. The linear-like behavior is puzzling and more experiments are currently being done to investigate this phenomena in more detail. A possible cause would be asymmetries in the sample layout. The antenna leads are located near the bottom side of the microstrip, which can produced Oersted fields that may affect the decay in the microstrip. The exponential-like decay is expected and has been studied by Ref. [131], which provides a functional form of an exponential, which uses the decay length λ, among other parameters, as fitting parameters:

$$I_{BLS} \propto \left| A \left[exp \left(ikx - \frac{x}{\lambda} \right) + \frac{1}{b} exp(i\phi) Log \left(\frac{x}{x+a} \right) \right] \right|^2 + T.$$ (6.7)

This functional form applies to continuous films and not microstrips for large wavevectors. Reference [131] also provides an analytical expression, which is given as

$$\lambda = \frac{v_g}{\alpha \gamma (H + 2\pi M_s)}.$$ (6.8)

Reference [114] provides a model for mode beating and interference but uses a simple exponential decay ($I_{BLS} \propto \exp(-x/\lambda)$) to fit for the λ. For completeness, Table 6.1 tabulates the decay lengths from fits and analytical expressions discussed in Ref. [114] and [131]. $\lambda_{fit,1}$ corresponds to the simple exponential used in Ref. [114]. $\lambda_{fit,2}$ and λ_{calc} correspond to Eq. 6.7 and Eq. 6.8, respectively. Also included are the wavevectors and group velocities extracted from the dispersion relation. These decay length fits seem to be specific to their respective experiments rather than general. The exact reason for the discrepancies between the fits is unknown at this time and further investigation is required to determine the cause.

TABLE 6.1. Comparison of Decay Length in Permalloy Microstrips

Config.	f_p (GHz)	k (μm^{-1})	v_g (μm/ns)	$\lambda_{fit,1}$ (μm)	$\lambda_{fit,2}$ (μm)	λ_{calc} (μm)
BV	6.1	0.94	2.46	0.76 ± 0.08	2.37 ± 0.82	3.21
DE	4.6	0.41	5.32	0.86 ± 0.06	3.69 ± 0.39	7.03
BV ($H = 0$)	2.9	1.58	3.61	0.80 ± 0.02	4.94 ± 0.35	4.99

6.3. SPIN WAVES IN CONI MULTILAYERED MICROSTRIPS

Cobalt nickel (CoNi) multilayers are thin ferromagnetic films that are typically only a few nanometers thick. CoNi films have perpendicular magnetocrystalline anisotropy: there is a strong tendency for the magnetization to point perpendicular to the film surface. There have recently been a large increase in research on films with perpendicular anisotropy, including CoNi multilayers due to the advancement in spintronics. CoNi multilayers have high giant magnetoresistive properties, which makes them suitable for spin polarization devices [132–137].

Magnetostatic forward volume wave (MSFVW) spin waves in perpendicularly magnetized thin films are rarely studied using BLS because it is experimentally difficult to produce the large external magnetic field needed to overcome the in-plane shape anisotropy and

saturate the spins out-of-plane for most magnetic films [23]. With using CoNi multilayers, perpendicular anisotropy acts as an effective field perpendicular to the surface of the film and it has large remnant state after being saturated out-of-plane, thus only a small external magnetic field should be needed to achieve a state where MSFVW spin waves can propagate.

In this study, spin waves in CoNi multilayers are observed with micro-BLS. The measurements provided in this section are preliminary measurements in CoNi multilayers. These measurements show evidence that spin waves in perpendicularly magnetized thin films can be observed with the micro-BLS. The measurements also include in-plane external magnetic field experiments following Ref. [138]. The purpose of the in-plane external magnetic field is to tilt the magnetization in plane to allow for greater signal-to-noise and to observe possible domain wall oscillation.

6.3.1. SAMPLE AND MICRO-BLS SETUP. The CoNi sample was fabricated in collaboration with the Kent group at New York University. Ferran Macià of the Kent group deposited the CoNi according to the mask design for microstrips that the author of this thesis provided to them. The CoNi was deposited onto a 3 inch silicon substrate with capping and base layers that formed a stacked composition of 3Ta|(0.2Co|0.6Ni)×6|0.2Co|3Pt (thickness in nanometers). The microwave antennae that were used to excite spin waves were fabricated at the Colorado Nanofabrication Laboratory in Boulder, CO. The design of the mask and the photolithography procedure used to fabricate the microwave antennae can be found in Appendix A. For the study presented in this thesis, the CoNi microstrip was 5 μm wide and 200 μm long. The microwave antennae were made from approximately 200 nm thick thermally evaporated Au on a 10 nm thick Cr underlayer and was approximately 2 μm wide.

The measurements in this section were done using both out-of-plane and in-plane external magnetic fields. The out-of-plane magnetic field was provided by placing the sample

at three different distance above a permanent magnetic using Plexiglas spacers. The in-plane magnetic field was provided by the same electromagnet that was used in the in-plane measurements discussed in the previous sections.

6.3.2. OUT-OF-PLANE MAGNETIC FIELD- AND FREQUENCY-DEPENDENT micro-BLS MEASUREMENTS. Figure 6.10 shows frequency-dependent micro-BLS measurements conducted at three out-of-plane external magnetic field values: $H = 1.33$, 1.66, and 2.10 kOe. At each value of H, the pumping frequency was varied from 2 to 15 GHz in 250 MHz steps and at a microwave power of 16 dBm from the generator. A total of 3000 BLS scans were conducted at a distance away from the antenna of $x = 0.5$ μm.

The integration routine and background subtraction discussed in Sec. 6.2 were used to extract the spin wave modes from the frequency measurements. Because the overall spin wave signal in the CoNi microstrips were noticeably less than the spin wave signals shown in Sec. 6.2, a baseline noise floor is identified. This noise floor is shown as a red dashed horizontal line and is consistently around 180 counts for 3000 scans. This noise floor is due to the fact that the integration routine sums up background counts within the specified frequency range of 1.25 GHz centered on f_p.

The external magnetic field value of $H = 1.66$ kOe was chosen to further investigate properties of the CoNi microstrip. This value of H was chosen because the signal was large compared to the noise floor and the spin wave peak showed a well-defined profile with the frequency scan range. At this value of H, the spin wave peak was centered near 3.5 GHz.

Figure 6.11 shows a two-dimensional spatial scan that was conducted to observe the spin wave profile away from the antenna. The scan was done at a fixed pumping frequency of 3.5 GHz and at a microwave power of 19 dBm from the generator. The spin wave signal emitted
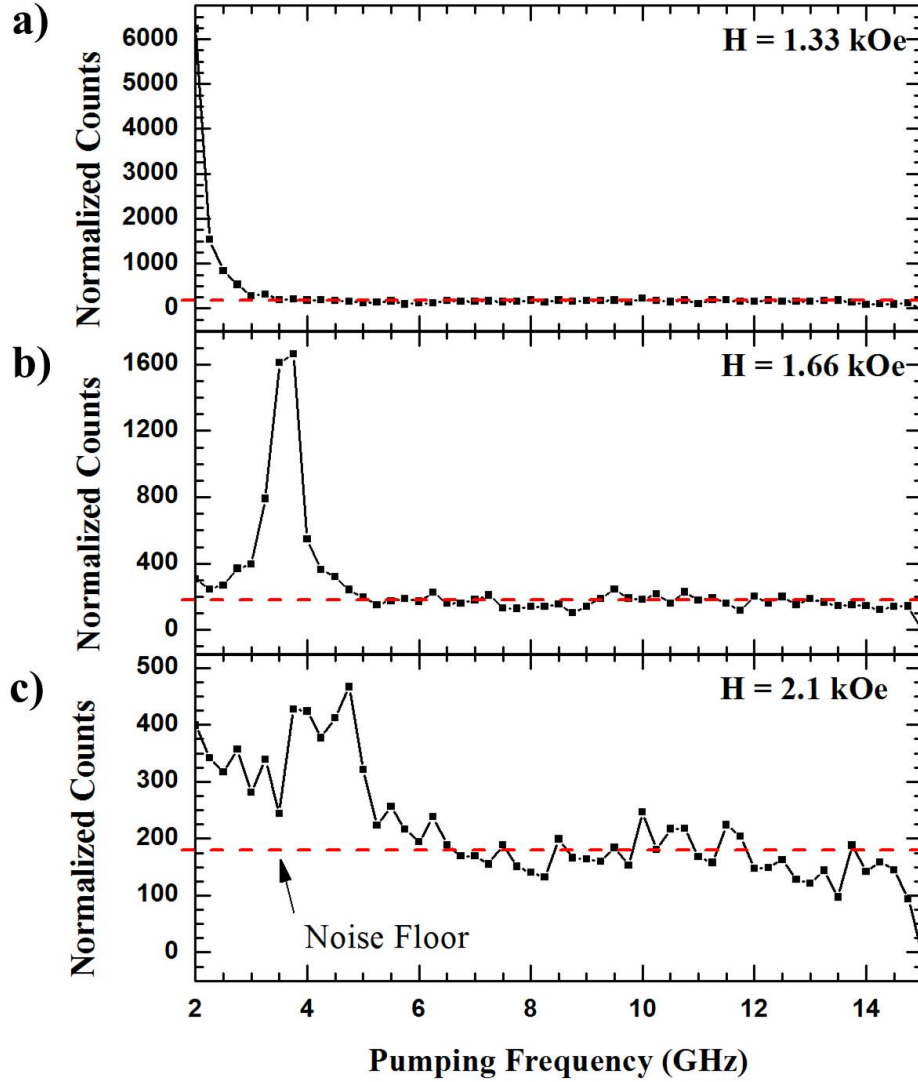
FIGURE 6.10. Frequency-dependent micro-BLS measurements of a CoNi microstrip in a perpendicular external magnetic field of a) 1.33 kOe, b) 1.66 kOe, and c) 2.10 kOe. The horizontal red dashed line represents the noise from the integration routine, which is consistently around 180 counts. The frequency measurements were conducted at a fixed distance of $x = 0.5$ μm and at the center of the microstrip $y = 0$.

from the antenna appears to not extend farther than 1 μm away from the antenna excite for

a signal that appears around 2 μm away from the antenna at the center of the microstrip.

Figure 6.12 shows a pumping frequency-dependent scan near the edge of the sample.

Although edge modes are not discussed in this thesis, the purpose of this scan was to see

if there were a difference in spin wave frequencies near the edge compared to the center.
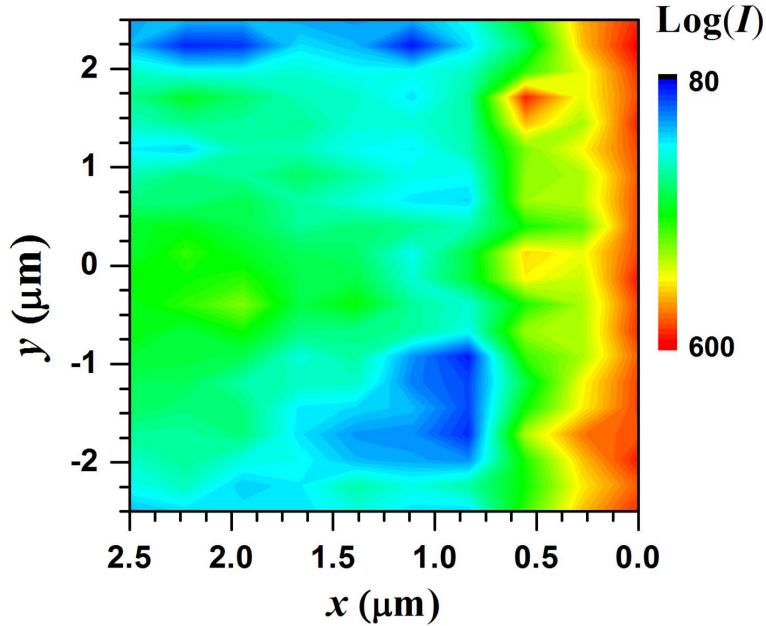
FIGURE 6.11. Two-dimensional spatial scan away from the antenna at $H = 1.66$ kOe. The spatial scans were conducted at a fixed pumping frequency of 3.5 GHz.

The measurements were conducted at a fixed position, $x = 0.5$ μm and $y = 2.0$ μm. The frequency was varied from a range of 1.5 to 4.5 GHz in 100 MHz steps. The frequency profile near the edge compared to the center shows a slight increase in frequency that is around 200 MHz. Edge modes are expected to be lower in frequency [21].

6.3.3. In-plane Magnetic Field- and Frequency-Dependent micro-BLS Measurements. The next measurement was done following Ref. [138]. This reference discussed measuring continuous (unpatterned) CoNi films with a purely in-plane magnetic field. An in-plane magnetic field slowly tilted the magnetization from out-of-plane to in-plane as the magnetic field was increased. They reported both high and low frequency spin wave modes (Fig.4 of Ref. [138]). Figure 6.13 shows a complex frequency versus in-plane magnetic field micro-BLS spectrum. These measurements were conducted at a fixed distance of $x = 2.5$ μm and $y = 0$ μm. The data show that there may be a low frequency spin wave signal at higher
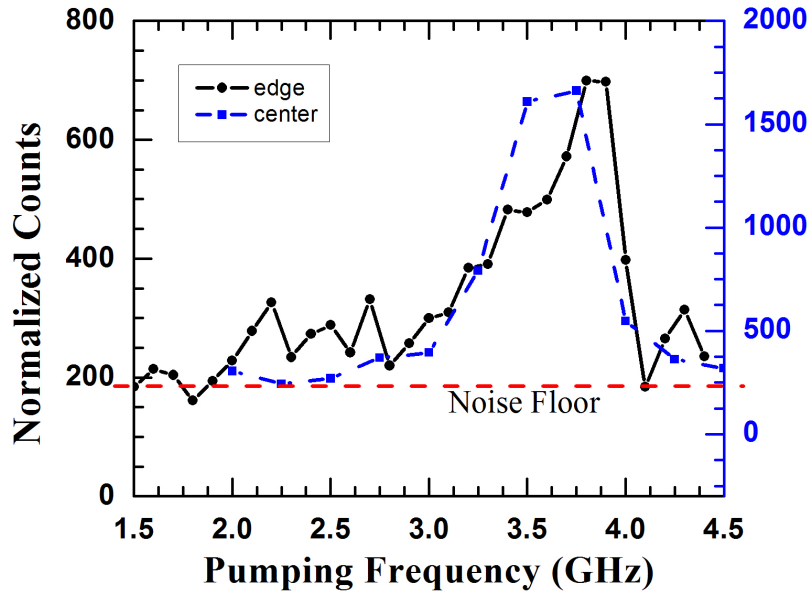
FIGURE 6.12. Frequency-dependent micro-BLS measurements at the edge of the CoNi microstrip for $H = 1.66$ kOe. The position of the measurements were at $y = 2.0$ μm and $x = 0.5$ μm. The frequency-dependent measurement at the center of the microstrip from Fig. 6.10(b) corresponding to the same magnetic field value is shown in the blue dashed line for comparison.

H. It is difficult to determine if there is a distinct spin wave signal in the high frequency measurements.
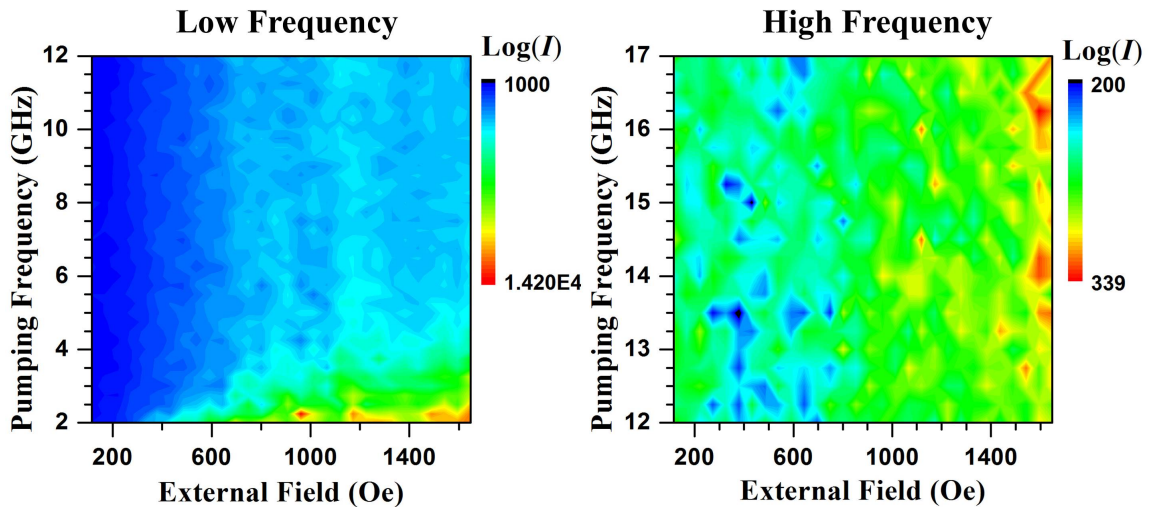
FIGURE 6.13. Complex frequency- and in-plane magnetic field-dependent micro-BLS measurements. The in-plane magnetic field was applied perpendicular to the long axis of the microstrip.

6.3.4. DISCUSSION ON CONI MICROSTRIPS. The CoNi data presented in this chapter are preliminary measurements and open questions still remain regarding the origin of the observed signals. It was shown that micro-BLS can be used to measure a magnetic signal from CoNi films with perpendicular anisotropy in an out-of-plane external magnetic field. The in-plane magnetic field measurements were limited by the maximum strength of the external magnetic field (approximately 1.60 kOe). A larger magnet would be needed in order to observe the spin wave modes discussed in Ref. [138].

Figure 6.14 shows the dispersion relation using Eq. 2.9 for $H = 1.33$, 1.66, and 2.10 kOe. The determination of material parameters like $\gamma/2\pi = 2.93$ MHz/Oe, $4\pi M_s = 9362$ G, $H_k = 11114$ Oe, and $\alpha = 2.87 \times 10^{-13}$ cm^2 can be found in Ref. [137]. H_k is a perpendicular anisotropy field that is taken as an additive term to H in the dispersion relation. The expected FMR frequency from the dispersion relation ($k = 0$) agrees well with the FMR frequency presented in Ref. [137]. The measured frequencies shown in Fig. 6.10 are lower than that predicted by the calculated dispersion relation. The dispersions relations start around 9 Ghz for $H = 1.33$ kOe and the measured BLS frequency start lower than 3 GHz for the same external magnetic field value. It is unknown at this time as to why the dispersion relations do not agree with the observed micro-BLS frequency from Fig. 6.10. One possible reason is that the focused laser from the microscope objective may have heated the sample and destroyed some of the perpendicular anisotropy, which would change the expected frequencies considerably. It is also possible that the sample may not have been completely saturated and that domains may be present, which would lead to difference resonance frequencies.
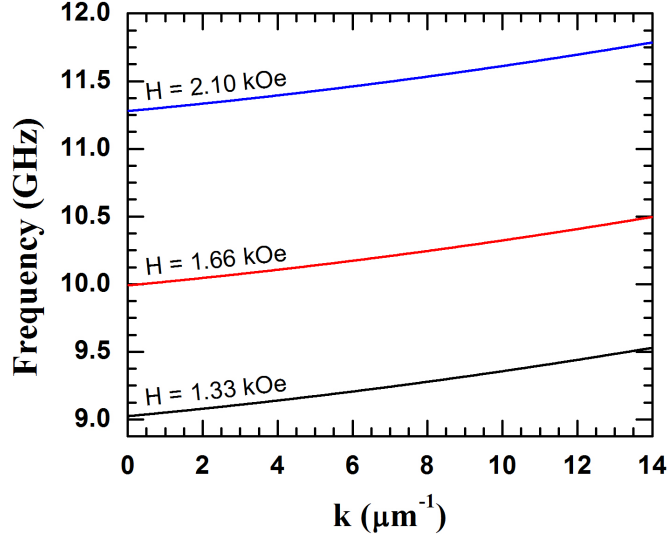
FIGURE 6.14. MSFVW dispersion relations calculated using Eq. 2.9. The calculations were done with the following parameters for the CoNi thin film: $\gamma/2\pi = 2.93$ MHz/Oe, $4\pi M_s = 9362$ G, $H_k = 11114$ Oe, $\alpha = 2.87 \times 10^{-13}$ cm^2, $t = 2.8$ nm and $w = 5.0$ μm.

6.4. CONCLUSIONS

In summary, a series of spin wave measurements made using the recently developed micro-BLS have been presented. Spin waves in Permalloy microstrips that were directly excited by a microwave antenna were measured in the DE and BV configurations. The peak intensities of the frequencies were compared and the DE spin waves showed an expected larger asymmetry in excitation efficiency for opposite wavevectors than their BV counterparts. BV spin waves were also observed in Permalloy microstrips with zero applied external magnetic field providing evidence that spin waves can be directly excited in the BV configuration even in zero field. Preliminary measurements in CoNi showed that a magnetic signal was observed with both out-of-plane and in-plane external magnetic fields, however open questions remain regarding the origin of the detected signal.

CHAPTER 7

Conclusions

7.1. Results

This thesis provided experimental measurements of spin waves in magnetic thin films using Brillouin light scattering (BLS). Spin wave dispersion relations were used to fit and compare spin wave frequencies obtained from the BLS measurements. In Chap. 4, the dispersion relations were used to fit the DE spin wave mode and PSSW modes to obtain the exchange parameter α for FeCo films. The fits resulted in $\alpha = 1.53 \pm 0.04 \times 10^{-13}$ cm^2 and a Landé g-factor of $g = 2.07 \pm 0.02$. In Chap. 5, space- and time-resolved BLS were used to extract the spin wave group velocities for directly pumped magnons as well as those created through two nonlinear processes, three magnon splitting and confluence. The group velocities agreed well with the calculated group velocities from the dispersion relations. Analysis of the arrival times showed that the splitting magnons formed at a distance of 1.7 $\pm$ 0.2 mm away from the microwave antenna. In Chap. 6, the micro-BLS was used to measure spin waves in Permalloy and CoNi microstrips. The measurements in Permalloy microstrips experimentally showed that DE spin waves with opposite wavevectors have a larger asymmetry in peak spin wave intensities as compared to BV spin waves with opposite wavevectors. BV spin waves were also observed in zero external magnetic field. The CoNi measurements showed that a magnetic signal can be detected in films with perpendicular anisotropy using micro-BLS, however further studies will be needed to determine if the signal is that of a forward volume propagating spin wave. In summary, BLS is a useful tool for studying linear and nonlinear spin waves in continuous and patterned thin films.

7.2. Future Work

Currently, there are two experiments that warrant further investigation: spin waves in Permalloy and CoNi microstrips. There is some indication of nonlinear effects in the Permalloy data. Therefore, it would be useful to repeat the measurements at a low microwave power where nonlinear effects are minimal. The experiments presented in this thesis used an external magnetic field that was in a single direction. Switching the direction of the external magnetic field will directly check the asymmetry of the spin wave wavevectors in the microstrips. This also may give insight into the odd spatial decay behavior that was observed. High microwave power measurements could also to be repeated to obtain two-dimensional spatial scans with the micro-BLS. With the high microwave power, nonlinear spin waves can be mapped spatially, which may show interesting propagation behavior.

The work on CoNi microstrips were preliminary measurements that showed that a signal was detected in films with perpendicular anisotropy. The the out-of-plane external magnetic field measurements were done by placing spacers between a permanent magnet to change the magnetic field value. This technique was adequate for observing a signal but for a detailed external magnetic field treatment it is insufficient. Colton Fluhling has designed an apparatus using a permanent magnetic on a translation stage that can be varied in a more controlled manner. This apparatus will allow for out-of-plane external magnetic field-dependent micro-BLS measurements with a maximum magnetic field of a few thousand Oersteds.

Measurements were also done with an in-plane external magnetic field, however, the maximum field that could be applied was approximately 1.6 kOe, which may not have been sufficient to saturate the sample in-plane. Producing higher magnetic field values will require redesigning the current electromagnet. Higher magnetic field values would allow one

to determine whether the magnetic signal that was detected is from domain wall oscillations or from spin wave propagation.

The Permalloy and CoNi microstrips were presented as preliminary work for a proposed spin wave interference project. This project involved spin waves propagating down microstrips and interfering at a right angle intersection. In the Permalloy microstrips, the interference of DE and BV spin waves may provide interesting results based on the interaction between two different types spin wave modes. In the CoNi microstrips, two magnetostatic forward volume spin waves would interfere, which has not yet been observed.

7.3. Micro-BLS Technique

The micro-BLS is a relatively new technique that can be used to effectively measure localized spin dynamics in microstructures. Its current limitation, compared to conventional BLS, is that the angle of the incident light is fixed by the microscope objective. This limits the micro-BLS because it collects light from all angle of incidence that vary from $0 \leq \phi \leq 48.6°$. This limitation does not allow the micro-BLS to observe a single spin wave wavevector. Singling out a spin wave wavevector provides a means to directly identify the spin wave mode that is excited. A possible improvement that would allow for singling out a spin wave wavevector would be to restrict the angles of the scattered light that are to the TFP with a mask. This setup would be analogous to the conventional backscattering configuration. One would have to weigh the value of additional information obtained against the reduction in the signal-to-noise due to reduced intensity of the incident light.

Bibliography

[1] C. Kittel, *Introduction to Solid State Physics*. Hoboken, NJ: John Wiley and Sons, Inc., 8th ed., 2005.

[2] D. D. Stancil and A. Prabhakar, *Spin Waves: Theory and Applications*. New York, NY: Springer, 2010.

[3] R. Krishnan, K. V. Rao, and H. H. Liebermann, "Magnetization and FMR studies in amorphous $Fe_{90}Zr_{10}$ and $Fe_{70}Ni_{20}Zr_{10}$ ribbons," *Journal of Applied Physics*, vol. 55, no. 6, 1984.

[4] "Are single phase manganite samples truly homogeneous? A magnetic resonance study," *Solid State Communications*, vol. 97, no. 3, pp. 193–196, 1996.

[5] J. Das, S. S. Kalarickal, K.-S. Kim, and C. E. Patton, "Magnetic properties and structural implications for nanocrystalline Fe-Ti-N thin films," *Physical Review B*, vol. 75, p. 094435, Mar 2007.

[6] R. C. Taylor and A. Gangulee, "Magnetization and magnetic anisotropy in evaporated GdCo amorphous films," *Journal of Applied Physics*, vol. 47, no. 10, 1976.

[7] "Anisotropy fields and FMR linewidth in single-crystal Al, Ga and Sc substituted hexagonal ferrites with M structure," *Materials Research Bulletin*, vol. 19, no. 3, pp. 385–392, 1984.

[8] X. Liu, Y. Sasaki, and J. K. Furdyna, "Ferromagnetic resonance in $Ga_{1-x}Mn_xAs$: Effects of magnetic anisotropy," *Physical Review B*, vol. 67, p. 205204, May 2003.

[9] M. J. Hurben, D. R. Franklin, and C. E. Patton, "Angle dependence of the ferromagnetic resonance linewidth in easy-axis and easy-plane single crystal hexagonal ferrite disks," *Journal of Applied Physics*, vol. 81, no. 11, 1997.

[10] "Anisotropic low-temperature FMR linewidth in nickel and the theory of anomalous damping," *Journal of Magnetism and Magnetic Materials*, vol. 104107, Part 3.

[11] R. Urban, G. Woltersdorf, and B. Heinrich, "Gilbert damping in single and multilayer ultrathin films: Role of interfaces in nonlocal spin dynamics," *Physical Review Letters*, vol. 87, p. 217204, Nov 2001.

[12] R. Yilgin, M. Oogane, Y. Ando, and T. Miyazaki, "Gilbert damping constant in polycrystalline CO_2MnSi Heusler alloy films," *Journal of Magnetism and Magnetic Materials*, vol. 310, no. 2, Part 3, pp. 2322–2323, 2007. Proceedings of the 17th International Conference on Magnetism The International Conference on Magnetism.

[13] N. Mo, J. Hohlfeld, M. Ul Islam, C. S. Brown, E. Girt, P. Krivosik, W. Tong, A. Rebei, and C. E. Patton, "Origins of the damping in perpendicular media: Three component ferromagnetic resonance linewidth in Co-Cr-Pt alloy films," *Applied Physics Letters*, vol. 92, pp. 022506–022506–3, Jan 2008.

[14] D. J. Griffiths, *Introduction to Electrodynamics.* Upper Saddle River, NJ: Prentice-Hall, Inc., 3th ed., 1999.

[15] J. D. Jackson, *Classical Electrodynamics.* New York, NY: John Wiley and Sons, Inc., 3th ed., 1999.

[16] W. D. Wilber, *A Brillouin Light-Scattering Study of Parametric Magnons in Yttrium Iron Garnet at Microwave Frequencies.* CSU Thesis/Dissertation, Colorado State University, 1987.

[17] C. Kittel, "On the theory of ferromagnetic resonance absorption," *Physical Review*, vol. 73, pp. 155–161.

[18] R. W. Damon and J. Eshbach, "Magnetostatic modes of a ferromagnet slab," *Journal of Physics and Chemistry of Solids*, vol. 19, no. 3, pp. 308–320, 1961.

[19] J. P. Park, P. Eames, D. M. Engebretson, J. Berezovsky, and P. A. Crowell, "Spatially resolved dynamics of localized spin-wave modes in ferromagnetic wires," *Physical Review Letters*, vol. 89, p. 277201, Dec 2002.

[20] C. Bayer, J. Jorzick, B. Hillebrands, S. O. Demokritov, R. Kouba, R. Bozinoski, A. N. Slavin, K. Y. Guslienko, D. V. Berkov, N. L. Gorn, and M. P. Kostylev, "Spin-wave excitations in finite rectangular elements of $Ni_{80}Fe_{20}$," *Physical Revview B*, vol. 72, p. 064427, Aug 2005.

[21] B. B. Maranville, R. D. McMichael, S. A. Kim, W. L. Johnson, C. A. Ross, and J. Y. Cheng, "Characterization of magnetic properties at edges by edge-mode dynamics," *Journal of Applied Physics*, vol. 99, no. 8, 2006.

[22] V. E. Demidov, M. Buchmeier, K. Rott, P. Krzysteczko, J. M, G. Reiss, and S. O. Demokritov, "Nonlinear hybridization of the fundamental eigenmodes of microscopic ferromagnetic ellipses," *Physical Review Letters*, vol. 104, p. 217203, May 2010.

[23] B. A. Kalinikos. personal communication.

[24] B. A. Kalinikos, *Linear and Non-linear Spin Waves in Magnetic Films and Superlattices*, ch. Dipole-exchange spin-wave spectrum of magnetic films. Singapore: World Scientific Publishing Company, 1994.

[25] B. A. Kalinikos and A. N. Slavin, "Theory of dipole-exchange spin wave spectrum for ferromagnetic films with mixed exchange boundary conditions," *Journal of Physics C: Solid State Physics*, vol. 19, no. 35, p. 7013, 1986.

[26] B. A. Kalinikos, "Excitation of propagating spin waves in ferromagnetic films," *Microwaves, Optics and Antennas, IEEE Proceedings H*, vol. 127, no. 1, p. 4, 1980.

[27] B. Hillebrands, "Spin-wave calculations for multilayered structures," *Physical Review B*, vol. 41, pp. 530–540, Jan 1990.

[28] P. H. Gammon, H. Kiefte, and M. J. Clouter, "Elastic constants of ice samples by Brillouin spectroscopy," *The Journal of Physical Chemistry*, vol. 87, no. 21, pp. 4025–4029, 1983.

[29] A. D. Alvarenga, M. Grimsditch, and R. J. Bodnar, "Elastic properties of water under negative pressures," *The Journal of Chemical Physics*, vol. 98, no. 11, 1993.

[30] M. Grimsditch, S. Popova, and A. Polian, "Test of the equation of state of water up to freezing at 100 and 200℃," *The Journal of Chemical Physics*, vol. 105, no. 19, 1996.

[31] F. Li, Q. Cui, Z. He, T. Cui, J. Zhang, Q. Zhou, G. Zou, and S. Sasaki, "High pressure-temperature Brillouin study of liquid water: Evidence of the structural transition from low-density water to high-density water," *The Journal of Chemical Physics*, vol. 123, no. 17, 2005.

[32] E. Courtens, J. Pelous, J. Phalippou, R. Vacher, and T. Woignier, "Brillouin-scattering measurements of phonon-fracton crossover in silica aerogels," *Physical Review Letters*, vol. 58, pp. 128–131, 1987.

[33] J. D. Bass, "Elasticity of grossular and spessartite garnets by Brillouin spectroscopy," *Journal of Geophysical Research: Solid Earth (1978–2012)*, vol. 94, no. B6, pp. 7621–7628, 1989.

[34] S. V. Sinogeikin, J. Zhang, and J. D. Bass, "Elasticity of single crystal and polycrystalline MgSiO$_3$ perovskite by Brillouin spectroscopy," *Geophysical Research Letters*, vol. 31, no. 6, 2004.

[35] P. Dainese, P. S. J. Russell, N. Joly, J. Knight, G. Wiederhecker, H. L. Fragnito, V. Laude, and A. Khelif, "Stimulated Brillouin scattering from multi-GHz-guided acoustic phonons in nanostructured photonic crystal fibres," *Nature Physics*, vol. 2, no. 6, pp. 388–392, 2006.

[36] J. Ko, K. Roleder, and A. Bussmann-Holder, "Determination of elastic stiffness coefficients of lead zirconate single crystals in the cubic phase by Brillouin light scattering," in *Materials Science and Engineering Conference Series*, vol. 54, p. 2002, 2014.

[37] G. Scarcelli and S. H. Yun, "Confocal Brillouin microscopy for three-dimensional mechanical imaging," *Nature Photonics*, vol. 2, no. 1, pp. 39–43, 2008.

[38] S. Reiss, G. Burau, O. Stachs, R. Guthoff, and H. Stolz, "Spatially resolved Brillouin spectroscopy to determine the rheological properties of the eye lens," *Biomedical Optics Express*, vol. 2, no. 8, pp. 2144–2159, 2011.

[39] F. Palombo, M. Madami, N. Stone, and D. Fioretto, "Mechanical mapping with chemical specificity by confocal Brillouin and Raman microscopy," *Analyst*, vol. 139, no. 4, pp. 729–733, 2014.

[40] C. Sandweg, M. Jungfleisch, V. Vasyuchka, A. Serga, P. Clausen, H. Schultheiss, B. Hillebrands, A. Kreisel, and P. Kopietz, "Wide-range wavevector selectivity of magnon gases in Brillouin light scattering spectroscopy," *Review of Scientific Instruments*, vol. 81, no. 7, p. 073902, 2010.

[41] A. A. Serga, V. S. Tiberkevich, C. W. Sandweg, V. I. Vasyuchka, D. A. Bozhko, A. V. Chumak, T. Neumann, B. Obry, G. A. Melkov, A. N. Slavin, *et al.*, "Bose-Einstein condensation in an ultra-hot gas of pumped magnons," *Nature Communications*, vol. 5, 2014.

[42] V. E. Demidov, S. Urazhdin, and S. O. Demokritov, "Direct observation and mapping of spin waves emitted by spin-torque nano-oscillators," *Nature Materials*, vol. 9, no. 12, pp. 984–988, 2010.

[43] M. Madami, S. Bonetti, G. Consolo, S. Tacchi, G. Carlotti, G. Gubbiotti, F. Mancoff, M. A. Yar, and J. Åkerman, "Direct observation of a propagating spin wave induced by spin-transfer torque," *Nature Nanotechnology*, vol. 6, no. 10, pp. 635–638, 2011.

[44] V. E. Demidov, S. Urazhdin, V. Tiberkevich, A. Slavin, and S. O. Demokritov, "Control of spin-wave emission from spin-torque nano-oscillators by microwave pumping," *Physical Review B*, vol. 83, no. 6, p. 060406, 2011.

[45] V. E. Demidov, S. Urazhdin, H. Ulrichs, V. Tiberkevich, A. Slavin, D. Baither, G. Schmitz, and S. O. Demokritov, "Magnetic nano-oscillator driven by pure spin current," *Nature Materials*, vol. 11, no. 12, pp. 1028–1031, 2012.

[46] K. An, D. R. Birt, C.-F. Pai, K. Olsson, D. C. Ralph, R. Buhrman, X. Li, *et al.*, "Control of propagating spin waves via spin transfer torque in a metallic bilayer waveguide," *arXiv preprint arXiv:1308.6357*, 2013.

[47] V. Naletov, G. de Loubens, S. Borlenghi, and O. Klein, "Spin-wave emission from spin-torque nano-oscillators and its control by microwave pumping," in *Magnonics*, pp. 163–175, Springer, 2013.

[48] V. Demidov, S. Urazhdin, A. Rinkevich, G. Reiss, and S. Demokritov, "Spin Hall controlled magnonic microwaveguides," *Applied Physics Letters*, vol. 104, no. 15, p. 152402, 2014.

[49] G. Gubbiotti, S. Tacchi, G. Carlotti, N. Singh, S. Goolaup, A. Adeyeye, and M. Kostylev, "Collective spin modes in monodimensional magnonic crystals consisting of dipolarly coupled nanowires," *Applied Physics Letters*, vol. 90, no. 9, p. 092503, 2007.

[50] S. Tacchi, F. Montoncello, M. Madami, G. Gubbiotti, G. Carlotti, L. Giovannini, R. Zivieri, F. Nizzoli, S. Jain, A. Adeyeye, *et al.*, "Band diagram of spin waves in a

two-dimensional magnonic crystal," *Physical Review Letters*, vol. 107, no. 12, p. 127204, 2011.

[51] G. Gubbiotti, M. Kostylev, S. Tacchi, M. Madami, G. Carlotti, J. Ding, A. Adeyeye, F. Zighem, A. Stashkevich, E. Ivanov, *et al.*, "Collective spin waves on a nanowire array with step-modulated thickness," *Journal of Physics D: Applied Physics*, vol. 47, no. 10, p. 105003, 2014.

[52] B. Van de Wiele and F. Montoncello, "Overcoming damping in spin wave propagation: A continuous excitation approach to determine time-dependent dispersion diagrams in 2D magnonic crystals," *arXiv preprint arXiv:1403.2549*, 2014.

[53] R. Zivieri, P. Malagò, and L. Giovannini, "Band structure and effective properties of binary magnonic crystals," *Photonics and Nanostructures-Fundamentals and Applications*, 2014.

[54] C. V. Raman, "A change of wave-length in light scattering," *Nature*, vol. 121, p. 619, 1928.

[55] L. Brillouin, "Diffusion of light and x-rays by a transparent homogeneous body," *Ann. Phys.(Paris)*, vol. 17, p. 88, 1922.

[56] J. Kerr, "On rotation of the plane of polarization by reflection from the pole of a magnet," *The London, Edinburgh, and Dublin Philosophical Magazine and Journal of Science*, vol. 3, no. 19, pp. 321–343, 1877.

[57] A. Barman and A. Haldar, *Solid State Physics*, vol. 65, ch. Time-domain study of magnetization dynamics in magnetic thin films and micro- and nanostructures. 2014.

[58] E. Hecht, *Optics*. San Francisco, CA: Pearson, 4th ed., 2002.

[59] J. R. Sandercock, *Tandem Fabry-Perot Interferometer TFP-1, Operator Manual*. JRS Scientific Instruments.

[60] J. R. Sandercock in *Light Scattering in Solids*, vol. 2, 1971.

[61] C. E. Patton. personal communication.

[62] J. Sandercock, "Brillouin scattering study of SbSI using a double-passed, stabilised scanning interferometer," *Optics Communications*, vol. 2, no. 2, pp. 73–76, 1970.

[63] W. Wettling, W. D. Wilber, P. Kabos, and C. E. Patton, "Light scattering from parallel-pump instabilities in yttrium iron garnet," *Physical Review Letters*, vol. 51, pp. 1680–1683, Oct 1983.

[64] W. D. Wilber, W. Wettling, P. Kabos, C. E. Patton, and W. Jantz, "A wave-vector selective light scattering magnon spectrometer," *Journal of Applied Physics*, vol. 55, no. 6, 1984.

[65] C. E. Patton, *A Idiot's Guide to Tandem Multi-pass Fabry Perot Alignment and Operation*. Internal Document.

[66] K. S. Buchanan, *Companion to Patton's Idiot Guide to BLS, Updated for the TFPDAS4 Software*. Internal Document.

[67] H. Schultheiss and K. Vogt, *TFPDAS4 Operator Manual*. Hillebrands Group, University of Kaiserslautern.

[68] V. E. Demidov, S. O. Demokritov, B. Hillebrands, M. Laufenberg, and P. P. Freitas, "Radiation of spin waves by a single micrometer-sized magnetic element," *Applied Physics Letters*, vol. 85, no. 14, pp. 2866–2868, 2004.

[69] G. Gubbiotti, G. Carlotti, M. Madami, S. Tacchi, P. Vavassori, and G. Socino, "Setup of a new Brillouin light scattering apparatus with submicrometric lateral resolution and its application to the study of spin modes in nanomagnets," *Journal of Applied Physics*, vol. 105, no. 7, p. 07D521, 2009.

[70] J. Jorzick, S. Demokritov, B. Hillebrands, M. Bailleul, C. Fermon, K. Guslienko, A. Slavin, D. Berkov, and N. Gorn, "Spin wave wells in nonellipsoidal micrometer size magnetic elements," *Physical Review Letters*, vol. 88, no. 047204, p. 13, 2002.

[71] L. Giovannini, F. Montoncello, F. Nizzoli, G. Gubbiotti, G. Carlotti, T. Okuno, T. Shinjo, and M. Grimsditch, "Spin excitations of nanometric cylindrical dots in vortex and saturated magnetic states," *Physical Review B*, vol. 70, p. 172404, Nov 2004.

[72] H. Schultheiss. personal communication, CSU visit.

[73] H. Schultheiss and K. Vogt, *Micro-TFPDAS4 Operator Manual*. Hillebrands Group, University of Kaiserslautern.

[74] H. S. Jung, W. D. Doyle, J. E. Wittig, J. F. Al-Sharab, and J. Bentley, "Soft anisotropic high magnetization Cu/FeCo films," *Applied Physics Letters*, vol. 81, no. 13, 2002.

[75] T. Shimatsu, H. Katada, I. Watanabe, H. Muraoka, and Y. Nakamura, "Effect of lattice strain on soft magnetic properties in FeCo/NiFe(Cr) thin films with 2.4 T," *Magnetics, IEEE Transactions on*, vol. 39, pp. 2365–2367, Sept 2003.

[76] Y. Fu, T. Miyao, J. Cao, Z. Yang, M. Matsumoto, X. Liu, and A. Morisako, "Effect of Co underlayer on soft magnetic properties and microstructure of FeCo thin films," *Journal of Magnetism and Magnetic Materials*, vol. 308, no. 1, pp. 165 – 169, 2007.

[77] Y. Okada, H. Hoshiya, T. Okada, and M. Fuyama, "Magnetic properties of FeCo multilayered films for single pole heads," *Magnetics, IEEE Transactions on*, vol. 40, pp. 2368–2370, July 2004.

[78] X. Liu, R. Sooryakumar, C. J. Gutierrez, and G. A. Prinz, "Exchange stiffness and magnetic anisotropies in bcc $Fe_{1-x}Co_x$ alloys," *Journal of Applied Physics*, vol. 75, no. 10, 1994.

[79] A. Liechtenstein, M. Katsnelson, and V. Gubanov, "Exchange interactions and spin-wave stiffness in ferromagnetic metals," *Journal of Physics F: Metal Physics*, vol. 14, no. 7, p. L125, 1984.

[80] M. Pajda, J. Kudrnovskỳ, I. Turek, V. Drchal, and P. Bruno, "Ab initio calculations of exchange interactions, spin-wave stiffness constants, and curie temperatures of Fe, Co, and Ni," *Physical Review B*, vol. 64, no. 17, p. 174402, 2001.

[81] K. Hller, "The spin wave excitations and the temperature dependence of the magnetization in iron, cobalt, nickel and their alloys," *Journal of Magnetism and Magnetic Materials*, vol. 61, no. 3, pp. 347–358, 1986.

[82] R. Pauthenet, "Spin waves in nickel, iron, and yttrium iron garnet," *Journal of Applied Physics*, vol. 53, no. 3, 1982.

[83] L. Ritchie, G. Xiao, Y. Ji, T. Y. Chen, C. L. Chien, M. Zhang, J. Chen, Z. Liu, G. Wu, and X. X. Zhang, "Magnetic, structural, and transport properties of the Heusler alloys Co_2MnSi and NiMnSb," *Physical Review B*, vol. 68, p. 104430, Sep 2003.

[84] E. Girt, W. Huttema, O. Mryasov, E. Montoya, B. Kardasz, C. Eyrich, B. Heinrich, A. Y. Dobin, and O. Karis, "A method for measuring exchange stiffness in ferromagnetic films," *Journal of Applied Physics*, vol. 109, no. 7, p. 07B765, 2011.

[85] S. P. Vernon, S. M. Lindsay, and M. B. Stearns, "Brillouin scattering from thermal magnons in a thin Co film," *Physical Review B*, vol. 29, pp. 4439–4442, Apr 1984.

[86] J. Booth, G. Srinivasan, C. Patton, and P. De Gasperis, "Brillouin light scattering study of the spin wave stiffness parameter in Sc-substituted lutetium-yttrium iron garnet," *Magnetics, IEEE Transactions on*, vol. 23, no. 5, pp. 3494–3496, 1987.

[87] O. Gaier, J. Hamrle, S. Trudel, B. Hillebrands, H. Schneider, and G. Jakob, "Exchange stiffness in the Co_2FeSi Heusler compound," *Journal of Physics D: Applied Physics*, vol. 42, no. 23, p. 232001, 2009.

[88] J. Hamrle, O. Gaier, S. Min, B. Hillebrands, Y. Sakuraba, and Y. Ando, "Determination of exchange constants of Heusler compounds by Brillouin light scattering spectroscopy: application to Co_2MnSi," *Journal of Physics D: Applied Physics*, vol. 42, no. 8, p. 084005, 2009.

[89] C. Mathieu, H.-J. Liu, K. S. Buchanan, and V. R. Inturi, "Volume exchange in soft FeCo films of high magnetization," *Journal of Applied Physics*, vol. 111, no. 7, 2012.

[90] J. R. Sandercock and W. Wettling, "Light scattering from surface and bulk thermal magnons in iron and nickel," *Journal of Applied Physics*, vol. 50, no. B11, 1979.

[91] K. S. Buchanan. personal communication.

[92] G. T. Rado and R. J. Hicken, "Theory of magnetic surface anisotropy and exchange effects in the Brillouin scattering of light by magnetostatic spin waves (invited)," *Journal of Applied Physics*, vol. 63, no. 8, 1988.

[93] A. A. Serga, A. V. Chumak, and B. Hillebrands, "YIG magnonics," *Journal of Physics D: Applied Physics*, vol. 43, no. 26, p. 264002, 2010.

[94] K. Kotzebue, "Broadband electronically-tuned microwave filters," in *WESCON/60 Conference Record*, vol. 4, pp. 21–27, 1960.

[95] P. Roschmann, "Compact YIG bandpass filter with finite-pole frequencies for applications in microwave integrated circuits (short papers)," *Microwave Theory and Techniques, IEEE Transactions on*, vol. 21, no. 1, pp. 52–57, 1973.

[96] C. Greene, "A microstrip nonreciprocal tunable YIG filter," *Solid-State Circuits, IEEE Journal of*, vol. 3, no. 2, pp. 146–148, 1968.

[97] S. A. Wolf, D. D. Awschalom, R. A. Buhrman, J. M. Daughton, S. von Molnr, M. L. Roukes, A. Y. Chtchelkanova, and D. M. Treger, "Spintronics: A spin-based electronics vision for the future," *Science*, vol. 294, no. 5546, pp. 1488–1495, 2001.

[98] J. E. Hirsch, "Spin Hall effect," *Physical Review Letters*, vol. 83, pp. 1834–1837, Aug 1999.

[99] M. D. Stiles and A. Zangwill, "Anatomy of spin-transfer torque," *Physical Review B*, vol. 66, p. 014407, Jun 2002.

[100] M. B. Jungfleisch, V. Lauer, R. Neb, A. V. Chumak, and B. Hillebrands, "Improvement of the yttrium iron garnet/platinum interface for spin pumping-based applications," *Applied Physics Letters*, vol. 103, no. 2, 2013.

[101] C. L. Ordóñez Romero, B. A. Kalinikos, P. Krivosik, W. Tong, P. Kabos, and C. E. Patton, "Three-magnon splitting and confluence processes for spin-wave excitations in yttrium iron garnet films: Wave vector selective Brillouin light scattering measurements and analysis," *Physical Review B*, vol. 79, p. 144428, Apr 2009.

[102] C. Mathieu, V. T. Synogatch, and C. E. Patton, "Brillouin light scattering analysis of three-magnon splitting processes in yttrium iron garnet films," *Physical Review B*, vol. 67, p. 104402, Mar 2003.

[103] V. T. Synogach, Y. K. Fetisov, C. Mathieu, and C. E. Patton, "Ultrashort microwave pulses generated due to three magnon interactions," *Physical Review Letters*, vol. 85, pp. 2184–2187, Sep 2000.

[104] P. Janatha. personal communication.

[105] J. O. Oti and S. E. Russek, "Micromagnetic simulations of magnetoresistive behavior of sub-micrometer spin-valve MRAM devices," *Magnetics, IEEE Transactions on*, vol. 33, no. 5, pp. 3298–3300, 1997.

[106] J. Sun, D. Monsma, T. Kuan, M. Rooks, D. Abraham, B. Oezyilmaz, A. Kent, and R. Koch, "Spin-torque transfer in batch-fabricated spin-valve magnetic nanojunctions," *Journal of Applied Physics*, vol. 93, no. 10, pp. 6859–6863, 2003.

[107] C. Chappert, A. Fert, and F. N. Van Dau, "The emergence of spin electronics in data storage," *Nature Materials*, vol. 6, no. 11, pp. 813–823, 2007.

[108] I. N. Krivorotov and A. N. Slavin, "Spin-torque devices," March 2010. US Patent 7,678,475.

[109] T. Schneider, A. Serga, B. Leven, B. Hillebrands, R. Stamps, and M. Kostylev, "Realization of spin-wave logic gates," *Applied Physics Letters*, vol. 92, no. 2, p. 022505, 2008.

[110] S. Bandyopadhyay and M. Cahay, "Electron spin for classical information processing: a brief survey of spin-based logic devices, gates and circuits," *Nanotechnology*, vol. 20, no. 41, p. 412001, 2009.

[111] Y. Nakashima, K. Nagai, T. Tanaka, and K. Matsuyama, "Optimum design consideration for interferometric spin wave logic operations," *Journal of Applied Physics*, vol. 109, no. 7, p. 07D318, 2011.

[112] J. Ding, M. Kostylev, and A. Adeyeye, "Realization of a mesoscopic reprogrammable magnetic logic based on a nanoscale reconfigurable magnonic crystal," *Applied Physics Letters*, vol. 100, no. 7, p. 073114, 2012.

[113] C. Bayer, S. Demokritov, B. Hillebrands, and A. Slavin, "Spin-wave wells with multiple states created in small magnetic elements," *Applied Physics Letters*, vol. 82, no. 4, pp. 607–609, 2003.

[114] V. E. Demidov, S. O. Demokritov, K. Rott, P. Krzysteczko, and G. Reiss, "Self-focusing of spin waves in Permalloy microstripes," *Applied Physics Letters*, vol. 91, no. 25, pp. –, 2007.

[115] K. Vogt, H. Schultheiss, S. Hermsdoerfer, P. Pirro, A. Serga, and B. Hillebrands, "All-optical detection of phase fronts of propagating spin waves in a $Ni_{81}Fe_{19}$ microstripe," *Applied Physics Letters*, vol. 95, no. 18, p. 182508, 2009.

[116] T. Brächer, P. Pirro, B. Obry, B. Leven, A. Serga, and B. Hillebrands, "Mode selective parametric excitation of spin waves in a $Ni_{81}Fe_{19}$ microstripe," *Applied Physics Letters*, vol. 99, no. 16, p. 162501, 2011.

[117] J. A. Osborn, "Demagnetizing factors of the general ellipsoid," *Physical Revview*, vol. 67, pp. 351–357, Jun 1945.

[118] D. C. Cronemeyer, "Demagnetization factors for general ellipsoids," *Journal of Applied Physics*, vol. 70, no. 6, 1991.

[119] S. O. Demokritov, B. Hillebrands, and A. N. Slavin, "Brillouin light scattering studies of confined spin waves: linear and nonlinear confinement," *Physics Reports*, vol. 348, no. 6, pp. 441–489, 2001.

[120] M. J. Donahue and D. G. Porter, *OOMMF User's guide.* US Department of Commerce, Technology Administration, National Institute of Standards and Technology, 1999.

[121] S. O. Demokritov and V. E. Demidov, *Spin Wave Confinement*, ch. Quantized spin-wave modes due to lateral confinement. Singapore: Pan Standford Publishing, 2008.

[122] V. E. Demidov, S. O. Demokritov, K. Rott, P. Krzysteczko, and G. Reiss, "Mode interference and periodic self-focusing of spin waves in Permalloy microstripes," *Physical Review B*, vol. 77, p. 064406, Feb 2008.

[123] K. Y. Guslienko, S. O. Demokritov, B. Hillebrands, and A. N. Slavin, "Effective dipolar boundary conditions for dynamic magnetization in thin magnetic stripes," *Physical Review B*, vol. 66, p. 132402, Oct 2002.

[124] A. Aharoni, *Introduction to the Theory of Ferromagnetism*. Oxford: Oxford Science Publications, 2th ed., 2000.

[125] A. Haldar and K. S. Buchanan, "Magnetic antivortex formation in pound-key-like nanostructures," *Applied Physics Letters*, vol. 102, no. 11, 2013.

[126] G. Venkat, D. Kumar, M. Franchin, O. Dmytriiev, M. Mruczkiewicz, H. Fangohr, A. Barman, M. Krawczyk, and A. Prabhakar, "Proposal for a standard micromagnetic problem: Spin wave dispersion in a magnonic waveguide," *Magnetics, IEEE Transactions on*, vol. 49, no. 1, pp. 524–529, 2013.

[127] X. Xing, Y. Yu, S. Li, and X. Huang, "How do spin waves pass through a bend?," *Scientific Reports*, vol. 3, 2013.

[128] T. Brächer, P. Pirro, J. Westermann, T. Sebastian, B. Lgel, B. Van de Wiele, A. Vansteenkiste, and B. Hillebrands, "Generation of propagating backward volume spin waves by phase-sensitive mode conversion in two-dimensional microstructures," *Applied Physics Letters*, vol. 102, no. 13, 2013.

[129] T. Brächer, P. Pirro, A. A. Serga, and B. Hillebrands, "Localized parametric generation of spin waves in a longitudinally magnetized $Ni_{81}Fe_{19}$ waveguide," *Applied Physics Letters*, vol. 103, no. 14, 2013.

[130] M. Kostylev, "Non-reciprocity of dipole-exchange spin waves in thin ferromagnetic films," *Journal of Applied Physics*, vol. 113, no. 5, p. 053907, 2013.

[131] D. R. Birt, K. An, M. Tsoi, S. Tamaru, D. Ricketts, K. L. Wong, P. Khalili Amiri, K. L. Wang, and X. Li, "Deviation from exponential decay for spin waves excited with a coplanar waveguide antenna," *Applied Physics Letters*, vol. 101, no. 25, pp. –, 2012.

[132] S. Mangin, D. Ravelosona, J. Katine, M. Carey, B. Terris, and E. E. Fullerton, "Current-induced magnetization reversal in nanopillars with perpendicular anisotropy," *Nature Materials*, vol. 5, no. 3, pp. 210–215, 2006.

[133] W. Chen, J.-M. Beaujour, G. De Loubens, A. Kent, and J. Sun, "Spin-torque driven ferromagnetic resonance of Co/Ni synthetic layers in spin valves," *Applied Physics Letters*, vol. 92, no. 1, pp. 012507–012507, 2008.

[134] D. Bedau, H. Liu, J. Sun, J. Katine, E. Fullerton, S. Mangin, and A. Kent, "Spin-transfer pulse switching: From the dynamic to the thermally activated regime," *Applied Physics Letters*, vol. 97, no. 26, p. 262502, 2010.

[135] W. H. Rippard, A. M. Deac, M. R. Pufall, J. M. Shaw, M. W. Keller, S. E. Russek, G. E. Bauer, and C. Serpico, "Spin-transfer dynamics in spin valves with out-of-plane magnetized CoNi free layers," *Physical Review B*, vol. 81, no. 1, p. 014426, 2010.

[136] S. M. Mohseni, S. R. Sani, J. Persson, T. Anh Nguyen, S. Chung, Y. Pogoryelov, and J. Åkerman, "High frequency operation of a spin-torque oscillator at low field," *Physica Status Solidi (RRL)-Rapid Research Letters*, vol. 5, no. 12, pp. 432–434, 2011.

[137] F. Macia, P. Warnicke, D. Bedau, M.-Y. Im, P. Fischer, D. Arena, and A. Kent, "Perpendicular magnetic anisotropy in ultrathin Co—Ni multilayer films studied with ferromagnetic resonance and magnetic x-ray microspectroscopy," *Journal of Magnetism and Magnetic Materials*, vol. 324, no. 22, pp. 3629–3632, 2012.

[138] G. Gubbiotti, G. Carlotti, S. Tacchi, M. Madami, T. Ono, T. Koyama, D. Chiba, F. Casoli, and M. Pini, "Spin waves in perpendicularly magnetized Co/Ni (111) multilayers

in the presence of magnetic domains," *Physical Review B*, vol. 86, no. 1, p. 014401, 2012.

Optical Mask Design and Lithography Process For Micro-BLS Microstrips

This appendix reviews the mask design and the optical lithography process used to grow the microwave antennae discussed in Chap. 6. The design of the mask was chosen such that it was compatible with the micro-BLS apparatus and the spin wave physics that were of interest. The lithography process, which has proven successful for growing microstrip, is outlined in the following sections.

A.1. Coplanar Waveguide Antenna and Optical Mask Design

Figure A.1 shows a 1×1 cm^2 sample that has six ground-signal-ground (GSG) antenna structures. This sample size was optimal for the sample holder used in the micro-BLS. Each GSG antenna is designed to overlay two magnetic microstrips. The larger ends of the GSG antenna were chosen to be compatible with the dimensions of the picoprobes that are used to connect the antennae to the microwave signal generator. The picoprobes were a custom design from GGB Industries with a flat extended probe that will fit under the microscope objective used in the micro-BLS setup. The probes have a separation between the ground and signal probes of 400 μm.

The optical mask was printed on 4×4 in^2 soda lime glass by laser writer. The mask was printed so that the structure of the waveguides were transparent on an otherwise chromium-coated mask. The lithography process was done with two masks. One mask was made with the red shaded areas in Fig. A.1 and another was made by our collaborators with the green shaded area. The green shaded areas represents the magnetic materials. Once the magnetic
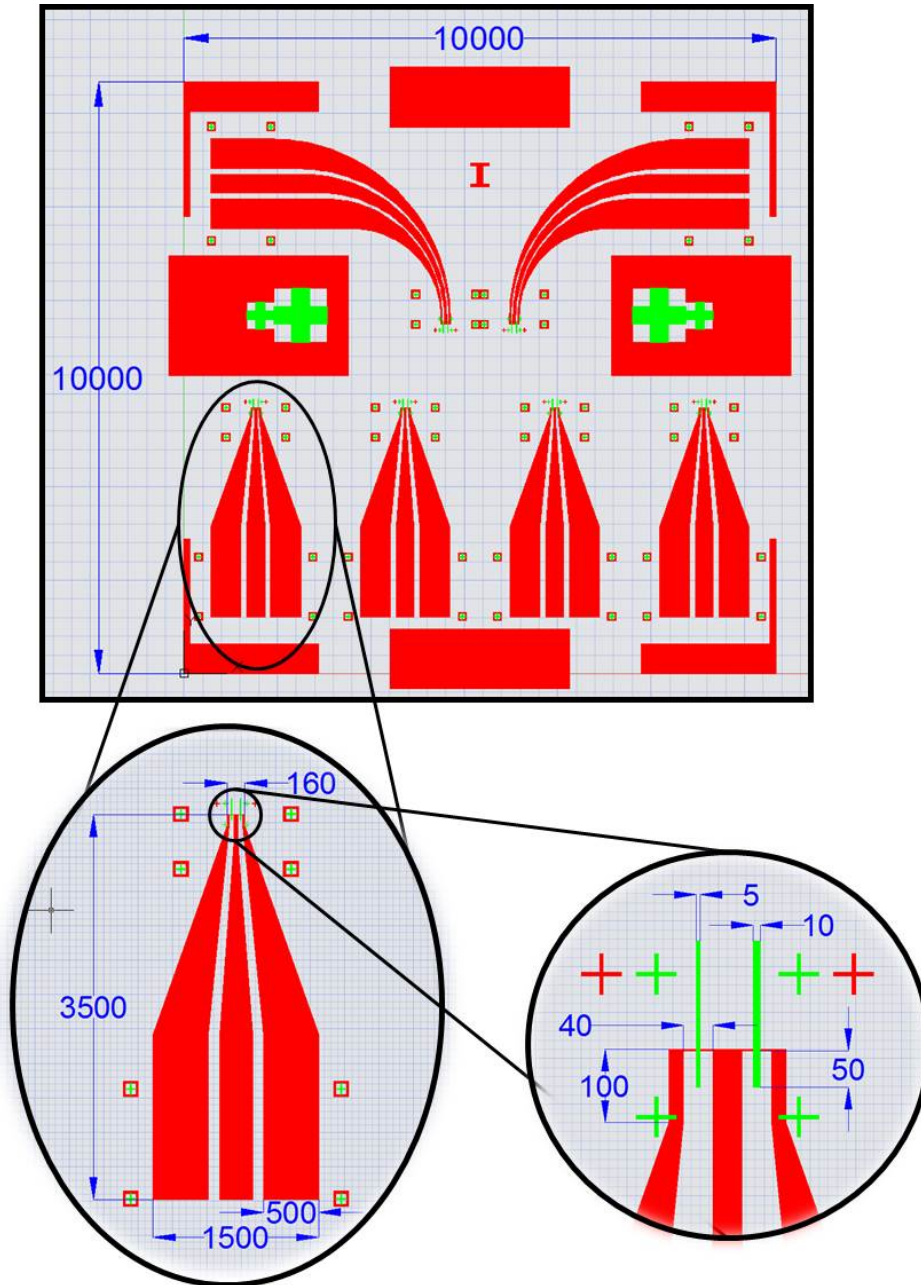
FIGURE A.1. Antenna design for micro-BLS microstrip spin wave measurements. Colored in red are the antenna structures and areas that were deposited in gold. The green areas were deposited with the magnetic materials. All dimensions are in units of micrometers.

materials were deposited, the lithography process described in the proceeding section was

used to deposit the antenna structures on top of the magnetic materials.

A.2. Lithography and Liftoff Processes

The lithography and liftoff processes outlined below are steps that were used at the Colorado Nanofabrication Laboratory (CNL). The lithography for the CoNi samples was done in collaboration with Martin Asmat-Uceda. The process was done following a recipe that was provided at the CNL for the AZ P4210 resist, which is a positive photoresist.

Steps for developing and exposing using a positive photoresist:

(1) Clean substrate with acetone, isopropyl alcohol, and then water.

(2) Blow dry with nitrogen gas.

(3) Remove moisture by baking on a hotplate set to 110 °C for 120 seconds.

(4) Spin coat adhesive layer (HDMS) at 6000 rpm for 30 seconds (HDMS is an adhesive layer to help the photoresist stick and is not a completely necessary step).

(5) Spin coat photoresist (AZ P4210) at 6000 rpm for 30 seconds. This angular velocity should yield a photoresist thickness of 1.8 μm.

(6) Cure the photoresist by baking on a hotplate set to 100 °C for 90 seconds. Note that the baking temperature can affect the development time.

(7) Using the mask aligner, expose the photoresist-coated substrate for 15 seconds.

(8) Develop the exposed substrate in a solution of 1 part developer (AZ400K) and 3 parts water for 60 seconds.

(9) Rinse the developed substrate in a deionized water bath for over 60 seconds.

(10) Rinse the substrate again in a second, clean, deionized water bath for at least 60 seconds.

(11) Blow dry with nitrogen gas.

(12) Examine the developed substrate under a microscope.

(13) If substrate is overdeveloped, underdeveloped, overexposed, underexposed, or a combination of these, adjust exposure time or developing time and repeat all steps.

Once the photoresist has been developed, the next step is to deposit the materials. To achieve good adhesion of the material, the substrate must be very clean and very dry. It is imperative to confirm proper development before deposition. Once the deposition process has began, there is no going back. Deposition methods include, but are not limited to, thermal evaporation, electron beam evaporation, or sputtering. The exact method will depend on the material. The material of interest for the structures discussed in Chap. 6 is gold and the deposition method was thermal evaporation. Since gold does not adhere well, an adhesion layer of approximately 10 nm of chromium was first deposited. The gold was for the material that made up the microwave antennae which are shown in red in Fig. A.1. The CoNi structures discussed in Chap. 6, shown as green in Fig. A.1, were grown at New York University by Ferran Macià. The liftoff process outlined below proved successful in removing gold from the substrate that was not exposed. Note that the smallest dimension of each microwave antenna was 2 μm.

Steps for liftoff using acetone:

(1) Place the substrate with the newly deposited film in an acetone bath with structures facing upwards.

(2) Cover the container and check it periodically. Be sure to top it up with additional acetone to prevent the substrate from completely drying.

(3) Let it sit for a few hours (large flakes will start to lift off of the substrate).

(4) To aid the liftoff process, slight agitation or the use of a sonic bath may be necessary. If using slight agitation, make sure to go slowly and that the substrate does not move around in the container. Movement of the substrate can lead to breakage. If using a sonic bath, use a short burst of approximately 1 second. Longer burst can lead to vibrating off small structures.

(5) Let it sit for a few hours.

(6) Repeat 4 and 5 until the desired liftoff is achieved.

(7) Remove carefully, rinse, and dry.